2-1-2017

Water splitting by defects: Insights into multinary transition metal oxides for solar water splitting

Samar Mohamed Fawzy Adam Shahin

The American University in Cairo

The Graduate School

The Nanotechnology Program

Water Splitting by defects: Insights into multinary transition metal oxides for solar water splitting

A Thesis in Nanotechnology

By:

Samar Mohammad Fawzy Adam

Submitted in Partial Fulfilment of the Requirements for

The Degree of Masters of Science in Nanotechnology

December 21st,2017

The Thesis of Samar Mohammad Fawzy was reviewed and approved* by the following

Nageh K. Allam

Associate Professor, Physics Department
Director, Energy of Materials Laboratory (EML).
The American University in Cairo
Thesis Advisor
Chair of Committee

Salah M. El-Sheikh
Professor, Physics Department
The American University in Cairo
Internal Examiner

Ahmad Mahmoud
Associate Professor, Chemistry Department
Faculty of Science, Cairo University.
External Examiner

Mohammad T. Al-Fiky
Assistant Professor, Physics Department
The American University in Cairo
Thesis Defence Moderator

* Signatures are on file in the Graduate School.

Abstract

With the energy deficiency problem becoming more threatening, the need to find reliable and alternative energy resources is becoming inevitable. Hydrogen gas is considered a good and cleaner alternative due to its green combustion; and it is used in many applications. Accordingly, the use of solar energy in water splitting to produce hydrogen gas is attracting much attention. Finding the optimum semiconducting material that can efficiently absorb sun light and use it in charge carriers' generation to split water into hydrogen and oxygen is a hot research topic; as many challenges exist in this regard. For instance, wide-bandgap semiconductors have enhanced stability, but absorption limited to the UV region. On the other hand, a lot of the narrow-bandgap semiconductors have poor stability in aqueous electrolytes.

In this thesis we explore different effective pathways to overcome the wide band gap problem. In the first part, the fabrication of nanostructured Ti-Nb-Zr MPNTs via simple hard templating anodization method in an electrochemical bath using Formamide-based electrolyte is explained. The formation mechanism and growth model of the MPNTs is discussed using FESEM images. Optical properties are examined using UV-Vis as well as photoelectrochemical properties where the MPNTs have shown 9-fold enhancement in the photocurrent density over the compact counterpart. The MPNTs possess graded refractive index which was confirmed by ellipsometry measurement; and high light scattering owing to their large diameter.

In the second part of the thesis, the MPNTs are annealed in three different gases Air, Oxygen and Hydrogen where a 26-fold enhancement was achieved in the H100 compared to Air and O100. XPS, XRD, and Raman scattering suggested the formation of a single mixed oxide under Air and Oxygen atmospheres, while Zr formed a second phase $ZrTiO_4$ under the reducing atmosphere. XPS core spectra confirmed that Hydrogen annealing resulted in formation of valence band tail states and Ti^{3+} defects. A thorough discussion is presented on the defects present and their contribution to the water splitting process.

Finally, CZTS is known to be a narrow-bandgap p-type semiconductor with absorption extending to the visible region. It was synthesized by a solvothermal method, and deposited by electrophoresis on the MPNTs annealed in Hydrogen. Despite of its instability in 1M KOH, a proof of concept was accomplished, as a great photocurrent enhancement was achieved.

Table of contents

List of Figures

List of Tables

List of Acronyms

AM	*Air Mass number*
CBM	*Conduction Band Minimum*
VBM	*Valence Band Maximum*
DFT	*Density Functional Theory*
EDX	*Energy-dispersive X-ray spectroscopy*
EIS	*Electrochemical Impedance Spectroscopy*
FA	*Formamide*
FESEM	*Field Emission Scanning Electron Microscope*
MS	*Mott-Schottky*
NHE	*Normal Hydrogen Electrode*
NTs	*Nanotubes*
$E_{p,d}$	*Free enthalpy of oxidation*
$E_{n,d}$	*Free enthalpy of reduction*
OER	*Oxygen Evolution Reaction*
HER	*Hydrogen Evolution Reaction*
MPNTs	*Multipodal Nanotubes*
PEC	*Photoelectrochemical*
DR	*Diffuse Reflectance*
UV-Vis	*Ultra Violet – Visible*
Air0	*Air annealed samples*
O100	*Oxygen annealed samples under flow of 100 SCCM*
H100	*Hydrogen annealed samples under flow of 100 SCCM*
XRD	*X- ray Diffraction*
XPS	*X-ray Photoelectron Spectrometer*
CZTS	*Copper Zinc Tin Sulfide*

Acknowledgements

All praise is to Allah, the most Merciful, Lord of the worlds, and the sole provider of each cause of success in every person's life. Allah gives us guidance to make choices and puts people in our paths that change our life course. This being said, I would like to express my gratitude to Dr. Nageh Allam, for his financial support throughout my thesis. I would also like to thank him for his patience with his students including myself, and for trying to guide us and help us find opportunities where we can learn and excel.

My gratitude also goes to my professors at the AUC, for their teaching and guidance especially Dr. Hanadi Salem, Dr. AbdelHameed Galal, Dr. Adham Ramadan, and Dr. Mohammad Alfiky. I would also like to thank the examination committee for their time and efforts to facilitate my thesis defence.

I would like to thank my parents who always guided me and tried to raise me to be a righteous person. I would especially like to thank my husband who has been very supportive throughout my studies and who continues to be a role model for me. I would like to thank my sisters Sara, Basma, and Yasmine, and my school friends especially Rahma Ali and Eman Ayman who supported me in my decision to leave my corporate job and to pursue a master's degree.

Finally, I would like to thank all the EML members for providing a nice work environment.

Chapter 1

Introduction & Thesis Scope

1.1 The Energy Problem

There is no doubt that the continuity of human civilization is majorly dependent on its ability to find and secure energy sources. In fact, the industrial revolution which reshaped the balance of power in the world in the beginning of the 18th century was entirely related to dispensing wood as a main energy source and shifting to coal. In addition, the vast advances and development in technology in the modern 20th and 21st centuries are attributed to the Black Gold or petroleum. Unfortunately, and expectedly, mankind greed and reckless behaviour is resulting in a great energy deficiency crisis due to the continuous diminution of fossil fuels. This energy crisis, which if he does not appropriately address and come together to solve, could lead to unprecedented consequences, namely the destruction of civilization as we know it. The existing energy challenge has mainly four aspects which need to be addressed:

1- Migration and over population

Since the beginning of civilization, man has migrated to where he can find water, food, shelter and other primary needs fulfilled; and ever since, he has been doing the same with these primary needs expanding to luxurious and prosperous life styles. Ergo, we find places rich of oil, natural gas and coal to be over populated. For instance, Texas is the 2nd most populated state in the U.S., and the top in the number of oil reserves [1].

2- War

Man being blinded by greed and imperialism has been fighting one another and unrightfully exploiting resources of others. Many wars have been fought and many lives have been lost to invade countries rich in oil in order to control oil reserves. The Russian intervention in Syria is regarded as one example of brute force use against innocent civilians for the sake of interest in securing oil funding.

3- Pollution

No doubt, the by-products produced during fossil fuels burning and consumption such as NO_x, SO_x, Cadmium, Beryllium, and Mercury are regarded as hazardous pollutants; especially CO_2 which holds approximately 80% of the total carbon dioxide emission. Global warming is attributed to the increase in CO_2 emissions which result in the greenhouse effect and causes the heat induced by infrared to become trapped and not be able to escape the earth

as shown in Figure 1-1[2]. In fact, the Global Carbon Project predicted an annual increase of 2.5% in the emission of CO_2 generated from fossil fuels combustion globally [3]. This will be reflected in a 4.3° C increase in earth's temperature by the year 2100 [4]. This global warming impacts sea level rising and is expected to have a great effect on climate change and accordingly destroy the balance of many ecosystems and endanger a wide range of species of plants, animals and marine life; not to mention the forecasted economic crises.

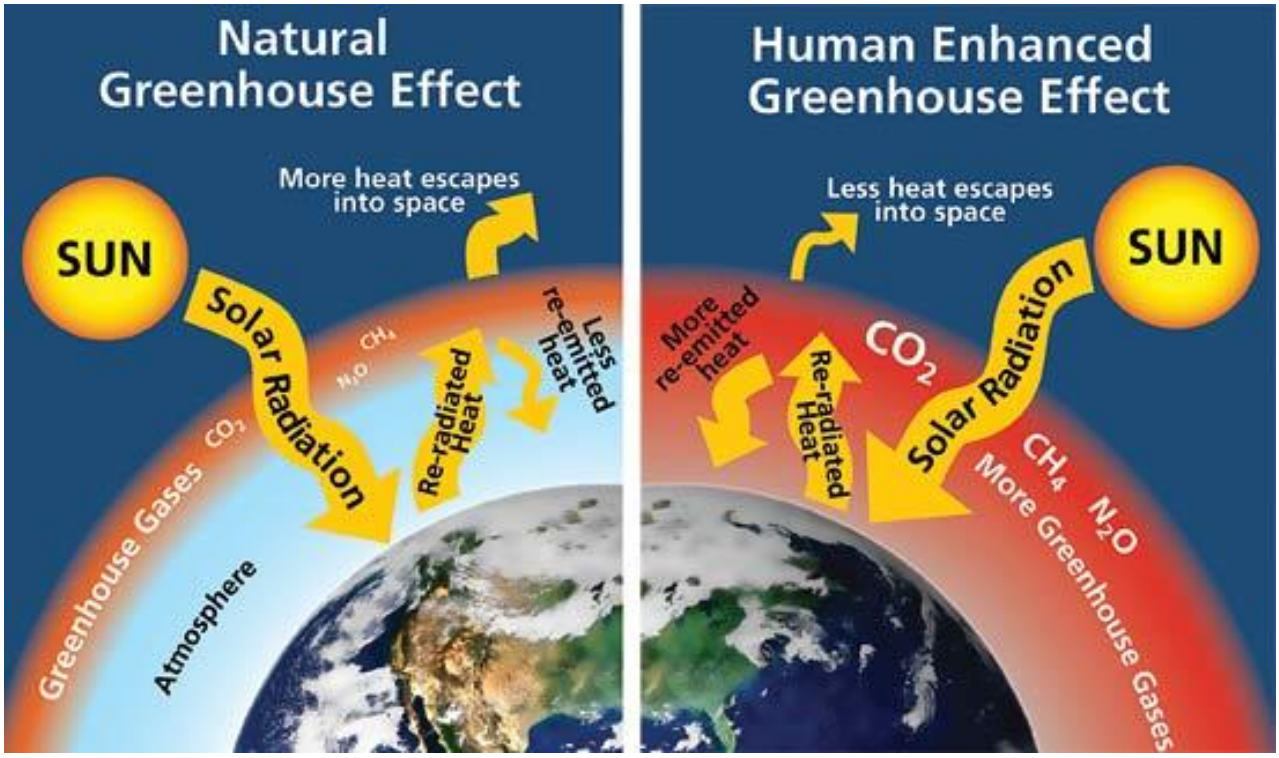

Figure 1-1 Human induced greenhouse effect versus natural greenhouse effect [2]

4- Fossil fuels depletion and the "Terawatt Challenge"

The continuous increase in the population of the world is a direct reason for the continuous reduction in available non-renewable fossil fuels due to the increased energy consumption rates. As reported by the Association for the study of Peak Oil & Gas (ASPO), it is expected that in a maximum of a hundred years, we will run out of all fossil fuels including coal, oil and natural gas, if the current consumption rates are maintained[5]. However, due to the increase in population, this duration may be shortened even more to a maximum of 80 years[6]. In addition, the cost of a daily life supply worth of energy is becoming not affordable by many individuals in a wide range of world countries. Not to mention that more natural resources like

water are becoming depleted in developing countries due to lack of consumption rationalization [7]. Professor Rick Smalley, 1996 Nobel Prize laureate, was the first to address the energy issue as the *Terrawatt Challenge* [8]. His study pointed out the urge to search for renewable energy resources that can replace fossil fuels. The United Nations estimates that the earth population will reach about 9.8 billion people by 2050[9]. As indicated in Figure 1-2, the consumption of energy globally in 2050 is estimated to become 28 terawatts per year versus 16 terawatts in 2009 [10]. It has been proven that the only possible way to meet this huge demand is to shift from the current non-renewable fossil fuel based energy supply systems to renewable ones independent of carbon as indicated in Figure 1-3. There are many renewable energy resources such as wind, biomass, geothermal and the sun. Solar energy is the only resource that can outweigh and exceed the total expected energy demand, as it is capable of providing up to 23,00 terawatts, i.e. almost 800 times more than the required demand.

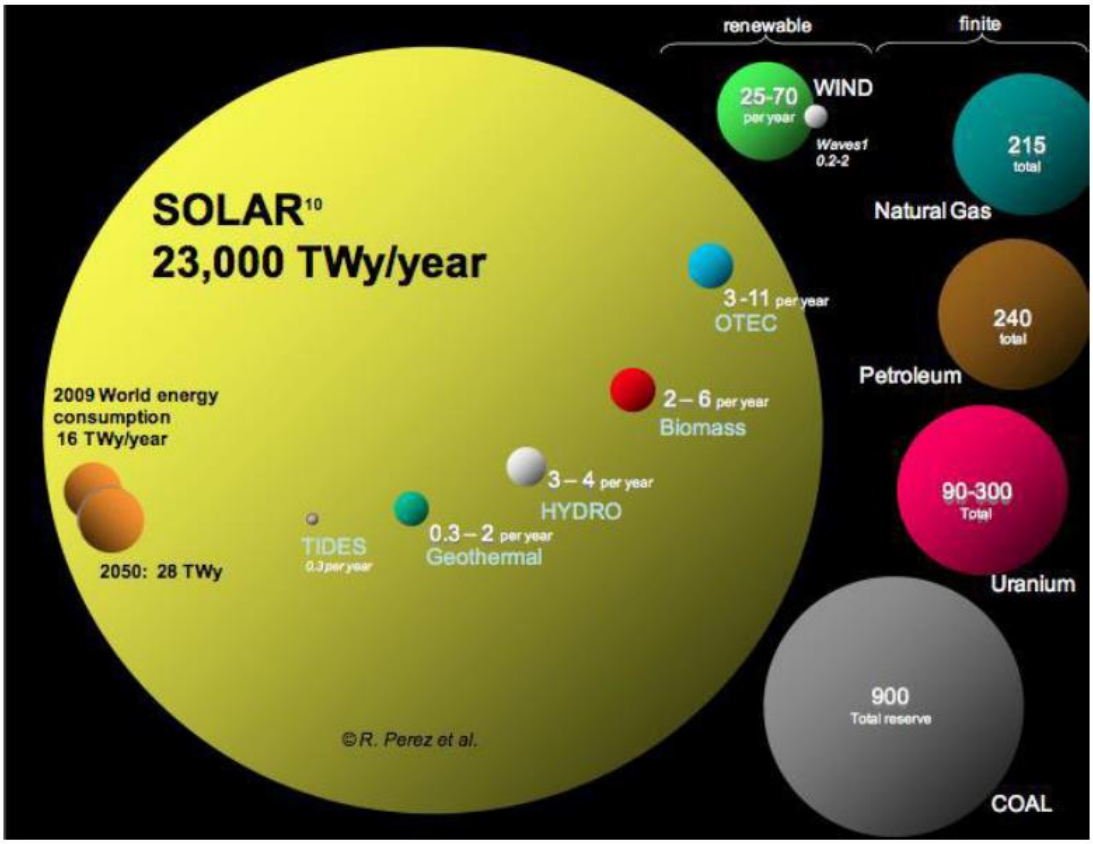

Figure 1-2 Energy demand in 2050 and the amount of energy supplied through various resources [10]

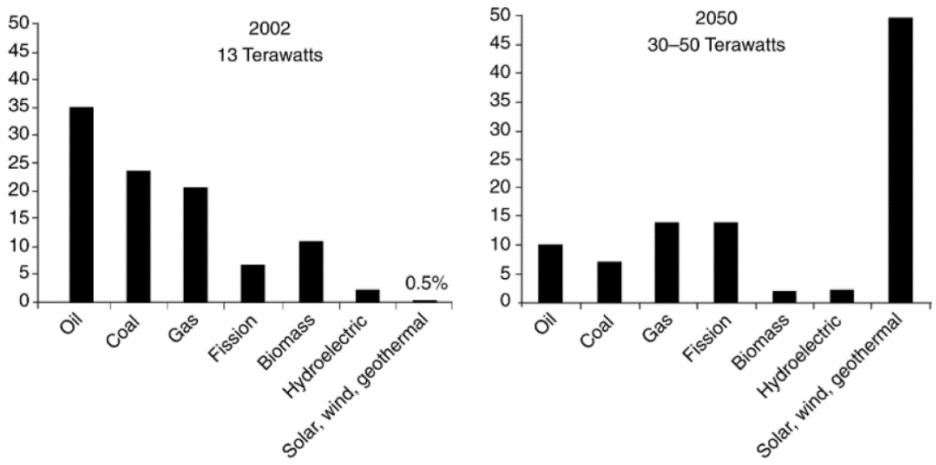

Figure 1-3 Ways to overcome the Terawatt Challenge: redistribution of energy resources where fossil fuels being the main supply on the left is shifted to Solar, wind and geothermal on the right [11]

From the previous discussion, it is concluded that the world is in dire need to join efforts and properly address the mentioned problems and find a proper solution to be globally implemented. World leaders, the people, environmental organizations, and the scientific community need to look for renewable, efficient and clean energy resources that can ensure sustainable mankind advancement.

1.2 Hydrogen – An Alternative Fuel

Hydrogen has emerged to be a possible fuel alternative to fossil fuels. It is a light weight gas that is abundant in the earth's atmosphere and produces nearly three times more energy during its combustion compared to natural gas and crude oil [12]. It is easily transported due to its light weight; in fact, it is has a much lower density than most fuels; for example, Methane is 8 times heavier [13]. Hydrogen is produced by splitting water, a relatively abundant resource, and it is considered as a clean fuel because its main by-product is steam. Accordingly, it is regarded to be environmentally friendly. In addition, it is used in many applications as can be seen in Figure 1-4, including fuel cells, ammonia fertilizers manufacturing, oil refining, and tons of pharmaceuticals production [14].

Hydrogen production can be obtained through various ways as shown in Figure 1-5 [15]. Although this may seem plausible, most of these processes are expensive as large amounts of energy are consumed throughout the process. While only 3.9% of the total Hydrogen produced is through water electrolysis, very large percentage (~ 96%) of the primary energy sources used

in Hydrogen production come from non-renewable fossil fuels. This raises questions about the need to invest more in the electrolysis process given that water is quite abundant which will be discussed further.

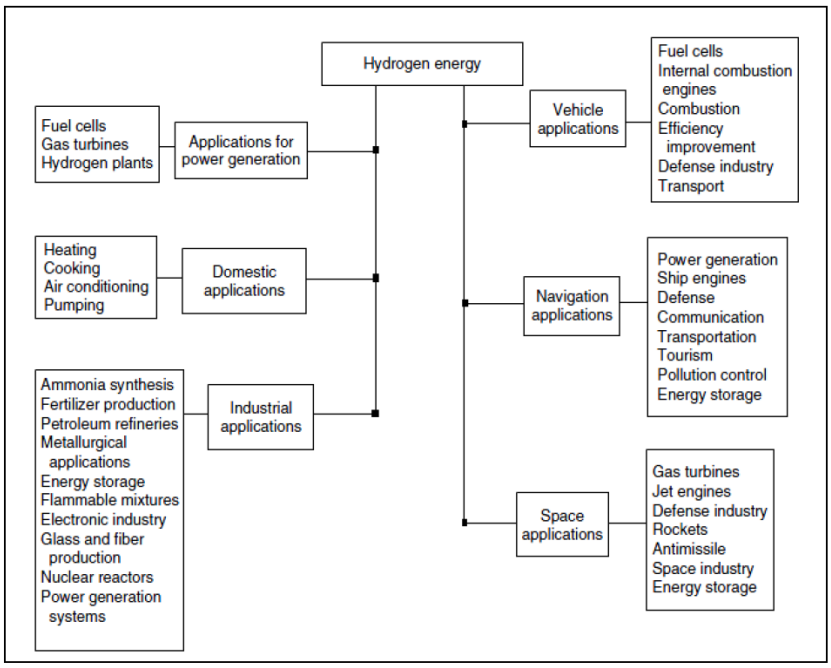

Figure 1-4 Different applications of Hydrogen fuel [16]

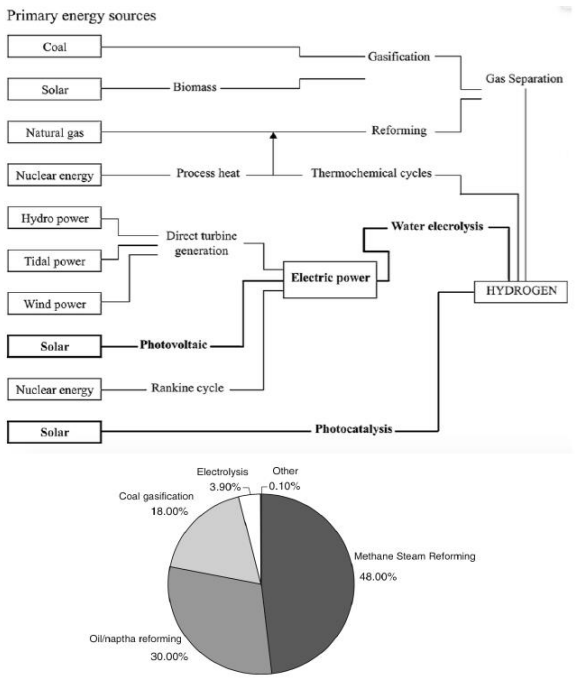

Figure 1-5 Possible Hydrogen production routes [15]

1.3 Solar Water Splitting for Hydrogen Production

As seen from the preceding sections, Hydrogen gas can be considered as an ideal energy carrier. However, the need to find an optimized production route from energy considerations point of view persists. In addition, it has been shown that we must invest in solar energy advancement to be able to face the Terawatt Challenge. This is the root of the idea to use solar energy to split water into Oxygen and Hydrogen; which can be done in two ways: either through incorporation of photovoltaics that can generate electrical energy to a grid used to harvest this energy which is later to be used in water electrolysis, or through photo-assisted electrochemical water splitting, where semiconductors with photoactivity are used as electrodes to split water. Figure 1-6 shows a depiction of the first experiment run by Fujishima and Honda who used TiO_2 as a photoanode that absorbs photons of wavelengths less than 450 nm [17]. An electron hole pair is generated, the hole in the valence band moves to the surface and oxidizes water giving Oxygen, while the electron in the conduction band is transferred by a bias to a Pt counter-electrode to reduce water into Hydrogen. Different combinations may be used, n-type semiconductor as a photoanode and Pt as the counter-electrode, p-type semiconductor as a photocathode and Pt as the counter-electrode, or n-type semiconductor as a photoanode together with p-type semiconductor as a photocathode [18]. Although an efficiency as low as 0.1% was obtained in their experiment, it is still regarded as a very important one as it has opened new horizons for the research community to explore.

Nanostructures and nanomaterials possess interesting properties when compared to their bulk counterpart. Chemical, optical, electrical, mechanical and magnetic properties change due to the increased surface to volume ratio and quantum confinement. Quantum confinement occurs when the material is reduced to a size beyond the Bohr radius, where the density of states become discrete unlike the continuous states in bulk as shown in Figure 1-7. Since materials define the performance limit of applications, and due to the interesting properties of nanomaterials, they are now used in numerous applications such as combustion engines, light-weight applications, gas storage, catalysis, electronics, and others.

To sum up at this point, it seems that the quest to find and develop new materials that satisfy the requirements of the water splitting process is very much needed.

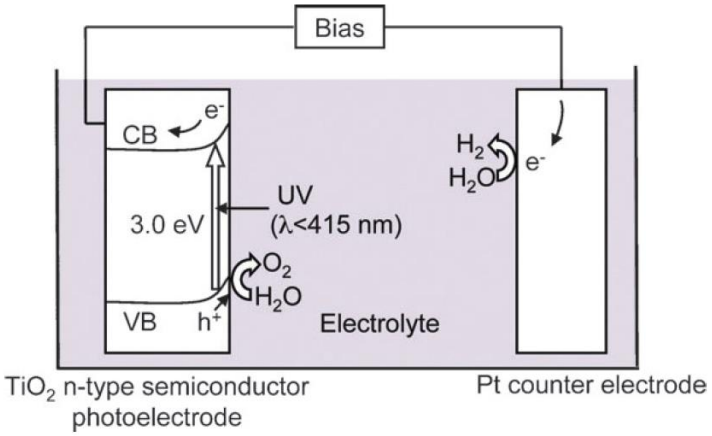

Figure 1-6 Depiction of Fujishima & Honda's experiment [19]

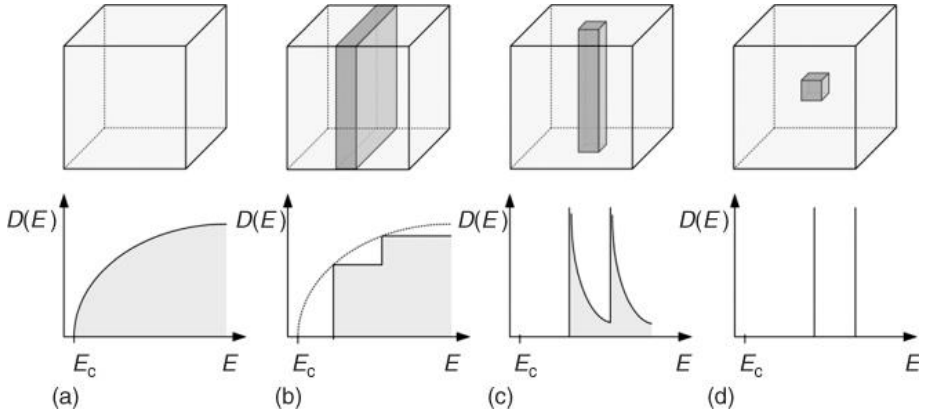

Figure 1-7 Change in density of states as the degree of quantization changes (a) bulk (b) 1D (b) 2D (c) 3D [20]

1.4 Scope of Thesis

As will be discussed thoroughly in chapter 2, for a semiconductor to be selected as a photo anode/cathode, it is required to maximize its absorption, and maintain efficient charge separation.

Chapter 2 provides the essential scientific background that deals with different aspects of photoelectrochemical (PEC) water splitting

Chapter 3 present a review of literature for recent advances in TiO_2 nanotubes, and various approaches to tailor its properties, as well as different CZTS synthesis techniques

Chapter 4 presents a discussion of various fabrication schemes and conditions used throughout thesis, as well as characterization techniques employed.

Chapter 5 presents the formation mechanism of MPNTs and how the morphology tuning has changed the optical and PEC properties.

Chapter 6 presents the results and discussion of annealing the MPNTs in different atmospheres, and the consequent structural, optical and electronic changes. It also presents the results for CZTS nanoparticles deposition on TiNbZr MPNTs annealed in Hydrogen.

Chapter 7 provides conclusion for the main work done in the thesis, and identifies possible opportunities for future work

References

(1) Ausick, P.; Sauter, M. B. The 10 most oil-rich states https://www.usatoday.com/story/money/business/2013/08/03/the-most-oil-rich-states/2613497/ (accessed Dec 11, 2017).

(2) M., K. How is the greenhouse effect related to global warming? https://socratic.org/questions/how-is-the-greenhouse-effect-related-to-global-warming (accessed Dec 11, 2017).

(3) Budget, G. C.; Ciais, P.; Conway, T.; Field, C. B. Carbon Budget. *Carbon*, 2008.

(4) Boger, D. With Global Warming, Delay is Not An Option | World Resources Institute https://www.wri.org/blog/2008/06/global-warming-delay-not-option (accessed Dec 11, 2017).

(5) Grimes, C. A.; Ranjan, S.; Varghese, O. K. *Light, Water, Hydrogen : The Solar Generation of Hydrogen by Water Photoelectrolysis.*; Springer, 2007.

(6) Morse, S. *Sustainability A Biological Perspective*; 2010.

(7) Konikow, L. F.; Kendy, E. Groundwater Depletion: A Global Problem. *Hydrogeol. J.* **2005**, *13*, 317–320.

(8) Zini, G.; Tartarini, P. Solar Hydrogen Energy Systems: Science and Technology for the Hydrogen Economy. *Solar Hydrogen Energy Systems: Science and Technology for the Hydrogen Economy*, 2012, *9788847019*.

(9) United Nations. World population projected to reach 9.8 billion in 2050, and 11.2 billion in 2100 | UN DESA | United Nations Department of Economic and Social Affairs https://www.un.org/development/desa/en/news/population/world-population-prospects-2017.html (accessed Dec 11, 2017).

(10) V3SOLAR http://v3solar.com/about-us/market/ (accessed Dec 11, 2017).

(11) Midilli, A.; Ay, M.; Dincer, I.; Rosen, M. A. On Hydrogen and Hydrogen Energy Strategies I : Current Status and Needs. *Renew. Sustain. Energy Rev.* **2005**, *9*, 255–271.

(12) U.S. Department of Energy. Alternative Fuels Data Center: Hydrogen https://www.afdc.energy.gov/fuels/hydrogen.html (accessed Dec 11, 2017).

(13) Makridis. Hydrogen Storage and Compression. *Methane Hydrog. Energy Storage* **2016**, 1–28.

(14) Royal Society of Chemistry. Hydrogen - Element information, properties and uses | Periodic Table http://www.rsc.org/periodic-table/element/1/hydrogen (accessed Dec 11, 2017).

(15) Sahaym, U.; Norton, M. G. Advances in the Application of Nanotechnology in Enabling a "Hydrogen Economy." *J. Mater. Sci.* **2008**, *43*, 5395–5429.

(16) Nowotny, J.; Sorrell, C. C.; Bak, T.; Sheppard, L. R. Solar-Hydrogen: Unresolved Problems in Solid-State Science. *Sol. Energy* **2005**, *78*, 593–602.

(17) FUJISHIMA, A.; HONDA, K. Electrochemical Photolysis of Water at a Semiconductor Electrode. *Nature* **1972**, *238*, 37–38.

(18) Maitra, U.; Lingampalli, S. R.; Rao, C. N. R. Artificial Photosynthesis and the Splitting of Water to Generate Hydrogen. *Curr. Sci.* **2014**, *106*, 518–527.

(19) Kudo, A.; Miseki, Y. Heterogeneous Photocatalyst Materials for Water Splitting. *Chem. Soc. Rev.* **2009**, *38*, 253–278.

(20) Rafailov, E. *The Physics and Engineering of Compact Quantum Dot-Based Lasers for Biophotonics*; Wiley, 2014.

Chapter 2

Scientific Background

In this part of the thesis, a brief review of the scientific background is presented. Fundamentals about solar irradiation, the PEC water splitting process, as well as semiconductors requirements are reviewed. Then, a brief description of synthesis techniques used throughout the thesis is offered.

2.1 Electromagnetic Solar Spectrum

The sun is the main supplier of heat and light on planet earth. Being a star, and due to the nuclear fusion of large amounts of Hydrogen and Helium, a wide spectrum of energy is released by the sun. Solar irradiance is defined as the power of the electromagnetic waves emitted by the sun and reaching the earth per unit area, measured in kW/m^2. Many factors influence the power density reaching the earth including: climate conditions, geographical nature of the place where the measurement is being taken, the sun position which depends on the time of the measurement during the day, and the air mass that electromagnetic radiations travel through. It has been shown that the presence of gases, vapours, dust, and particles in the atmosphere where the radiation travels influences the power density due to their interaction with the electromagnetic waves through absorption and scattering [1]. Therefore, a term is proposed that includes this power loss in order to adequately describe solar irradiance, which is the Air Mass number (AM) shown in 2-1

$$AM = \frac{1}{\cos\theta} \qquad 2\text{-}1$$

where θ is the angle between the vertical line at normal incidence and the modified line at non-normal conditions. In order to set a reference, three known standards are used for laboratory experiments namely: AM 1.5, AM 1 and AM 0 as displayed in Figure 2-1 (a). AM0 refers to spectral irradiance at normal incidence at the top of the atmosphere, AM 1 is the same irradiance but taken at sea level, while AM 1.5 is the yearly average irradiance in all states of the US, where θ is taken to be equal 48.2^o. The normalized spectral irradiance corresponding to the AM 1.5 standard is 1 kW/m^2. Practically, a Xenon lamp is used in experiments along with AM 1.5 filter to avoid inconsistencies [2].

As shown in Figure 2-1 (b), the electromagnetic radiation is composed of ~52% Infrared of wavelengths longer than 700 nm, ~45% Visible of wavelengths in the range 400-700 nm,

and only 3% ultraviolet of wavelengths shorter than 400 nm. It is thus preferable to have a semiconductor of narrow bandgap to absorb most of the solar spectrum as wide bandgap will have the limitation of absorbing only 3% of the entire solar spectrum. But as the discussion progresses, it will become evident that other factors contribute to material selection.

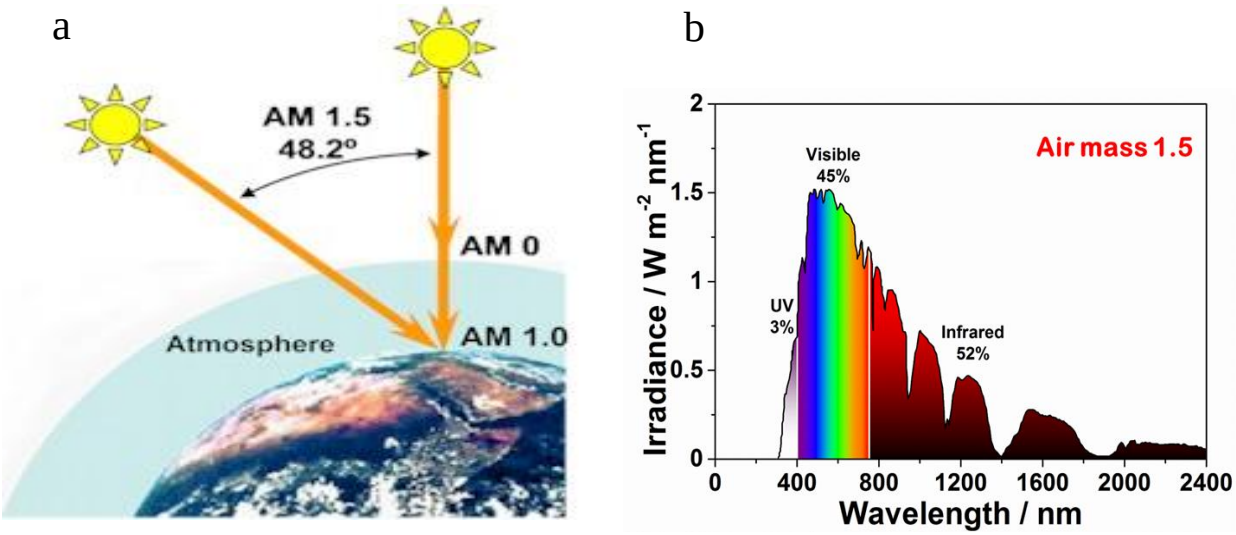

Figure 2-1 (a) Different spectral irradiance standards [3] *(b) Irradiance of AM 1.5* [4]

2.2 Photoelectrochemical Water Splitting - Energy Considerations

Water splitting is non-spontaneous and energy consuming, i.e. it is an endothermic process as expressed in 2-2. The Gibb's free energy ΔG associated with the reaction would be a positive quantity of approximately 237.14 kJ/mol for one mole of reactants at standard conditions of 1 atm pressure and 298.15° K [5]. The standard potential E required to drive a two-electron transfer reaction $(n = 2)$ is calculated by 2-3 to give 1.23 V, given that the charge of 1 mole of electrons is equal to Faraday's constant F. However, in a typical experiment, a greater bias value of ~1.6 is used, to compensate for losses originating from the electrolyte resistance, ohmic losses, carrier recombination and other possible losses.

$$H_2O + energy \rightarrow \frac{1}{2}O_2(gas) + H_2(gas) \qquad 2\text{-}2$$

$$\Delta G^0 = -nFE \qquad 2\text{-}3$$

In PEC water splitting, ideally, it is required to identify a semiconducting material that can provide this amount of voltage through light absorption keeping the additional bias minimized, or better yet without any external bias. This is quite challenging, given that the

process of PEC water splitting is sequential, throughout which many losses occur. To understand the steps involved in the PEC, a schematic of a common lab use quartz PEC cell is shown in Figure 2-2, comprising of three electrodes: the working electrode or the photoanode, a counter electrode and a reference electrode. Due to the high resistance of water, as well as its relatively low absorption coefficient[6], it cannot be used directly, but instead an electrolyte with salts is selected keeping in mind pH considerations which will be discussed later. Frequently, electrolyte refreshment maybe needed, so a circulation system is added.

Light is illuminated upon the photoanode and the PEC process is carried out in the following steps:

1- The photoanode absorbs photons of energy equal to or greater than its bandgap. Upon absorption, electrons are excited to the conduction band and there are un-neutralized holes in the valence band that are free to move to the surface as shown in 2-4

$$2h\nu \rightarrow 2e^- + 2h^+ \qquad 2\text{-}4$$

2- The holes, now at the interface between the electrode and the electrolyte, can oxidize water giving oxygen gas and positive H^+ as shown in (gas)

$$2h^+ + H_2O\ (liquid) \rightarrow 2H^+ + \frac{1}{2}\ O_2\ (gas) \qquad 2\text{-}5$$

3- The positive H^+ move in the electrolyte to the counter electrode where they are reduced by the conduction band electrons transferred by the bias, as shown in 2-6

$$2H^+ + 2e^- \rightarrow\ H_2(gas) \qquad 2\text{-}6$$

The net reaction is shown in 2-7

$$2h\nu +\ H_2O(liquid) \rightarrow \frac{1}{2}\ O_2(gas) +\ H_2(gas) \qquad 2\text{-}7$$

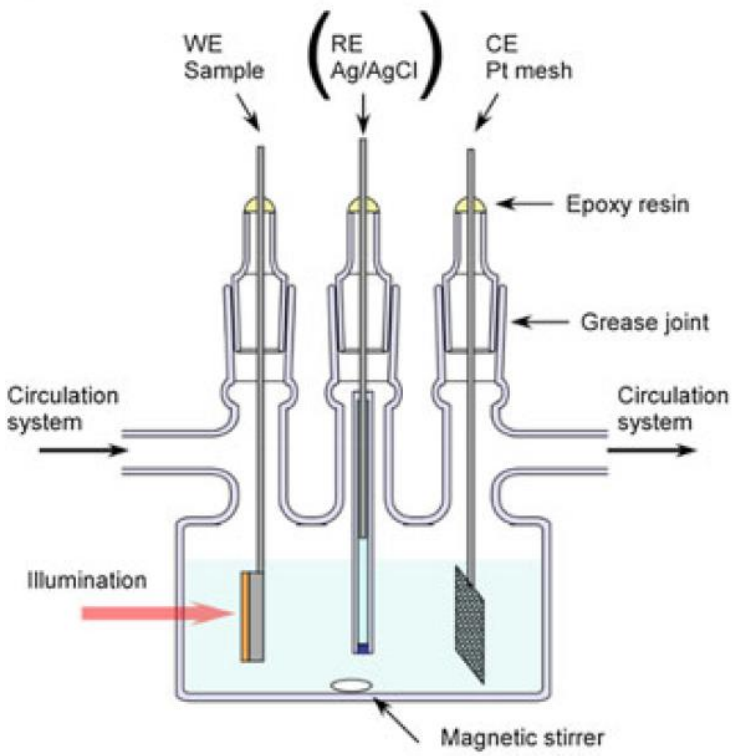

Figure 2-2 Typical PEC cell setup including the three electrodes and a circulation system [2]

Considering an n-type semiconductor/photoanode, the energy band diagrams of the water splitting process is further explained in Figure 2-3. Before contact, the fermi level of the semiconductor is close to the conduction band (CB), due to the unequal probability of finding electrons in the CB and holes in the valence band (VB); while the fermi level of the electrolyte will lie between the potentials of oxidation and reduction (Figure 2-3 a). On bringing the photoanode in contact with the electrolyte and the metal, and since the photoanode has fermi level that is more cathodic than that of the electrolyte, electrons transfer from the CB to the electrolyte, resulting in formation of a region that is depleted of electrons rendering un-neutralized positive donor ions, which re-orient the electrolyte ions forming a capacitive Helmholtz layer. An electric field builds up and consequent voltage drop is formed, referred to as band bending (Figure 2-3 b) [7]. The width of the resulting depletion region is expressed in 2-8, where e is electron charge, N_D is the donor states density, ε is the material permittivity, ε_0 is the free space permittivity, $V_{applied}$ is the applied bias, V_{FB} is the flat band potential which is the potential of the fermi level before bending occurs. By electrochemical impedance spectroscopy, and considering that the space charge region and the Helmholtz layer are capacitive, then using the Mott-Schottky relation (2-9), one is able to calculate V_{FB} and N_D (2-

10). The fermi levels of the semiconductor and the electrolyte are now aligned with the metal work function, equilibrium is established, and no charge transfer will occur. Upon illumination (Figure 2-3 c), more electrons are excited to the CB leaving holes in the VB, the band bending is decreased, and with aid of the built-in electric field, electrons and holes cannot recombine, as electrons are swept towards the bulk, while holes move to the electrolyte. Since the holes are at lower potential than that of H_2O/O_2 reaction, they will be able to move to that potential. However, the reaction of water splitting will not proceed, since the electrons are still at a lower potential than that of the H^+/H_2 reaction, therefore and external bias (over potential) is needed to break that equilibrium and force them to move to the metal work function that is now at potential higher than that of the H^+/H_2 reaction, and the water splitting reaction can finally proceed (Figure 2-3 d) [7].

$$W_{SC} = \sqrt{\frac{2\varepsilon\varepsilon_0}{eN_D}}\sqrt{(V_{applied} - V_{FB})} \qquad 2\text{-}8$$

$$\frac{1}{C^2} = \frac{2}{N_D\varepsilon\varepsilon_0 e}[(V - V_{FB}) - \frac{kT}{e}] \qquad 2\text{-}9$$

$$N_D = -[\frac{2}{\varepsilon\varepsilon_0 e}][\frac{d(1/C^2)}{d(V)}]^{-1} \qquad 2\text{-}10$$

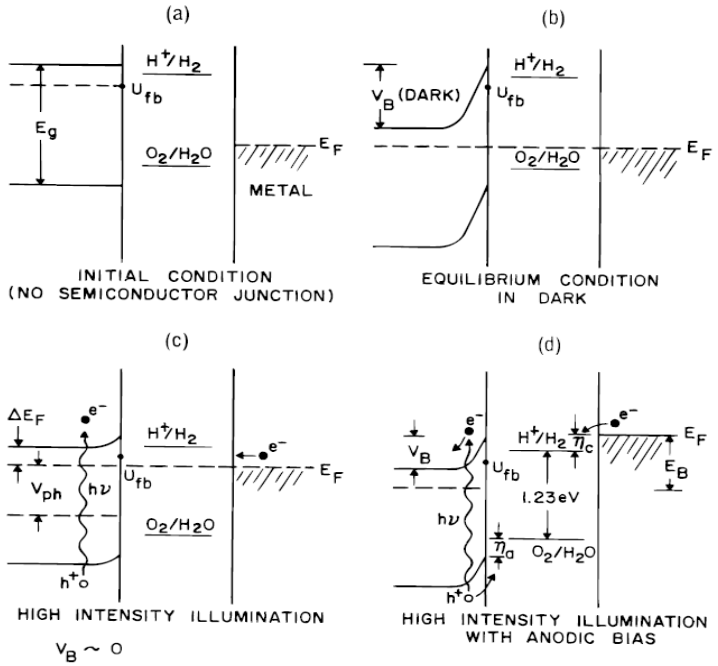

Figure 2-3 PEC water splitting mechanism using a photoanode and a metal as the cathode/counter electrode (a) before contact (b) after contact (c) under illumination (d) under illumination and external bias [7]

2.3 Photoelectrochemical Water Splitting - Material Considerations

Following that discussion, a decision can be made regarding the criteria of photoanode selection:

2.3.1 Bandgap

It is preferable to have a semiconductor of narrow bandgap to enable it to absorb most of the solar spectrum in the visible or NIR region. However, narrow bandgap semiconductors such as CdS[8], often suffer from stability problems which will be discussed in section 2.3.3. Therefore, band tuning of wide bandgap metal oxides is of great interest.

2.3.2 Band Edge Positions

CBM and VBM must straddle the oxidation and reduction potentials of water to make the water splitting reaction thermodynamically favourable and avoid the need for large overpotentials, as holes move to higher energies while electrons move to lower energies. The band alignment of various wide and narrow bandgap semiconductors relative to water redox potentials at pH=0 relative to the Normal Hydrogen Electrode NHE is shown in Figure 2-4; it is obvious that most narrow bandgap semiconductors do not always straddle water redox potentials. It is also worth mentioning that the band alignment is dependent on the pH of the electrolyte, some semiconductors have band edge positions that straddle the redox potentials only in certain pH value as the case of TiO2 shown in Figure 2-5 .

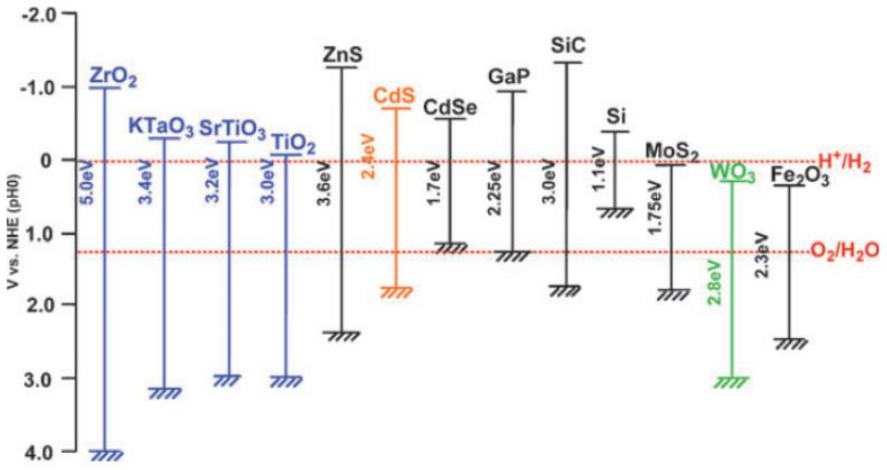

Figure 2-4 Band edge positions of some straddling and non-straddling semiconductors [9]

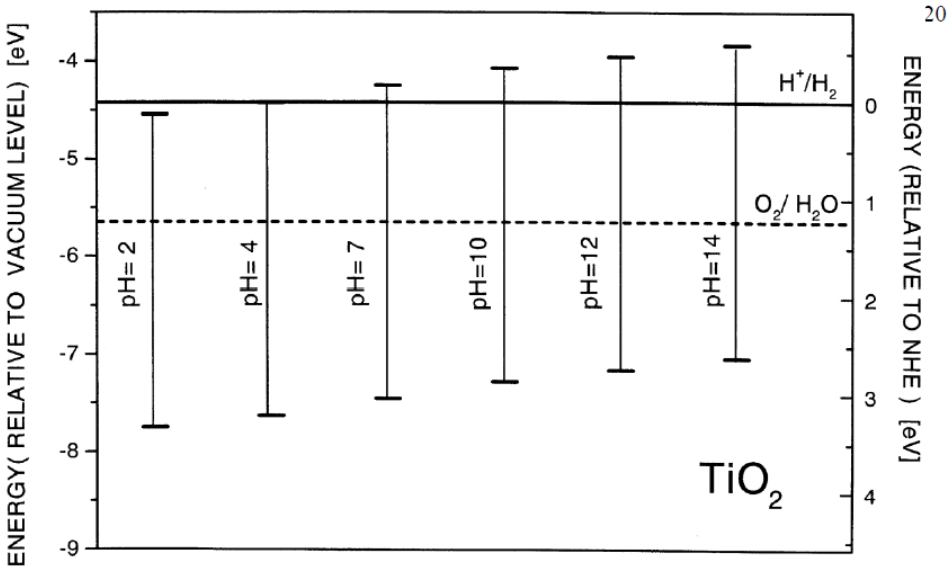

Figure 2-5 Band edge positions of TiO_2 at different pH relative to vacuum level and NHE [10]

2.3.3 Stability and Resistance to Corrosion

For a semiconductor to be suitable for use in water splitting, it must be stable in the electrolyte, i.e. the holes must thermodynamically favour water oxidation over self-oxidation and electrons must holes must thermodynamically favour Hydrogen reduction over self-reduction [11]. This will be achieved when the conditions in 2-11 & 2-12 are satisfied, where the free enthalpy of oxidation $E_{p,d}$ is less than the OER potential; and the free enthalpy of reduction $E_{n,d}$ is greater than the HER potential. Figure 2-6 shows the decomposition potentials of various semiconductors, it is obvious that most wide bandgap semiconductors are stable while most narrow bandgap semiconductors suffer from stability issues.

$$E(O_2/H_2O) < E_{p,d} \qquad 2\text{-}11$$

$$E(H^+/H_2) > E_{n,d} \qquad 2\text{-}12$$

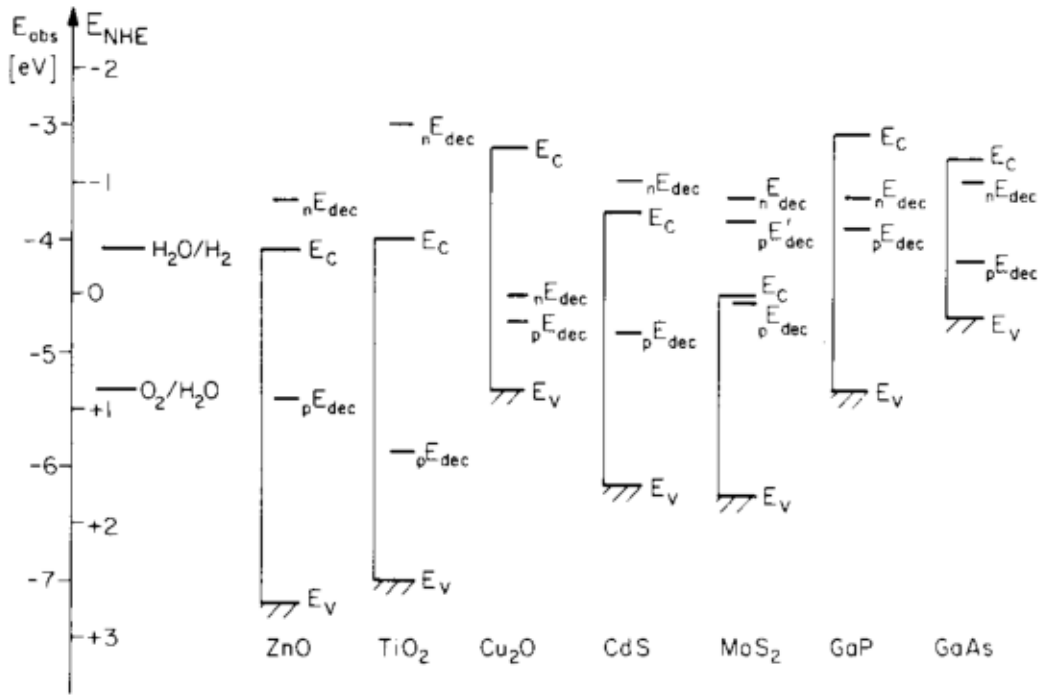

Figure 2-6 Decomposition potentials of some semiconductors versus water redox potentials relative to vacuum scale and NHE [11]

2.3.4 Electronic and Structural Considerations

In water splitting process, it is important to collect all the photogenerated charge carriers and minimize recombination. Therefore, possible recombination centres (Figure 2-7) such as structural defects whether vacancies, interstitials, grain boundaries, and surface trap states must be curtailed [12]. Structural defects introduce new allowed energy states in the previously forbidden bandgap, which act as electron traps and therefore hinders the photocurrent [13]. To be specific, there are two types of defects: shallow and deep defects. Deep defects lie far away near mid-gap and are main electron traps; on the other hand, shallow defects are defect states that lie close to the CBM, and could be in favour of the water splitting reaction as they will easily be transferred to the CB because of the small energy difference [12]. Moreover, ionized surface trap states, which are present due to reactive surface sites, attract charge carriers from bulk and could result in a phenomenon known as Fermi level pinning, which prevents carrier diffusion [7].

The presence of defects in the material is a result of the fabrication process that can be used to tune the density of defect states. Although nanostructuring increases the

surface area which is desirable for the water splitting reaction due to the presence of many active sites, it may come on the expense of increasing the surface states resulting in fermi level pinning or increasing the possibility of surface recombination. A way of overcoming this problem is the attempt to form thin-walled nanotubes and hollow nanofibers whose thickness is equal to or less than the diffusion length of the minority carriers [15] (2-13). The minority carrier diffusion is the considered the rate determining step[16]. This way, the charge collection probability increases as well as light trapping in the tube length.

$$L_D = \sqrt{D\tau} \qquad 2\text{-}13$$

where L_D is the minority carrier diffusion length, D is the diffusion coefficient and τ is the minority carrier life time.

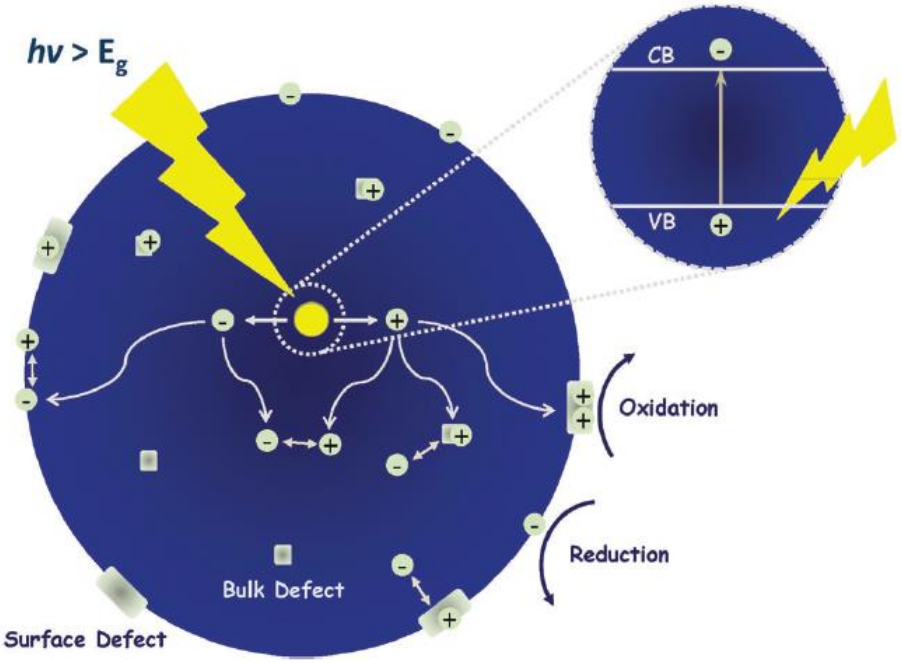

Figure 2-7 Photocarrier generation and various defects in the crystal that could act as recombination centres [17]

To sum up at this point, wide bandgap semiconductors possess properties that are desirable for the PEC water splitting reaction such as stability and resistance to corrosion; however, attempts need to be made in order to overcome the wide bandgap problem to tune the bandgap and enhance the absorption, such as nanostructuring, doping and defect introduction.

References

(1) Murphy, A. B.; Barnes, P. R. F.; Randeniya, L. K.; Plumb, I. C.; Grey, I. E.; Horne, M. D.; Glasscock, J. A. Efficiency of Solar Water Splitting Using Semiconductor Electrodes. *Int. J. Hydrogen Energy* **2006**, *31*, 1999–2017.

(2) Chen, Z.; Dinh, H. N.; Miller, E. *Photoelectrochemical Water Splitting: Standards, Experimental Methods, and Protocols*; 2013.

(3) National Science Foundation. V. Air Mass - SolarWiki https://photon.libretexts.org/The_Science_of_Solar/Solar_Basics/B._Basics_of_the_Sun/V._Air_Mass (accessed Dec 12, 2017).

(4) Norena, L.; Wang, J. *Advanced Catalytic Materials - Photocatalysis and Other Current Trends*; Intech, 2016.

(5) O'Hayre, R.; Cha, S.; Colella, W.; Prinz, F. *Fuel Cell Fundamentals*; Wiley, 2016.

(6) Grimes, C. A.; Ranjan, S.; Varghese, O. K. *Light, Water, Hydrogen : The Solar Generation of Hydrogen by Water Photoelectrolysis.*; Springer, 2007.

(7) Nozik, a. J.; Memming, R. Physical Chemistry of Semiconductor - Liquid Interfaces. *J. Phys. Chem.* **1996**, *100*, 13061–13078.

(8) Ellis, A. B.; Kaiser, S. W.; Wrighton, M. S. Visible Light to Electrical Energy Conversion. Stable Cadmium Sulfide and Cadmium Selenide Photoelectrodes in Aqueous Electrolytes. *J. Am. Chem. Soc.* **1976**, *98*, 1635–1637.

(9) Kudo, A.; Miseki, Y. Heterogeneous Photocatalyst Materials for Water Splitting. *Chem. Soc. Rev.* **2009**, *38*, 253–278.

(10) Nowotny, M. K.; Sheppard, L. R.; Bak, T.; Nowotny, J. Defect Chemistry of Titanium Dioxide. Application of Defect Engineering in Processing of TiO_2-Based Photocatalysts. *J. Phys. Chem. C* **2008**, *112*, 5275–5300.

(11) Gerische, H. Electrolytic Decomposition and Photodecomposition of Compound Semiconductors in Contact with Electrolytes Heinz. *J. Vac. Sci. Technol.* **1978**, *15*, 1422–1428.

(12) Allam, N. K. An Investigation Into The Doping And Crystallinity Of Anodically Fabricated TiO_2 Nanotube Arrays: Towards An Efficient Material For Solar Energy Applications., 2009.

(13) Hagfeldt, A.; Grätzel, M. Light-Induced Redox Reactions in Nanocrystalline Systems.

Chem. Rev. **1995**, *95*, 49–68.

(14) Walter, M. G.; Warren, E. L.; McKone, J. R.; Boettcher, S. W.; Mi, Q.; Santori, E. A.; Lewis, N. S. Solar Water Splitting Cells. *Chem. Rev.* **2010**, *110*, 6446–6473.

(15) Hautier, G.; Miglio, A.; Ceder, G.; Rignanese, G.-M.; Gonze, X. Low Hole Effective Mass P-Type Transparent Conducting Oxides: Identification and Design Principles. *Nat. Commun.* **2013**, *4*, 1–7.

(16) Yan, J.; Wu, G.; Guan, N.; Li, L.; Li, Z.; Cao, X. Understanding the Effect of Surface/bulk Defects on the Photocatalytic Activity of TiO2: Anatase versus Rutile. *Phys. Chem. Chem. Phys.* **2013**, *15*, 10978.

Chapter 3

Literature Review

The use of nanomaterials in different applications is becoming more popular due to their desired properties which are highly dependent on the size and quantization; such as: high surface to volume ratio, enhanced mechanical properties and controlled pathway of charge transfer [1]. Many studies are focused on metal oxides and their use in numerous electronic, catalytic, and biomedical applications due to their low cost, abundance and stability [2,3,4,5,6]. Titanium dioxide is regarded as a very promising material that can be used in different applications [7]. Fujishima and Honda's work on TiO_2 as possible photocatalyst to be used in PEC water splitting[8] has opened the doors for many extensive research on it (Figure 3-1) and other metal oxides and their use in water splitting [9,10,11].

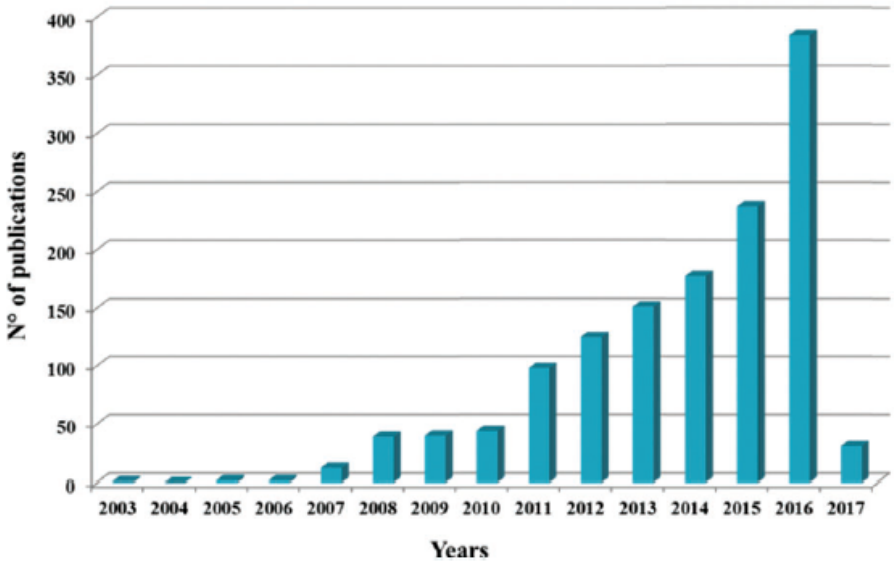

Figure 3-1 Number of publications on Titania Nanotubes over the past few years [12]

There are two major problems faced when looking for a suitable photoanode: carrier recombination that hinders the photocurrent, and limited absorption due to the wide band gap problem present in most metal oxides. Different approaches have been previously adopted in order to find possible effective pathways to modify and tune the properties of TiO_2 to match the application demands. TiO_2 has a wide bandgap (~3.0 eV when it is in the Rutile structure, and 3.2 eV when it is in Anatase) which limits its absorption to the UV region hindering the

efficiency of the PEC water splitting reaction to theoretical values of 2.2% and 1.3% for Rutile and Anatase respectively [13]. Accordingly, it is desirable to red-shift the absorption edge towards lower frequencies in the NIR/Vis range. This band gap tuning/engineering can be achieved through doping and annealing in different atmospheres.

Another problem is the recombination and carriers' scattering, which greatly reduces the photocurrent and decrease efficiency. Therefore, it is desirable to control the pathways of charge carriers to minimize recombination and reinforce the charge collection probability. This can be attained through nanostructuring and decoration where charge injection can compensate the carriers lost during the recombination process. Doping as well can help enhance carrier mobility by modifying the band egde positions. The previous is discussed in detail below.

3.1 Nanostructuring

As previously discussed, nanomaterials are showing very interesting properties owing to the quantization effect. Accordingly, the degree of quantization controls the material properties. Therefore, properties of nanoparticles differ from those of nanosheets or nanotubes/nanorods. For instance, on examining the performance of nanoparticles in DSSC, where high dye loading is desired on the surface of the TiO_2 thin film, they become perfect for the application[14]. However, the decreased crystallinity, non-uniformity and larger number of grain boundaries cause charge carrier scattering and make carriers more prone to recombination (Figure 3-2 a); which is undesirable in the PEC water splitting process[15]. Nanotubes and nanorods provide a great solution for this problem by separating the pathways of the electron and holes supressing recombination. Holes move horizontally to the surface to participate in the OER; while electrons move vertically towards the bulk as shown in Figure 3-2 b. Nanotubes are preferable to nanowires as they offer a decreased wall thickness and a shorter path (ultimately less than the hole diffusion length) thus allowing for comparatively facile hole transport to the surface compared to nanowires. Also, nanotubes can by synthesized to be more ordered. In addition, nanowires are generally very long, with increased resistivity and more recombination centres [16].

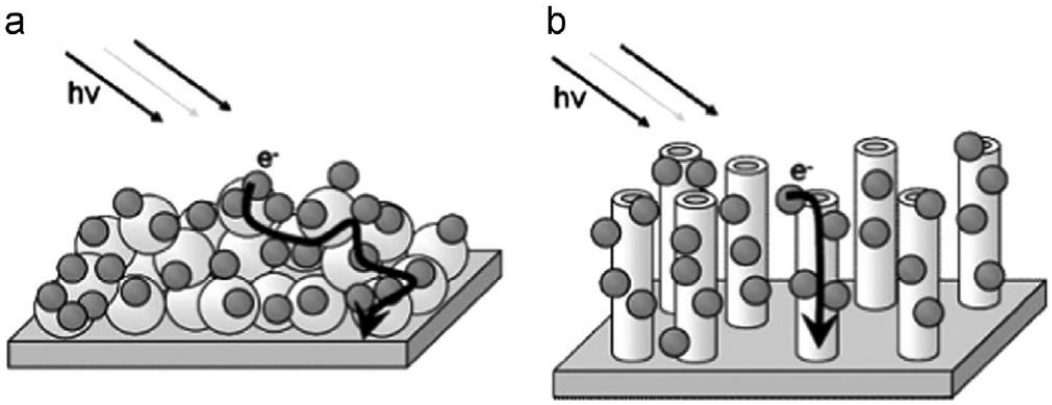

Figure 3-2 Electron transport in (a) particles (b) nanotubes [17]

The multipodal morphology has proven to possess remarkable features making it suitable for use in light harvesting applications owing to its graded refractive index decreasing the Fresnel reflectance and its enhanced light scattering according to Mie scattering theory [17–20]. Mohammadpour et al. reported the formation of TiO_2 MPNTs by anodization in diethylene glycol (DEG)-based electrolyte containing Hydrogen Flouride (HF) for 45 hours as shown in Figure 3-3 [20]. Rambabu et al. used DEG-based electrolyte with HF and ammonium fluoride for 2 hours to synthesize TiO_2 MPNTs [17]. However, there are no reports present on the synthesis of complex oxide MPNTs. It is known that compact oxide barrier films form when the oxide is insoluble in the anodization bath, and porous films when it is moderately soluble[21]. In addition, Formamide-based electrolyte was used by Allam et al. to produce vertically oriented $Ti_{35}Nb_5Zr$ nanotubes of tube lengths up to 7um[22]. Therefore, a formamide-based electrolyte is used to produce the complex MPNTs of the alloy in hand.

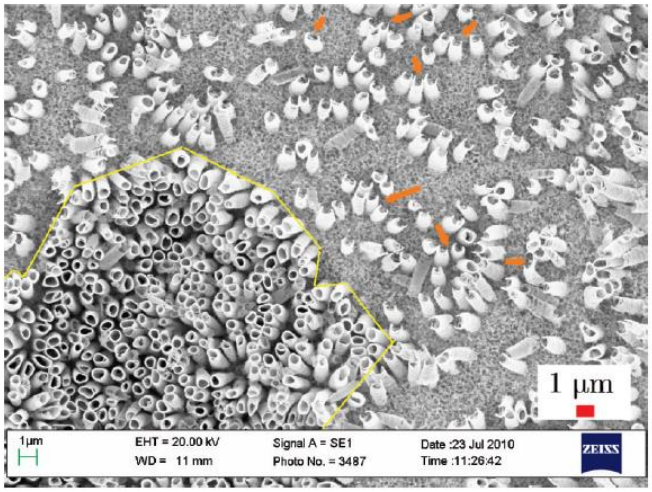

Figure 3-3 SEM of TiO_2 MPNTs synthesized in DEG-based electrolyte [20]

3.2 Doping

Doping can be performed to either enhance charge separation or tailor the band gap. In addition to sputtering, ion implantation and other clean-room based techniques, doping can be obtained through using alloying. When thinking of band gap reduction, it is thought of incorporating cations in the lattice with another cation of lower d orbital energies than that of Ti^{4+} (Figure 3-4 a). On the other hand, one could possibly replace oxygen anions with anions of higher atomic 2p or 3p orbital energies than that of O to raise the VBM (Figure 3-4 b). DFT calculations show that (Ta, N), (Nb, N),(Mo, N) and (W, N) are optimum for engineering TiO2 to meet band gap, optical absorption, band edge positions, and mobility criteria[23]. Moreover, binary and ternary Titanium-based alloys possibly enhance charge generation and separation, which is employed to introduce donor and acceptor defects and enhance the charge carrier density. In this sense, Nb is considered as a donor impurity[24]; while Zr doping is expected to shift the CBM towards vacuum level and maintain carrier mobility[23].

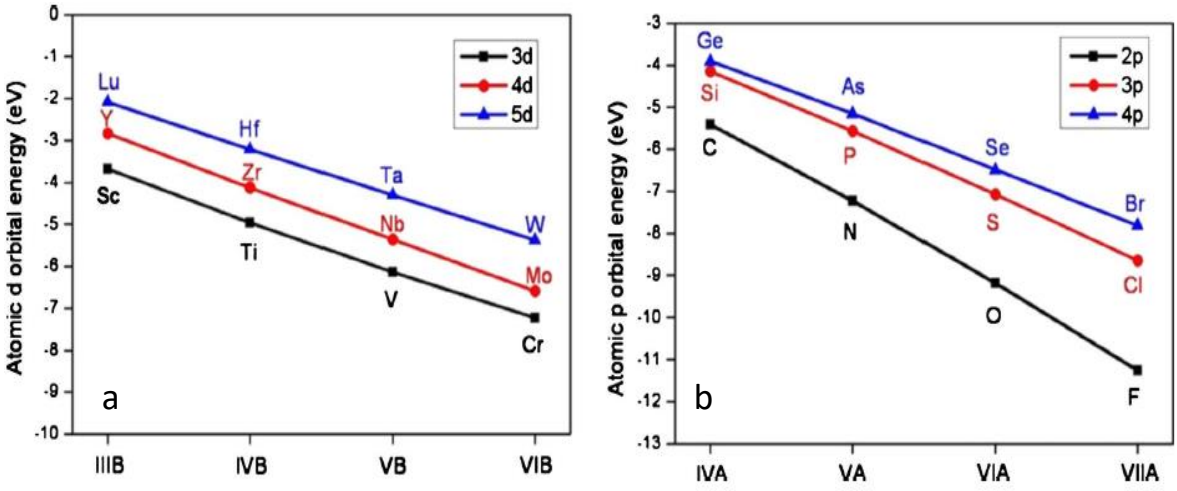

Figure 3-4 Atomic (a) d orbitals energy levels and (b) p orbitals energy levels of various cations and anions [23]

As discussed before, enhancing the crystallinity can greatly reduce recombination; accordingly, annealing at different temperatures, atmospheres, and times can greatly influence the electrical, photoelectrochemical and mechanical properties of the material [25–31]. Annealing can be considered at times as a form of doping when carried out under different atmospheres. It has a great influence on the conductivity as shown in Figure 3-5 **.** it also controls phase transformation and crystallinity [26].

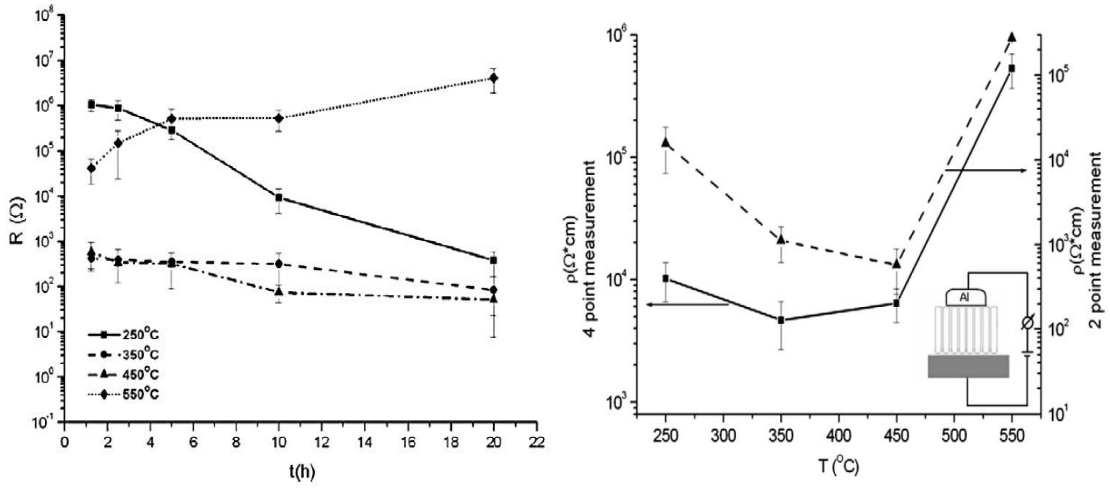

Figure 3-5 Effect of annealing time and temperature on the conductivity of 1um long TiO_2 nanotubes [26]

It has been also shown that annealing under different atmospheres can induce electronic structure modification and band gap tuning. For instance, Allam et al. have shown that Ammonia annealing of Niobium microcones incites bandgap reduction due to Oxygen substitution by Nitrogen which has 2p orbitals of higher potential energy than that of oxygen[29]. Taga et al. firstly reported enhanced TiO_2 absorption through Nitrogen doping[32], shown in Figure 3-6.

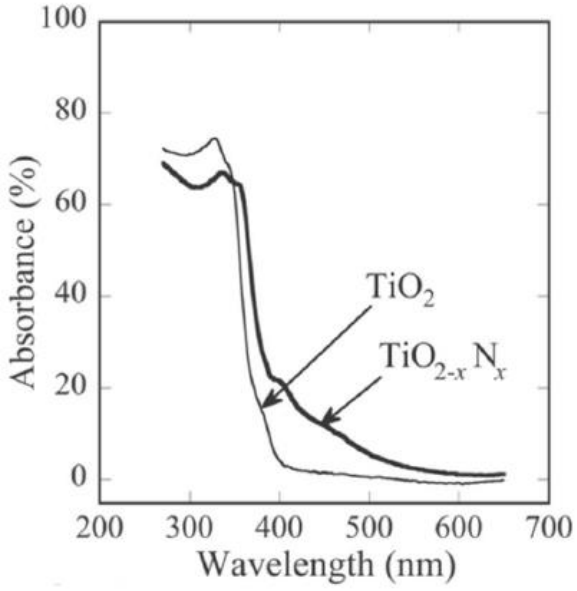

Figure 3-6 Comparison between the absorption of doped $TiO_{2-x}N_x$ and undoped TiO_2 [32]

One of the very interesting band-tuning techniques is annealing in a reducing atmosphere. DFT calculations showed that new allowed gap states are introduced in the bandgap by the disordered structure formed through bonding one Hydrogen atom to Titanium and another Hydrogen atom to Oxygen in a process known as Hydrogenation [33]. This can be used as another way to overcome the wide bandgap problem of TiO_2 and shift the absorption towards visible region as shown in Figure 3-7 a. The introduced states are referred to as CB and VB tail states with the valence band tailing being strong and is formed by Oxygen 2p orbitals hybridization with Titanium 3d orbitals. On the other hand, the CB tail states are formed by 3d orbitals only (Figure 3-7 b).

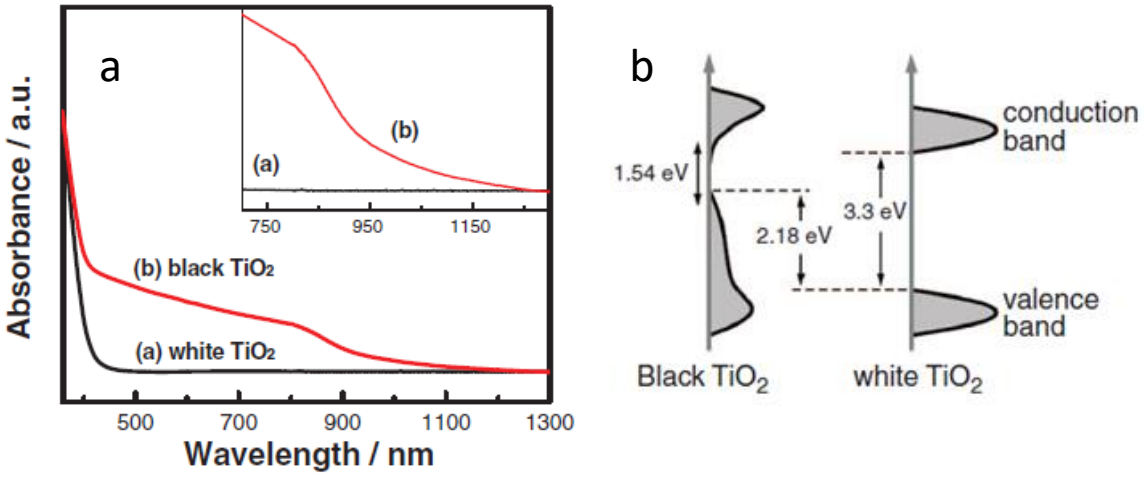

Figure 3-7 (a) Absorption shift introduced by the band tails (b) Schematic of the new density of states on the left compared to conventional Titania density of states [33]

It has been shown that annealing in a reducing atmosphere, results in the formation of Oxygen vacancies and/or Titanium interstitials, accompanied by the formation of Ti^{3+}, which cause a contraction in the lattice decreasing crystallinity [34]. Although the decreased crystallinity is expected to increase the recombination sites, the band gap reduction still persisted which is promising in photoelectrochemical water splitting. Also, Wang et. Al, discussed the formation of Ti^{3+} during Hydrogen annealing and detailed defect positions formed by it (Figure 3-8), which are 0.7-1 eV lower than the CBM. They have also showed that electronic transitions between the VB tails and the localized oxygen vacancies as well as transitions between the localized oxygen vacancies and CB contribute to NIR absorption [35]. Moreover, Li et al. suggested that in order for Ti^{3+} defects to be effective in the water splitting process and contribute to the carrier density, they must exist in bulk not on the surface, to prevent their

oxidation by VB holes [36]. Finally, Tusi et al. suggested that Hydrogen annealing causes passivation of surface states that act as trap/recombination centres increasing the carrier density [37].

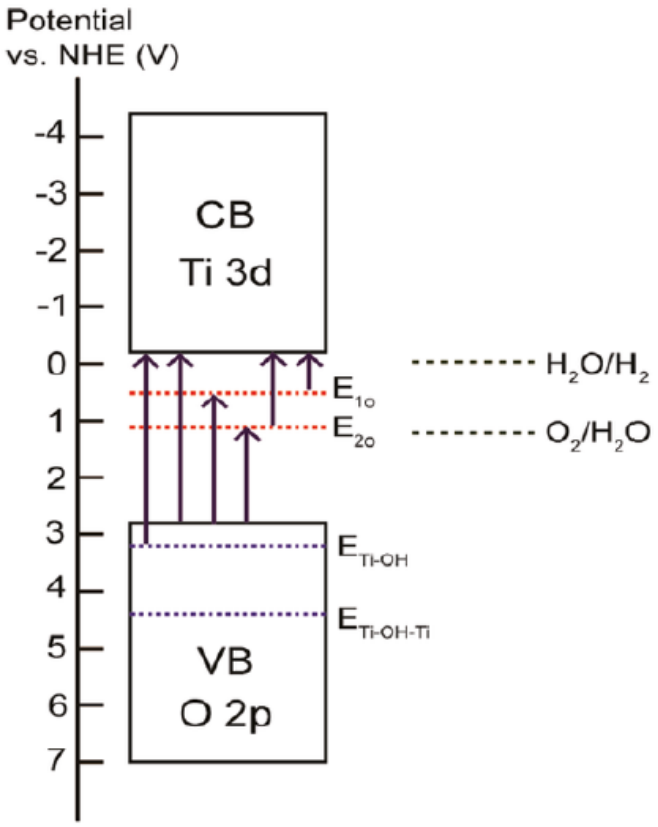

Figure 3-8 E_{10} & E_{20} are Oxygen vacancies present at 0.7-1 eV below the CB [35]

It is also worth mentioning that the concept of oxide reduction has been discussed with other metal oxides. For example, Sinhamahapatra et al. confirmed the presence of VB tail states in black ZrO_{2-x} formed by hybridization of O 2p and Zr 4d, which greatly reduced the bandgap from 5.09 eV to 1.52 eV [38]. Moreover, Liu et al., using DFT calculations, proved that the VB of Anatase doped with Nb will be formed by hybridization of Oxygen 2p and Nb 4d [39]. It is then acceptable to expect that on annealing the alloy in hand in a reducing atmosphere, VB tail states will merge and perhaps CB tail states too; where the aforementioned VB tail states will be formed by O 2p orbitals hybridization with Ti 3d, Zr 4d, and Nb 4d, while the CB tail states will be formed by the transition metals' d orbitals.

3.3 Decoration & Coupling

Many reports in literature discuss the decoration of Titania nanotubes with other Many reports in literature discuss the decoration of Titania nanotubes with other materials of desired properties to overcome the problems discussed earlier. One of the decorating elements used in literature are noble metal (such as Gold and Silver) plasmonic nanoparticles and quantum dots for enhanced antibacterial effect [40] and enhanced photocatalytic activity in the visible range[41]. In addition, quite often semiconductor nanoparticles of a narrow bandgap are coupled with Titania nanotubes to enhance the absorption, increase charge separation efficiency and enhance charge injection facilitated by the relative band alignment to increase the carrier density. For example, Tsui et al. used electrodeposition method to deposit n-type and p-type Cu_2O on TiO_2 nanotubes, and obtained a fourfold enhancement in the photocurrent[42]. Yun et al. used ternary p-type $CuInS_2$ for improving light absorption and trapping resulting in improved photoelectrochemical performance[43]. However, very few reports are present on the use of quaternary CZTS with metal oxide nanotubes and to our knowledge there are no reports on the coupling of CZTS with multinary metal oxides. Zhang et al. used electrophoresis to deposit $(Cu_2Sn)_{x/3}Zn_{1-x}S$ with x= 0.75, 0.24, and 0.09 on TiO_2 nanotubes. Figure 3-9 shows the J-V plots obtained at different stoichiometry, with the highest photocurrent at x=0.09. They have attributed this enhancement to the type II alignment shown in Figure 3-10 enhancing charge separation efficiency; where the higher the offset between the CZTS CBM and that of TiO_2, the higher the achieved photocurrent [44].

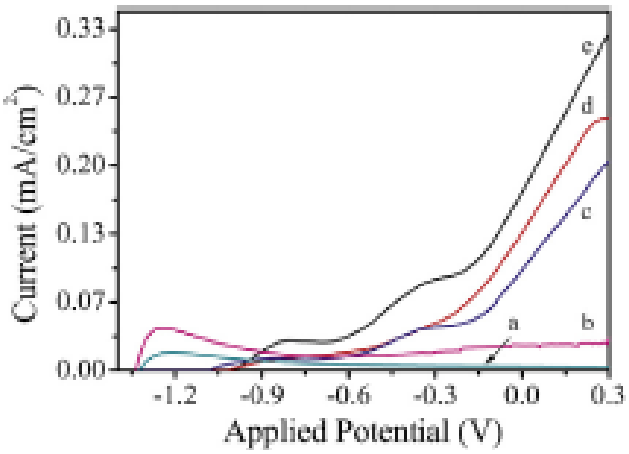

Figure 3-9 J-V plots of TiO_2 nanotubes (a)in dark (b) under light; and TiO_2 nanotubes with $(Cu_2Sn)_{x/3}Zn_{1-x}S$ (c) x=0.75 (d) x=0.24 and (e)x=0.09 [44]

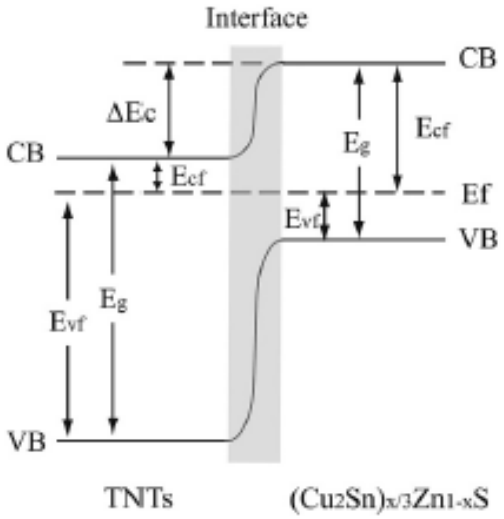

Figure 3-10 Energy band diagram showing the relative alignment of band edge positions of $(Cu_2Sn)_{x/3}Zn_{1-x}S$ and $(Cu_2Sn)_{x/3}Zn_{1-x}S$ [44]

References

(1) Grimes, C. A.; Ranjan, S.; Varghese, O. K. Light, Water, Hydrogen : The Solar Generation of Hydrogen by Water Photoelectrolysis., 2007.

(2) Zhang, X.; Zhang, B.; Zuo, Z.; Wang, M.; Shen, Y. N/Si Co-Doped Oriented Single Crystalline Rutile TiO_2 Nanorods for Photoelectrochemical Water Splitting. *J. Mater. Chem. A* **2015**, *3*, 10020–10025.

(3) Ham, Y.; Hisatomi, T.; Goto, Y.; Moriya, Y.; Sakata, Y.; Yamakata, A.; Kubota, J.; Domen, K. Flux-Mediated Doping of $SrTiO_3$ Photocatalysts for Efficient Overall Water Splitting. *J. Mater. Chem. A* **2016**, *4*, 3027–3033.

(4) Li, C.-T.; Li, S.-R.; Chang, L.-Y.; Lee, C.-P.; Chen, P.-Y.; Sun, S.-S.; Lin, J.-J.; Vittal, R.; Ho, K.-C. Efficient Titanium Nitride/titanium Oxide Composite Photoanodes for Dye-Sensitized Solar Cells and Water Splitting. *J. Mater. Chem. A* **2015**, *3*, 4695–4705.

(5) Wang, S.; Zhao, L.; Bai, L.; Yan, J.; Jiang, Q.; Lian, J. Enhancing Photocatalytic Activity of Disorder-Engineered C/TiO_2 and TiO_2 Nanoparticles. *J. Mater. Chem. A* **2014**, *2*, 7439–7445.

(6) Costo, R.; Bello, V.; Robic, C.; Port, M.; Marco, J. F.; Puerto Morales, M.; Veintemillas-Verdaguer, S. Ultrasmall Iron Oxide Nanoparticles for Biomedical Applications: Improving the Colloidal and Magnetic Properties. *Langmuir* **2012**, *28*, 178–185.

(7) Fujishima, A.; Rao, T. N.; Tryk, D. A. Titanium Dioxide Photocatalysis. *J. Photochem. Photobiol. C Photochem. Rev.* **2000**, *1*, 1–21.

(8) FUJISHIMA, A.; HONDA, K. Electrochemical Photolysis of Water at a Semiconductor Electrode. *Nature* **1972**, *238*, 37–38.

(9) Aroutiounian, V. M.; Arakelyan, V. M.; Shahnazaryan, G. E. Metal Oxide Photoelectrodes for Hydrogen Generation Using Solar Radiation-Driven Water Splitting. *Sol. Energy* **2005**, *78*, 581–590.

(10) Yang, Y.; Niu, S.; Han, D.; Liu, T.; Wang, G.; Li, Y. Progress in Developing Metal Oxide Nanomaterials for Photoelectrochemical Water Splitting. *Adv. Energy Mater.* **2017**, *7*, 1–26.

(11) Roger, I.; Shipman, M. A.; Symes, M. D. Earth-Abundant Catalysts for Electrochemical and Photoelectrochemical Water Splitting. *Nat. Rev. Chem.* **2017**, *1*.

(12) El Ruby Mohamed, A.; Rohani, S. Modified TiO_2 Nanotube Arrays (TNTAs): Progressive Strategies towards Visible Light Responsive Photoanode, a Review. *Energy Environ. Sci.* **2011**, *4*, 1065.

(13) Ni, M.; Leung, M. K. H.; Leung, D. Y. C.; Sumathy, K. A Review and Recent Developments in Photocatalytic Water-Splitting Using TiO_2 for Hydrogen Production. *Renew. Sustain. Energy Rev.* **2007**, *11*, 401–425.

(14) Mor, G. K.; Varghese, O. K.; Paulose, M.; Shankar, K.; Grimes, C. A. A Review on Highly Ordered, Vertically Oriented TiO2 Nanotube Arrays: Fabrication, Material Properties, and Solar Energy Applications. *Sol. Energy Mater. Sol. Cells* **2006**, *90*, 2011–2075.

(15) Grimes, C. A.; Mor, G. K. *TiO2 Nanotube Arrays*; Springer US: Boston, MA, 2009.

(16) Roy, P.; Berger, S.; Schmuki, P. TiO2 Nanotubes: Synthesis and Applications. *Angew. Chemie - Int. Ed.* **2011**, *50*, 2904–2939.

(17) Rambabu, Y.; Jaiswal, M.; Roy, S. C. Enhanced Photoelectrochemical Performance of Multi-Leg TiO_2 Nanotubes through Efficient Light Harvesting. *J. Phys. D. Appl. Phys.* **2015**, *48*, 295302.

(18) Rambabu, Y.; Jaiswal, M.; Roy, S. C. Effect of Annealing Temperature on the Phase Transition, Structural Stability and Photo-Electrochemical Performance of TiO_2 Multi-Leg Nanotubes. *Catal. Today* **2016**, *278*, 255–261.

(19) Mohammadpour, A.; Farsinezhad, S.; Hsieh, L.-H.; Shankar, K. Multipodal and Multilayer TiO_2 Nanotube Arrays: Hierarchical Structures for Energy Harvesting and Sensing. *MRS Proc.* **2013**, *1552*, 29–34.

(20) Mohammadpour, A.; Waghmare, P. R.; Mitra, S. K.; Shankar, K. Anodic Growth of Large-Diameter Multipodal TiO_2 Nanotubes. *ACS Nano* **2010**, *4*, 7421–7430.

(21) Hebert, K. R.; Albu, S. P.; Paramasivam, I.; Schmuki, P. Morphological Instability Leading to Formation of Porous Anodic Oxide Films. *Nat. Mater.* **2011**, *11*, 162–166.

(22) Allam, N. K.; Alamgir, F.; El-Sayed, M. A. Enhanced Photoassisted Water Electrolysis Using Vertically Oriented Anodically Fabricated Ti-Nb-Zr-O Mixed Oxide Nanotube Arrays. *ACS Nano* **2010**, *4*, 5819–5826.

(23) Yin, W. J.; Tang, H.; Wei, S. H.; Al-Jassim, M. M.; Turner, J.; Yan, Y. Band Structure Engineering of Semiconductors for Enhanced Photoelectrochemical Water Splitting: The Case of TiO_2. *Phys. Rev. B - Condens. Matter Mater. Phys.* **2010**, *82*, 1–6.

(24) Nikolay, T.; Larina, L.; Shevaleevskiy, O.; Ahn, B. T. Electronic Structure Study of Lightly Nb-Doped TiO_2 Electrode for Dye-Sensitized Solar Cells. *Energy Environ. Sci.* **2011**, *4*, 1480.

(25) Hyam, R. S.; Lee, J.; Cho, E.; Khim, J.; Lee, H. Effect of Annealing Environments on Self-Organized TiO_2 Nanotubes for Efficient Photocatalytic Applications. *J. Nanosci. Nanotechnol.* **2012**, *12*, 8908–8912.

(26) Tighineanu, A.; Ruff, T.; Albu, S.; Hahn, R.; Schmuki, P. Conductivity of TiO_2 Nanotubes: Influence of Annealing Time and Temperature. *Chem. Phys. Lett.* **2010**, *494*, 260–263.

(27) Sun, Y.; Yan, K.; Wang, G.; Guo, W.; Ma, T. Effect of Annealing Temperature on the Hydrogen Production of TiO_2 Nanotube Arrays in a Two-Compartment Photoelectrochemical Cell. *J. Phys. Chem. C* **2011**, *115*, 12844–12849.

(28) Amer, A. W.; El-Sayed, M. A.; Allam, N. K. Tuning the Photoactivity of Zirconia Nanotubes-Based Photoanodes via Ultrathin Layers of ZrN: An Effective Approach toward Visible-Light Water Splitting. *J. Phys. Chem. C* **2016**, *120*, 7025–7032.

(29) Shaheen, B. S.; Hafez, A. M.; Murali, B.; Kirmani, A. R.; Amassian, A.; Mohammed, O. F.; Allam, N. K. 10-Fold Enhancement in Light-Driven Water Splitting Using Niobium Oxynitride Microcone Array Films. *Sol. Energy Mater. Sol. Cells* **2016**, *151*, 149–153.

(30) Tauseef Anwar; Wang Li; Naveed Hussain; Wang Chen; Rizwan Ur Rehman Sagar; Liang Tongxiang. Effect of Annealing Atmosphere Induced Crystallite Size Changes on the Electrochemical Properties of TiO_2 Nanotubes Arrays. *J. Electr. Eng.* **2016**, *4*, 43–51.

(31) Chen, X.; Liu, L.; Yu, P. Y.; Mao, S. S. Increasing Solar Absorption for Photocatalysis with Black Hydrogenated Titanium Dioxide Nanocrystals. *Science* **2011**, *331*, 746–750.

(32) Asahi, A. R.; Morikawa, T.; Ohwaki, T.; Aoki, K.; Taga, Y.; Lee, V.; Lee, M. Visible-Light Photocatalysis in Nitrogen-Doped Titanium Oxides Published by : American Association for the Advancement of Science Linked References Are Available on JSTOR for This Article : Visible-Light Visible-Light Photocatalysis Photocatalysis in in N. **2016**, *293*, 269–271.

(33) Chen, X.; Liu, L.; Yu, P. Y.; Mao, S. S. Increasing Solar Absorption for Photocatalysis with Black Hydrogenated Titanium Dioxide Nanocrystals. *Science (80-.).* **2011**, *331*, 746–750.

(34) Naldoni, A.; Allieta, M.; Santangelo, S.; Marelli, M.; Fabbri, F.; Cappelli, S.; Bianchi, C. L.; Psaro, R.; Dal Santo, V. Effect of Nature and Location of Defects on Bandgap Narrowing in Black TiO 2 Nanoparticles. *J. Am. Chem. Soc.* **2012**, *134*, 7600–7603.

(35) Wang, G.; Wang, H.; Ling, Y.; Tang, Y.; Yang, X.; Fitzmorris, R. C.; Wang, C.; Zhang, J. Z.; Li, Y. Hydrogen-Treated TiO_2 Nanowire Arrays for Photoelectrochemical Water Splitting. *Nano Lett.* **2011**, *11*, 3026–3033.

(36) Li, H.; Chen, J.; Xia, Z.; Xing, J. Microwave-Assisted Preparation of Self-Doped TiO_2 Nanotube Arrays for Enhanced Photoelectrochemical Water Splitting. *J. Mater. Chem. A* **2015**, *3*, 699–705.

(37) Tsui, L.; Saito, M.; Homma, T.; Zangari, G. Trap-State Passivation of Titania Nanotubes by Electrochemical Doping for Enhanced Photoelectrochemical Performance. *J. Mater. Chem. A* **2015**, *3*, 360–367.

(38) Sinhamahapatra, A.; Jeon, J.-P.; Kang, J.; Han, B.; Yu, J.-S. Oxygen-Deficient Zirconia (ZrO_{2-x}): A New Material for Solar Light Absorption. *Sci. Rep.* **2016**, *6*, 27218.

(39) Zhi-yong, Z. Electronic Structure and Optical Properties of. *Phys. Lett. A* **2007**, *16*, 2791–2797.

(40) Li, J.; Zhou, H.; Qian, S.; Liu, Z.; Feng, J.; Jin, P.; Liu, X. Plasmonic Gold Nanoparticles Modified Titania Nanotubes for Antibacterial Application. *Appl. Phys. Lett.* **2014**, *104*.

(41) Yang, B.; He, D.; Wang, W.; Zhuo, Z.; Wang, Y. Gold-Plasmon Enhanced Photocatalytic Performance of Anatase Titania Nanotubes under Visible-Light Irradiation. *Mater. Res. Bull.* **2016**, *74*, 278–283.

(42) Tsui, L. -k.; Wu, L.; Swami, N.; Zangari, G. Photoelectrochemical Performance of Electrodeposited Cu_2O on TiO_2 Nanotubes. *ECS Electrochem. Lett.* **2012**, *1*, D15–D19.

(43) Yun, J.-H.; Ng, Y. H.; Huang, S.; Conibeer, G.; Amal, R. Wrapping the Walls of N-TiO_2 Nanotubes with P-$CuInS_2$ Nanoparticles Using Pulsed-Electrodeposition for Improved Heterojunction Photoelectrodes. *Chem. Commun.* **2011**, *47*, 11288.

(44) Zhang, Z.; Zhu, J.; Li, S.; Liu, X.; Mao, Y. Enhanced Photoelectrochemical Properties of TiO2 Nanotube Arrays Sensitized with Energy-Band Tunable $(Cu2Sn)_{x/3}Zn_{1-x}S$ Nanoparticles. *Int. J. Hydrogen Energy* **2014**, *39*, 4198–4205.

Chapter 4

Materials & Methods [*]

4.1 Chemicals and Supplies

4.1.1 TiNbZr MPNTS

TiNbZr alloy sheet (ATI Tiadyne™ 3510) was supplied from ATI Wah Chang. The alloyed was used as received without treatment but cut into samples with dimensions about ~ 20 mm x 10 mm. The breakdown of the alloy constituents is as follows: 55% Ti, 35% Zr, and 5%Nb. Formamide (AppliChem, 99.5%, Analytical grade), Ammonium Flouride (Alfa Aesar, 96%), and Phosphoric acid (Chem-Lab nv, 85%) were to prepare the electrolytic anodization bath. Potassium Hydroxide (AppliChem, Pharma Grade, 85%) was used to prepare 1M KOH solution to be used as the electrolyte in PEC cell.

4.1.2 CZTS nanoparticles

Copperic Chloride dihydrate (Fine-Chem Limited, Analytical grade), Zinc Chloride (Fine-Chem Limited, Analytical grade), Stannous Chloride dihydrate (Lobachemie, 98%, Analytical grade), Thiourea (Lobachemie, 98%, Analytical grade), Polyethylene Glycol 400 (Oxford, Analytical grade) were used in the solvothermal preparation of CZTS nanoparticles. Toluene (LobaChemie, Analytical grade) was used to prepare the electrophoretic deposition solution to be used to deposit CZTS nanoparticles on Hydrogen annealed samples.

4.2 Synthesis and Fabrication

4.2.1 MPNTs Anodization & Annealing

The fabrication of Ti-Nb-Zr-O nanotubes was performed by anodizing titanium alloy ATI Tiadyne™ 3510 (Ti-35Zr-10Nb) with a size of ~ 20 mm x 10 mm. Before anodization, the samples were polished using SiC emery paper up to 2500-grit, and then

[*] Part of this chapter was published in: Omar, M. M.; Fawzy, S. M.; El-Shabasy, A. B.; Allam, N. K.; Large-Diameter Light-Scattering Complex Multipodal Nano-tubes with Graded Refractive Index: Insights into their Formation Mechanism and Photoelectrochemical Performance. *J. Mater. Chem. A*. **2017**, *5*, 23600 - 23611

ultrasonically cleaned successively in Acetone, Ethanol, and deionized (DI) water, each for 10 minutes. Subsequently, anodized samples were rinsed thoroughly with DI water followed by drying under an air stream. Anodic oxide layers were produced by anodization using a 2-electrode electrochemical cell (Figure 4-1), with the alloy serving as the anode / working electrode (WE) and a graphite counter electrode (CE). The separating distance between the electrodes was set to 2 cm, and operating temperature was set to room temperature (24±2°C). Compact oxide barrier films form when the oxide is insoluble in the anodization bath, and porous films when it is moderately soluble.

Anodization was performed by sweeping the potential using Agilent E3612 DC power supply under potentiostatic conditions from 0 V to the target potential (60 V for compact nanotubes and 100 V for Multipodal ones) at a rate of ~ 0.6 V.s-1, and then keeping the potential for the specified time based on the experimental condition. As-prepared samples were annealed in Thermoscientific programmable tube furnace model Lindburg/Blue M Tf55030C for 4 hours under flow of air with a heating rate of 2^0 C/min when compared to Compact nanotubes, but on comparing the effect of the three different annealing atmospheres, heating and cooling rates of 1^0 C/min were used. The samples annealed in Oxygen and Hydrogen were annealed under Oxygen and Hydrogen respectively using a flow rate of 100 SCCM.

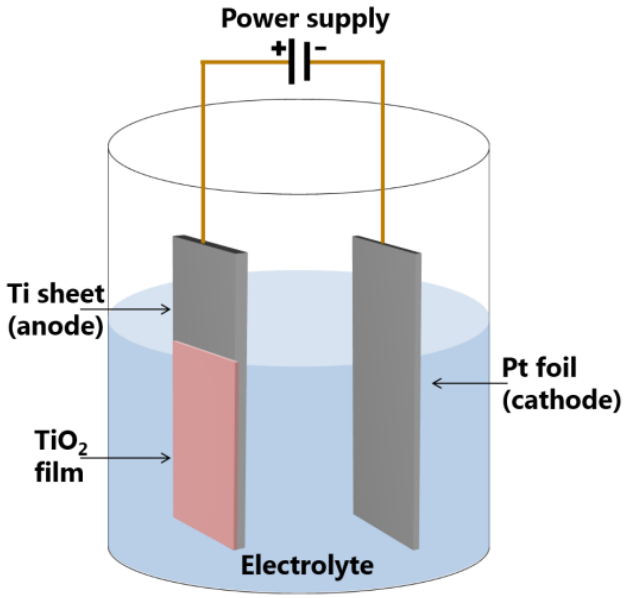

Figure 4-1 Anodization setup [1]

4.2.2 Solvothermal Synthesis & Electrophoretic Deposition

CZTS nanoparticles were synthesized in a three-neck flask, by a solvothermal method using a solvent of high boiling point (PEG 400) and non-stoichiometric molar concentrations of the precursors at 350^{o} C for four hours under Nitrogen bubbling. Next, the obtained precipitate was thoroughly washed several times using Acetone, Ethanol, and distilled water to get rid of the organic residuals. For electrophoretic deposition (Figure 4-2) on Hydrogen annealed samples, 5 mg of the obtained CZTS powder were sonicated for 10 minutes in 25 ml Toluene and two of the MPNTS samples were connected to the positive and negative terminals of the Agilent E3612 DC power supply; where 50V was used for 90 minutes to deposit the CZTS nanoparticles.

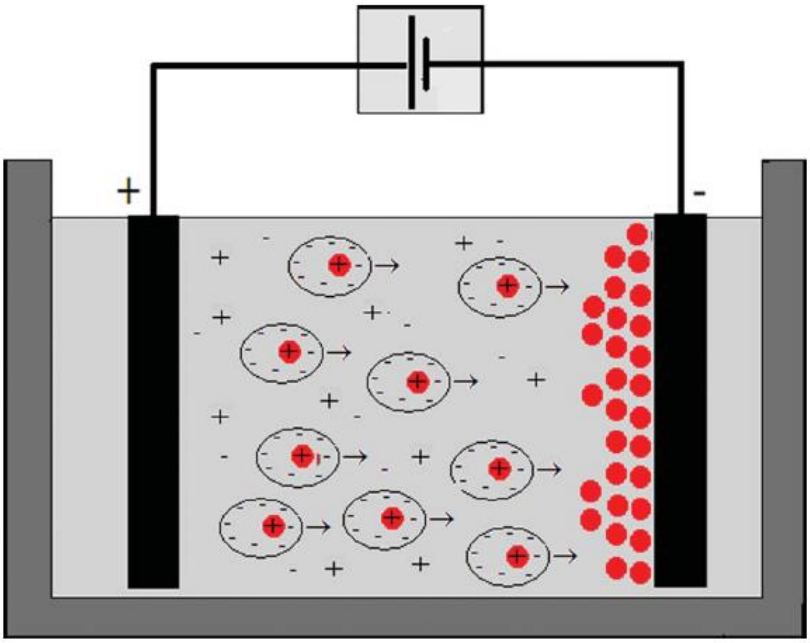

Figure 4-2 Electrophoretic deposition schematic, where the surface charge of the particles suspended controls the deposition direction [2]

4.3 Characterization

4.3.1 Morphology & Structure

A Zeiss SEM Ultra 60 field emission scanning electron microscope (FESEM) was used to characterize the morphology of the fabricated MPNTs. Investigations of the crystalline phases of the annealed samples were performed using a Raman microscope (Pro Raman-L Analyzer) with an excitation laser beam wavelength of 532 nm, as well as PANalytical X'pert Pro PW3040 MPD

X-Ray Diffractometer (XRD) using copper Cu Kα radiation (λ= 0.15406 nm) in the range of 5° to 80° at a scan rate (2θ) of 3° s^{-1}. XPS studies were carried out in a Kratos Axis Ultra DLD spectrometer equipped with a monochromatic Al Kα X-ray source (hν = 1486.6 eV). Binding energies were referenced to the C 1s binding energy of adventitious carbon contamination (CC/C-H), which was taken to be 284.8 eV. CASAXPS software was used for the fitting and deconvolution of the XPS data. Vesta software was used to draw and identify the interstitial sites in the anatase microstructure.

4.3.2 Optical & Photoelectrochemical

A 3-electrode electrochemical cell was used to study the photoelectrochemical performance of the prepared MP and compact NTs with Ag/AgCl as a reference electrode and Platinum as a counter electrode. The measurements were carried out using Biologic SP-200 Potentiostat using a Xenon lamp with AM 1.5 filter illumination in 1M KOH as the electrolyte. Chronoamperometric measurements were done at 0.5 V. Mott-Schottky measurements were done at 1 kHz in the voltage range -1.0 to 1.0 V. Spectroscopic Ellipsometry measurements were done using HORIBA Jobin Yvon Ellipsometer.

References

(1) Bessegato, G.; Guaraldo, T.; Zanoni, M. *Enhancement of Photoelectrocatalysis Efficiency by Using Nanostructured Electrodes*; Aliofkhazraei, M., Ed.; 2014.

(2) Ammam, M. Electrophoretic Deposition under Modulated Electric Fields: A Review. *RSC Adv.* **2012**, *2*, 7633.

Chapter 5

Multipodal Ti-Nb-Zr: Formation Mechanism, Optical and Photoelectrochemical Properties [*]

The purpose of this chapter is to present a theoretical perspective that considers NTs as a bottom-fixed cantilever in order to understand the formation mechanism of MPNTs. The effect of the multipodal morphology on the optical and photoelectrochemical properties is studied through a comparison between multipodal and regular compact nanotubes.

5.1 Morphological Analysis

Figure 5-1 a and b show FESEM images of a tilted surface and a top-view surface, respectively of a 2-hr anodized sample in a formamide-based electrolyte at 100 V. MPNTs can clearly be recognized all over the sample surface (indicated by the yellow arrows). The high magnification images of a bipodal as well as tripodal NTs in the insets of the figure confirm the presence of a common top pore with 2 and 3 pods (legs) underneath. Further validation was proved via the cross-sectional view image shown in Figure 5-1 c, indicating independent, discrete NTs fusing at the middle portion leading to a common pore near the top surface of the oxide layer, an insight which would help in the explanation of the formation mechanism discussed later. The samples synthesized under these anodization conditions are characterized by widely separated NTs with large inter-tubular spaces compared to the regular compact NTs synthesized at 60 V in the same electrolyte (Figure 5-1 d). These wide separations arose from the dissolution of a fluorine-rich layer that exists between pores before transforming into separate tubes. While the presence of fluorine-rich layer underneath the NTs at the metal/oxide interface was confirmed via EDX and XPS analyses[1,2], AES analysis provided a direct proof that the fluoride concentration increases toward the NT/NT junctions reaching its maximum in between the walls of the NTs[3]. As a result, once the oxide is formed at the metal/metal oxide interface, fluoride ions attack both the metal and the oxide to form water soluble fluoride complexes. Subsequently, the inter-connecting layers between the tubes are consumed. In

[*] Parts of this chapter was published in: Omar, M. M.; Fawzy, S. M.; El-Shabasy, A. B.; Allam, N. K.; Large-Diameter Light-Scattering Complex Multipodal Nano-tubes with Graded Refractive Index: Insights into their Formation Mechanism and Photoelectrochemical Performance. *J. Mater. Chem. A*. **2017**, *5*, 23600 - 23611

addition, the high electric field accelerates the dissolution during anodization[4]. Therefore, it is rational to assume that the presence of this layer and its dissolution is the main cause for the large tube separations observed[3]. In this context, it is noteworthy that using a low water content in an organic-based electrolyte resulted in the formation of smooth NT sidewalls with no ripples or inhomogeneities observed at the upper portion (Figure 5-1 c)[5].

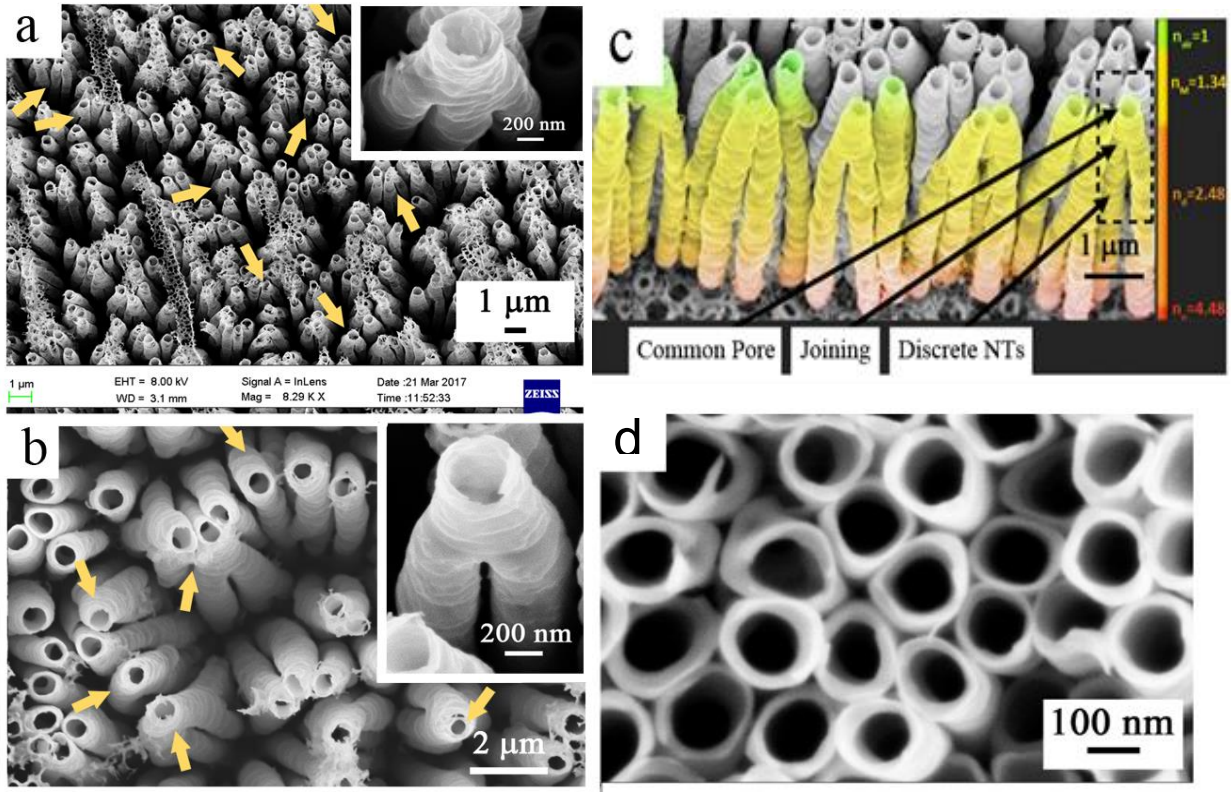

Figure 5-1 (a) FESEM images of the as-prepared Ti-Nb-Zr-O MPNTs tilted surface where the inset shows a high magnification image of a tripodal NTs, (b) normal top-view image, arrows point to the different pods for the same mouth and the inset shows a high magnification image of a bipodal NTs, (c) cross-sectional view of as-prepared MPNTs, where different formation stages are pointed out by the arrows, (d) compact nanotubes

Several prerequisites concerning the magnitude of the forces acting on the NTs as well as their geometry are mandatory for the MPNTs to be formed. These conditions can be estimated by modeling the NT as a vertical cantilever fixed from its bottom end, Figure 5-2. This cantilever is loaded at its top with a perpendicular force (F_{net}) generated by the surface tension of the electrolyte. Forces were assumed to act from the outside only as it was reported that wetting is not uniform over the entire top surface of the NTs, but favourably takes place in the intertubular spaces[6]. Moreover, while the forces exerted due to surface tension can either be a repulsive or attractive forces between the

NTs depending on the contact angle of the meniscus between NTs[7], these forces must overcome the stiffness of the NT to start leaning and reposing on its neighbour. In order to keep the NT bent, stresses generated from the applied force should either exceeds the yield strength of the NT material (i.e. material starts plastic deformation), or elastically bend till reaching a distance by which van der Waals attraction force can keep them in contact[8].

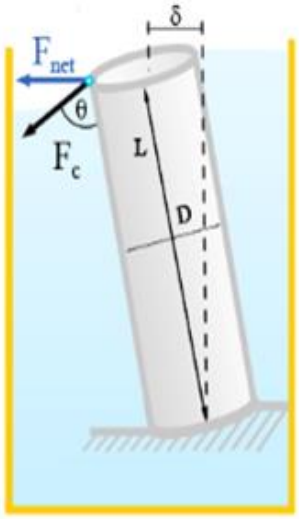

Figure 5-2 A schematic illustration of the force resolution on a bent NT fixed from the bottom.

Figure 5-2 shows a schematic illustration of the bending force generated as a result of the electrolyte capillary force (F_c). Note that for simplification, we neglected the effect of electrostatic repulsion forces from like-charges buildup on the NTs.

$$F_{net} = F_c \sin\theta = 2\pi R\gamma \sin\theta \qquad 5\text{-}1$$

where γ is the surface tension of the electrolyte, R is the outer radius of the NT, and θ is the static equilibrium contact angle of the electrolyte with the NT surface. Two different conditions can occur causing the NTs to lean on each other: First, applied force causes bending plastically, at this case stresses (σ) induced by F_{net} must exceed the yield strength (σ_y) value of the oxide. Bending stresses can be calculated using the following formula[9]:

$$\sigma = \frac{My}{I} = \frac{(F_{net}.L)R}{I} \geq \sigma_y \qquad 5\text{-}2$$

where M is the bending moment due to the F_{net}, y is the distance from the neutral axis of the cross-section with a maximum value equals R, and I is the 2nd moment of area of

the cross-section, for a hollow circle: $I = \frac{\pi(R^4 - r^4)}{4}$, where r is the inner radius. Accordingly, for the NTs to start plastic deformation $F_{net} \geq \frac{\sigma_y I}{LR}$, thus $2\pi R\gamma \sin\theta \geq \frac{\sigma_y I}{LR}$

Therefore, a critical length for the NTs to start plastic deformation (L_p^*) can be calculated as:

$$L_p^* \geq \frac{\sigma_y I}{2\pi R^2 \gamma \sin\theta} \qquad 5\text{-}3$$

Yet, before reaching the plastic deformation region, a second mechanism can be active by which NTs can start bending elastically, and in case the resultant deflection was large enough, NTs can repose on each other. The critical length can then be calculated by making use of the deflection dependence on the applied force:

$$\delta = \frac{F_{net} L^3}{3EI} \qquad 5\text{-}4$$

where δ is the deflection at a distance L from the bottom of the tube, E is the elastic modulus of the oxide, and the value of EI represents the materials stiffness or the resistance of the material to elastic bending. Moreover, for the NTs to repose on each other, each NT must deflect with half the intertubular space, which was estimated, based on the FESEM images, to be approximately R/2.

$$\frac{R}{4} \leq \frac{2\pi R\gamma \sin\theta L^3}{3EI} \qquad 5\text{-}5$$

Then, L^* can be calculated as:

$$L_e^* \geq \left(\frac{3EI}{8\pi\gamma \sin\theta}\right)^{1/3} \qquad 5\text{-}6$$

The value of (EI) represents – but not equal to - the stiffness or elastic resistance of the NT. Thus, the product of E and I value would determine whether the elastic or the plastic bending mode will be active first. From Equations 5-3 & 5-6, L* is directly proportional to the radius of the NTs given that other properties are constant for the oxide and electrolyte ($\sigma_y, E, \gamma,$ and θ). Therefore, to intentionally form MPNTs, tradeoff between R and L must be made. From another perspective, the force required to deflect the NT a certain distance can be calculated as:

$$F_{net} = \frac{3EI}{L^3}\ \delta \qquad 5\text{-}7$$

Therefore, F_{net} is inversely proportional to L or L3 depending on the active mode of bending, while Fc is independent of the length. Therefore, L* represents the value at which the capillary force is large enough to induce the minimum amount of deflection required for NTs to repose on each other given that other parameters are constant. As a result, for NTs shorter than L*, NT stiffness (elastic resistance) would be enough to hold the NT vertically without reaching required deflection. In addition, at first sight, time appears to have no effect on the magnitude of the acting force, yet a more careful analysis leads to a different conclusion. Equation 5-1 shows that the capillary force is dependent on the outer diameter, which increases with time. Hence, as time increases, the acting force on the NTs increases, together with the fact that deflection is a function of not only the acting force but also the length of the NT. Thus, deflection increases as the length increases even if the force remains constant. In the light of this investigation, it can be concluded that anodization time has a dual effect on the deflection, through both the magnitude of force and the NT length. Nevertheless, if the NTs formed are compact, NTs would have no room to bend and lean, this explains the existence of long NTs without being multipodal.

5.2 Optical Analysis

In order to investigate the effect of the multipodal morphology on the optical as well as the photoelectrochemical behavior of the material, diffuse reflectance, linear sweep voltammetry (LSV), chronoamperometry, and Mott- Schottky analyses were performed. Figure 5-3 a shows the diffuse reflectance spectrum, indicating higher scattering from the structure of the MPNTs than that for the compact NTs counterpart (Figure *5-1* d). This is in accordance with the Mie scattering theory suggesting that light is scattered more efficiently when the diameter of the tube matches that of the incident wavelength. This would result in enhanced light harvesting yielding better performance upon their use in optical devices. Note that the diameter of the compact nanotubes in the range of 170 nm, thus acting as subwavelength structures that scatter light in a Rayleigh fashion[10]. It is also expected that the MPNTs provide a graded refractive index behaviour owing to the gradual increase in porosity. The refractive index is gradually matched to that of the surrounding medium (air in this case), thus decreasing the difference between the refractive index of the material and that of air, resulting in

decreased reflectance according to Fresnel's equations[11]. To our knowledge, there are no previous reports for the refractive index of the mixed oxide under study. Therefore, ellipsometry was used to measure the effective refractive index of the compact nanotubes in the wavelength range 300-800 nm then the refractive index was selected at wavelength= 590 nm as convention. Next, information from FESEM images was used in volumetric calculations to obtain the refractive index of the oxide layer underlying the NTs (n_o) following the effective medium theory[12,13].

$$n_C = [f_C * (n_O^q) + f_{air} * (n_{air}^q)]^{1/q} \quad 5\text{-}8$$

$$R = (\frac{n_O - n_{air}}{n_O + n_{air}})^2 \quad 5\text{-}9$$

where R, f_C and f_{air} are the reflectance, and filling factors of the compact layer and air, respectively. The refractive index of the compact tubes (n_c) layer is calculated to be 1.5 with reflectance at incidence normal to the plane = 4%. The refractive index of air (n_{air}) is set to 1 and the exponent is set to 2/3, resulting in n_o=4.48. However, adding the MPNTs portion of the tubes, results in two layers: discrete NTs and MPNTs (Figure *5-1* c) with refractive indices of n_d=2.48 and n_M=1.34 respectively assuming constant length for each portion throughout the sample, and reflectance = 2.11%. This proves that the MPNTs provide graded refractive index behavior decreasing reflectance from the surface. This would open the door for a low-cost morphology optimization technique that can influence the refractive index in favourable ways since the multipodal portion of the nanotube act as a self-induced antireflective coating[14].

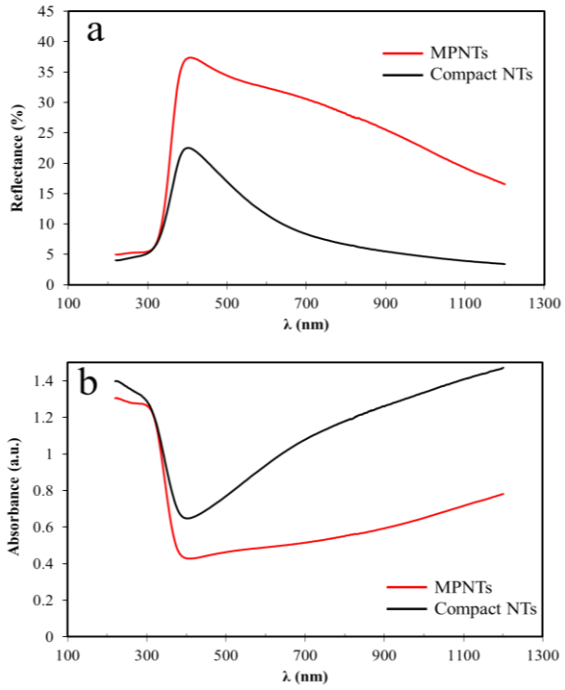

Figure 5-3 (a) Diffuse reflectance and (b)absorbance spectra of MPNTs and compact NTs.

5.3 Photoelectrochemical Analysis

Upon their use as photoanodes to split water photoelectrochemically, the large diameter (~360 nm) MPNTs showed a photocurrent that is almost 9 times larger than that of the comparatively smaller diameter compact NTs under AM 1.5 illumination (100 mW/cm^2) (Figure 5-4 a). The MPNTs showed a photocurrent of 48.4 µA/cm^2 at 1 $V_{Ag/AgCl}$ compared to 5.2 µA/cm^2 for the compact NTs. Figure 5-4 b shows the results of transient photocurrent (J–t) tests carried out under light On/Off conditions at a constant external bias of 0.5 $V_{Ag/AgCl}$. It has been shown that trapped electrons and holes have transient absorption in the visible region[15] as shown in the absorption of the compact nanotubes, Figure 5-3 b. In addition, it is clear that the transient response has decreased in the MPNTs, which is reflected in the I-t curves where the samples exhibited sharp and fast current decay upon turning the light off indicating the presence of a high concentration of shallow oxygen vacancies on the surface[16], as well as being stable over the test duration.

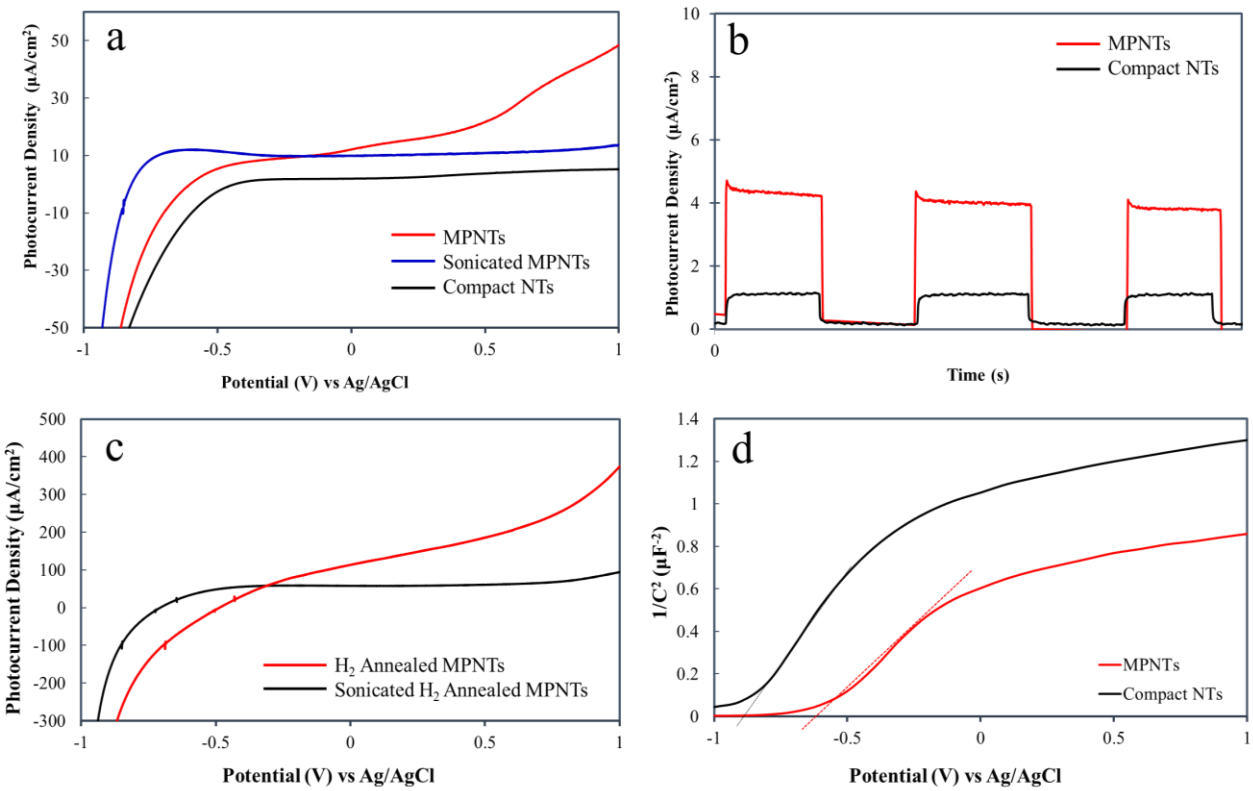

Figure 5-4 Photoelectrochemical performance of MPNTs and compact NTs: (a) LSV, (b) normalized Chronoamperometric measurements conducted at 0.5 V, (c) LSV of H_2 annealed samples, and (d) Mott-Schottky plots.

However, the enhancement cannot be related only to the light absorption capability of the material, Figure 5-3 b as there are two competing factors: the large diameter providing higher scattering, and the graded refractive index reducing surface reflectance. Therefore, Mott-Schottky (MS) analysis was performed to get an insight of the charge carriers density and flat-band potential of the MPNTs. Figure 5-4 d shows the MS plots of the compact and MPNTs, which were used to calculate the charge density and the flat-band potential as:

$$\frac{1}{C^2} = \frac{2}{N_D \varepsilon \varepsilon_0 e}\left[(V - V_{FB}) - \frac{kT}{e}\right] \qquad 5\text{-}10$$

$$N_D = -\left[\frac{2}{\varepsilon \varepsilon_0 e}\right]\left[\frac{d\left(1/C^2\right)}{d(V)}\right]^{-1} \qquad 5\text{-}11$$

where N_D is the donor density, e is the electron charge, ε_0 is the permittivity of free space, ε is the dielectric constant calculated from the measured refracted index where $\varepsilon = n^2 = 20.07$, V is the electrode applied voltage, V_{FB} is the flat-band potential, k is

Boltzmann's constant and T is the temperature set to 25 °C. The positive slopes of the MS plots indicate the n-type semiconducting behaviour of the tested electrodes. The slope was extrapolated to obtain the flat-band potential[17–19]. The V_{FB} of the compact and MPNTs were found to be -1.115 V and -0.835 V, respectively. The positive shift in the V_{FB} of the MPNTs indicates that less voltage is required to overcome the decreased band bending at the interface[17–19]. Moreover, the calculated charge densities are 51.83×10^{18} cm^{-3} and 24.74×10^{18} cm^{-3} for the MPNTs and compact NTs, respectively. The larger N_D may result in increased probability of charge collection, which can explain the observed enhancement in the photocurrent and implying that the multipodal structure may be passivating some of the surface states that act as recombination centers[20].

To confirm the large diameter MPNTs effect, the samples were sonicated to remove the MPNTs portion of the nanotubes. The photoelectrochemical measurements were done before and after the sonication step. Figure 5-4 a shows that the photocurrent has decreased after sonication. To further confirm that this effect is independent of the annealing conditions, a batch of samples were annealed under Hydrogen gas flow instead of Air. The same behavior persisted where the photocurrent has decreased after sonication (Figure 5-4 c). The higher photocurrent can be attributed to the effect of the large diameter of the MPNTs providing a larger surface area in contact with the electrolyte that can facilitate hole transfer to the present species undergoing oxidation[21].

References

(1) Amer, A. W.; Mohamed, S. M.; Hafez, A. M.; AlQaradawi, S. Y.; Aljaber, A. S.; Allam, N. K. Self-Assembled Zirconia Nanotube Arrays: Fabrication Mechanism, Energy Consideration and Optical Activity. *RSC Adv.* **2014**, *4*, 36336–36343.

(2) Albu, S. P.; Ghicov, A.; Aldabergenova, S.; Drechsel, P.; LeClere, D.; Thompson, G. E.; Macak, J. M.; Schmuki, P. Formation of Double-Walled TiO_2 Nanotubes and Robust Anatase Membranes. *Adv. Mater.* **2008**, *20*, 4135–4139.

(3) Berger, S.; Albu, S. P.; Schmidt-Stein, F.; Hildebrand, H.; Schmuki, P.; Hammond, J. S.; Paul, D. F.; Reichlmaier, S. The Origin for Tubular Growth of TiO_2 Nanotubes: A Fluoride Rich Layer between Tube-Walls. *Surf. Sci.* **2011**, *605*, L57–L60.

(4) Chen, Y.-X. X.; Jacob, T. Function Calculation: A Simple Way to Predict the Geometry Parameters of Self-Organized Titania Nanotube Arrays. *ChemElectroChem* **2017**, *4*, 476–480.

(5) Regonini, D.; Satka, A.; Jaroenworaluck, A.; Allsopp, D. W. E.; Bowen, C. R.; Stevens, R. Factors Influencing Surface Morphology of Anodized TiO_2 Nanotubes. *Electrochim. Acta* **2012**, *74*, 244–253.

(6) Roy, P.; Dey, T.; Schmuki, P. Scanning Electron Microscopy Observation of Nanoscopic Wetting of TiO_2 Nanotubes and ODS Modified Nanotubes Using Ionic Liquids. *Electrochem. Solid-State Lett.* **2010**, *13*, E11.

(7) Hill, J. J.; Haller, K.; Gelfand, B.; Ziegler, K. J. Eliminating Capillary Coalescence of Nanowire Arrays with Applied Electric Fields. *ACS Appl. Mater. Interfaces* **2010**, *2*, 1992–1998.

(8) Pokroy, B.; Kang, S. H.; Mahadevan, L.; Aizenberg, J. Self-Organization of a Mesoscale Bristle into Ordered, Hierarchical Helical Assemblies. *Science.* **2009**, *323*, 237–240.

(9) Beer, F. P.; Johnston, E. R.; DeWolf, J. T.; Mazurek, D. *Mechanics of Materials*; 6th ed.; McGraw-Hill, 2012.

(10) Mohammadpour, A.; Farsinezhad, S.; Hsieh, L.-H.; Shankar, K. Multipodal and Multilayer TiO_2 Nanotube Arrays: Hierarchical Structures for Energy Harvesting and

Sensing. *MRS Proc.* **2013**, *1552*, 29–34.

(11) Rambabu, Y.; Jaiswal, M.; Roy, S. C. Enhanced Photoelectrochemical Performance of Multi-Leg TiO_2 Nanotubes through Efficient Light Harvesting. *J. Phys. D. Appl. Phys.* **2015**, *48*, 295302.

(12) Min, W. L.; Jiang, B.; Jiang, P. Bioinspired Self-Cleaning Antireflection Coatings. *Adv. Mater.* **2008**, *20*, 3914–3918.

(13) Stavenga, D. G.; Foletti, S.; Palasantzas, G.; Arikawa, K. Light on the Moth-Eye Corneal Nipple Array of Butterflies. *Proc. Biol. Sci.* **2006**, *273*, 661–667.

(14) Xi, J. Q.; Schubert, M. F.; Kim, J. K.; Schubert, E. F.; Chen, M.; Lin, S.-Y.; Liu, W.; Smart, J. A. Optical Thin-Film Materials with Low Refractive Index for Broadband Elimination of Fresnel Reflection. *Nat. Photonics* **2007**, *1*, 176–179.

(15) Schneider, J.; Matsuoka, M.; Takeuchi, M.; Zhang, J.; Horiuchi, Y.; Anpo, M.; Bahnemann, D. W. Understanding TiO_2 Photocatalysis : Mechanisms and Materials. *Chem. Rev.* **2014**, *114*, 9919–9986.

(16) Ahn, S. E.; Lee, J. S.; Kim, H.; Kim, S.; Kang, B. H.; Kim, K. H.; Kim, G. T. Photoresponse of Sol-Gel-Synthesized ZnO Nanorods. *Appl. Phys. Lett.* **2004**, *84*, 5022–5024.

(17) Cai, H.; Yang, Q.; Hu, Z.; Duan, Z.; You, Q.; Sun, J.; Xu, N.; Wu, J. Enhanced Photoelectrochemical Activity of Vertically Aligned ZnO-Coated TiO_2 Nanotubes. *Appl. Phys. Lett.* **2014**, *104*.

(18) Qi, X.; She, G.; Huang, X.; Zhang, T.; Wang, H.; Mu, L.; Shi, W. High-Performance N-Si/α-Fe_2O_3 Core/shell Nanowire Array Photoanode towards Photoelectrochemical Water Splitting. *Nanoscale* **2014**, *6*, 3182.

(19) Wang, Z.; Yang, C.; Lin, T.; Yin, H.; Chen, P.; Wan, D.; Xu, F.; Huang, F.; Lin, J.; Xie, X.; *et al.* Visible-Light Photocatalytic, Solar Thermal and Photoelectrochemical Properties of Aluminium-Reduced Black Titania. *Energy Environ. Sci.* **2013**, *6*, 3007.

(20) Amer, A. W.; El-Sayed, M. A.; Allam, N. K. Tuning the Photoactivity of Zirconia Nanotubes-Based Photoanodes via Ultrathin Layers of ZrN: An Effective Approach

toward Visible-Light Water Splitting. *J. Phys. Chem. C* **2016**, *120*, 7025–7032.

(21) Mor, G. K.; Varghese, O. K.; Paulose, M.; Shankar, K.; Grimes, C. A. A Review on Highly Ordered, Vertically Oriented TiO_2 Nanotube Arrays: Fabrication, Material Properties, and Solar Energy Applications. *Sol. Energy Mater. Sol. Cells* **2006**, *90*, 2011–2075.

Chapter 6

Towards Enhancing the Optical & Photoelectrochemical Properties of MPNTs*

As seen from the literature review, annealing in different atmospheres can be one way to manipulate the material properties and tune the bandgap. Following the morphology optimization phase, the aim of this phase was study possible routes for enhancement of optical and PEC properties. The effect of the annealing atmosphere on the structure, optical and PEC properties of the MPNTs is studied in sections 6.1-6.4; and CZTS deposition on H100 MPNTs is studied in section 6.5.

6.1 Morphological Analysis

Figure 6-1 shows FESEM images of the as-synthesized MPNTs and after their annealing under oxygen (O100), Air (Air0) and hydrogen (H100) streams. Note the uniform distribution of the MPNTs on the surface. Upon annealing in hydrogen (H100), a noticeable decrease in the nanotubes diameter is observed. Outer diameters of O100, Air0 & H100 are 418.31, 411.33 and 371.45 respectively. Figure 6-2 a,b shows the top, side, and bottom views of the synthesized nanotubes confirming the formation of compact NTs at the bottom (Figure 6-2 b inset) and their bending as they grew longer. MPNTs are created as a result of the bending and fusion of discrete NTs once they exceed a critical length. Moreover, Figure 6-2 c shows a high-resolution cross-sectional FESEM image of a MPNT where two NTs merge, confirming the proposed formation mechanism discussed in the previous chapter.

* Parts of this chapter are submitted as a paper

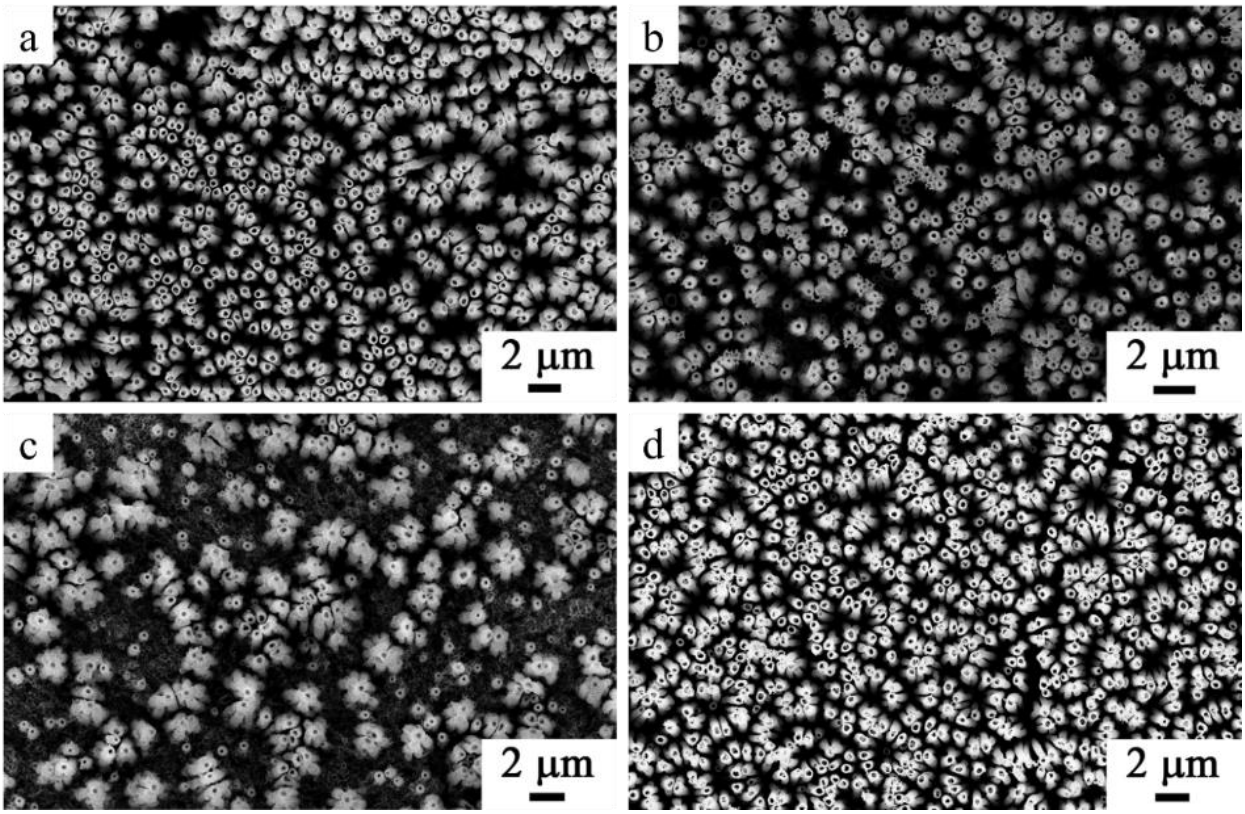

Figure 6-1 FESEM images of the (a) as-prepared Ti-Nb-Zr-O MPNTs via anodization for 2 hours at 100 V in formamide-based electrolyte. (b-d) After annealing in (b) Oxygen, (c) Air0, (d) Hydrogen

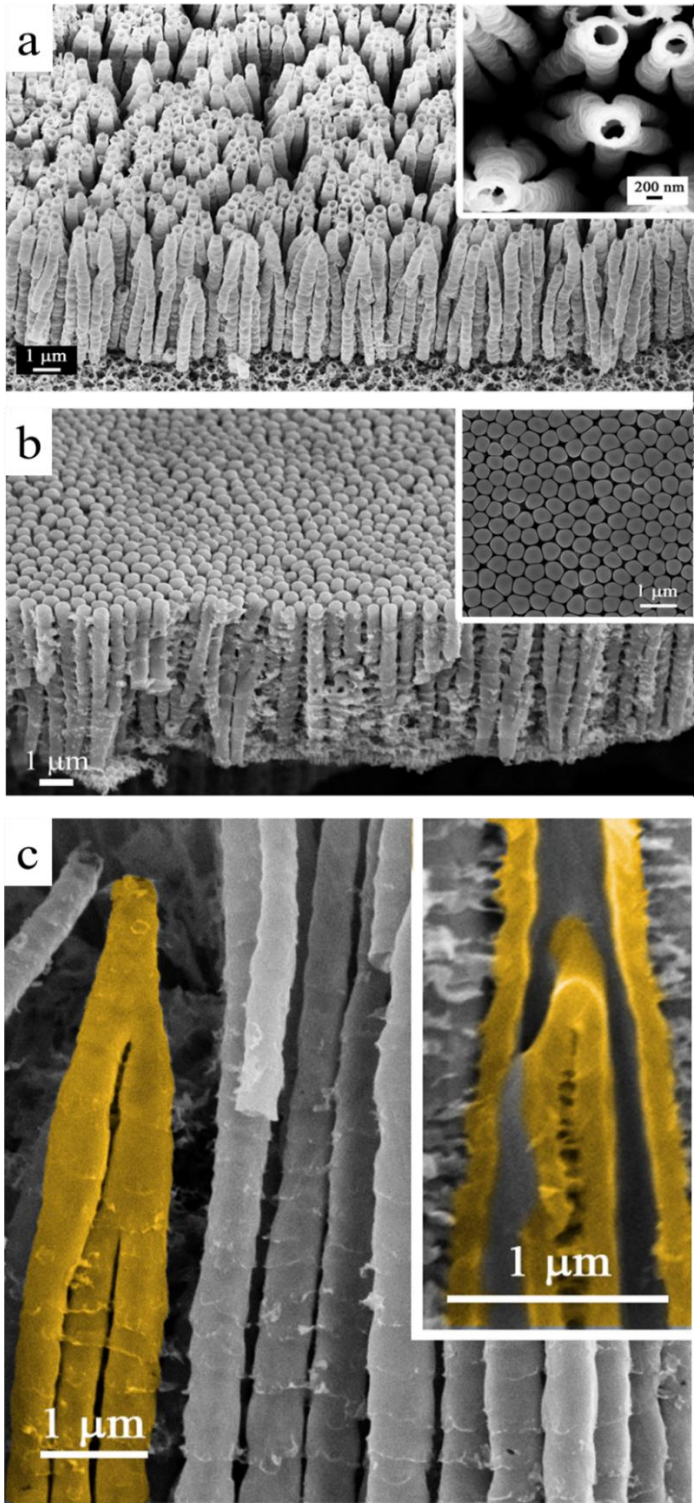

Figure 6-2 FESEM images of MPNTs via anodization for 2 hours at 100 V in formamide-based electrolyte. (a) Tilted surface where the inset shows a high magnification image of the MPNTs, (b) bottom view of the MPNTs confirming the presence of a compact NTs at the bottom (c) closeup image of a tripodal nanotube, the inset shows cross-sectional view

6.2 Structural Analysis

Figure 6-3 shows the diffraction patterns obtained for the samples annealed under different conditions. The Air0 and O100 peaks can be indexed to the characteristic diffraction peaks of the anatase phase of TiO_2, indicating a polycrystalline structure. The sharp and strong peak at (100) indicates that the presence of highly crystalline anatase. It should be noted that no significant peaks for neither ZrO_2 nor Nb_2O_5 phases are observed. The absence of peaks relevant to other oxides indicates the coherent integration of Zr and Nb into the lattice of the TiO_2. Hence, the XRD suggests the formation of an anatase-dominant structure of mixed complex oxide Ti-Nb-Zr-O rather than different binary oxides[1].

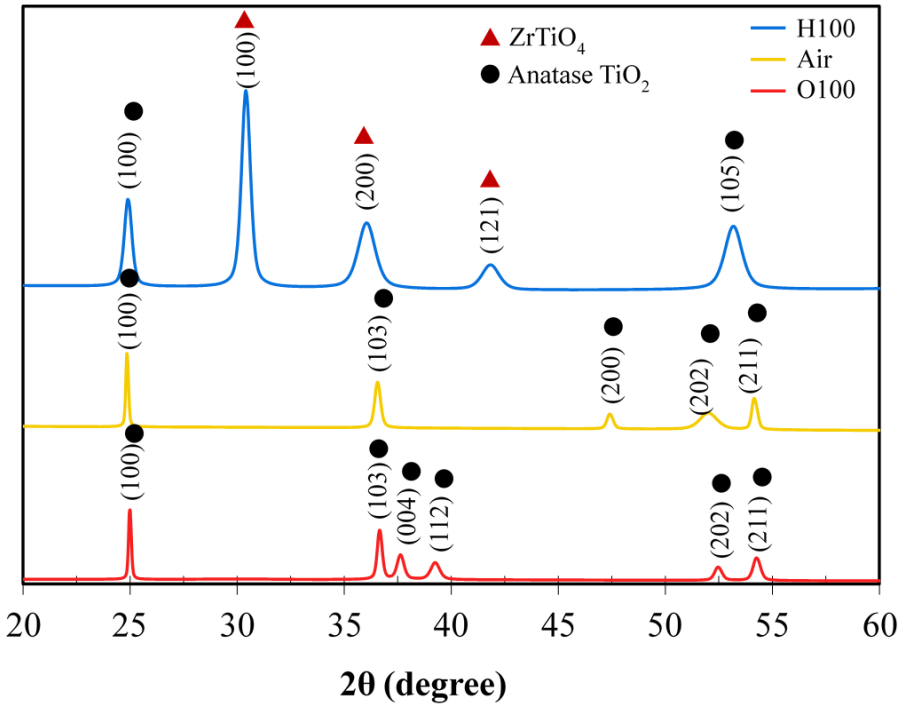

Figure 6-3 XRD of H100, Air0 & Oxygen showing incorporation of Zr & Nb in an anatase crystal structure in O100 & Air0, with formation $ZrTiO_4$ phase in H100

However, the obtained peaks appear at a 2θ ca. 0.4° lower than the reference anatase peaks, which can be attributed to the change in the lattice constant and the heterogenous tensile strain in the structure owing to the incorporation of secondary metals[2–7]. Quantitative analysis was performed for the XRD data in order to calculate the interplanar distances (d-spacing), crystallite size (D), the full width at half maximum (FWHM) of the different peaks, and the resultant lattice strain at each condition, Table

6-1. The crystallite size can provide a direct measure for the coherence of different crystalline domains, and can be calculated using Scherrer's Equation (6-1)[8]:

$$D = \frac{0.94\lambda}{\beta cos\theta} \qquad 6\text{-}1$$

where λ is the incident x-ray wavelength, β is the FWHM, θ is half of the Bragg's angle, 0.94 is a shape factor. While the lattice strain (ε) can be estimated from the Williamson-Hall equation (assuming a uniform deformation model in [9]:

$$\varepsilon = \frac{\beta_\varepsilon}{4\tan\theta} \qquad 6\text{-}2$$

Table 6-1 Detailed calculation of shift, d-spacing, crystallite size, FWHM, and resultant strain

H100								
No.	Index	Pos. [2θ]	Ref. (2θ)	Shift	d-spacing [Å]	β [°2Th.]	Crystallite Size only [Å]	Strain
1	100	24.8824	25.224	-0.3416	3.57846	0.3936	236.1264	0.44602
2	100 (ZrTiO4)	30.3837	30.442	-0.0583	2.94193	0.4723	198.2648	0.43483
3	200 (ZrTiO4)	36.0155	35.641	0.3745	2.49376	0.9446	99.90288	0.72646
4	121 (ZrTiO4)	41.7961	41.9	-0.1039	2.16127	0.9446	101.6994	0.61848
5	105	53.1278	53.867	-0.7392	1.72394	0.9446	106.2288	0.47232
Air0								
No.	Index	Pos. [2θ]	Ref. (2θ)	Shift	d-spacing [Å]	β [°2Th.]	Crystallite Size only [Å]	Strain
1	100	24.84	25.224	-0.3851	3.58464	0.1181	924.4797	0.13407
2	103	36.53	36.903	-0.3734	2.45985	0.2952	327.0922	0.22361
3	200	47.37	47.848	-0.4737	1.91898	0.2952	339.2672	0.16822
4	202	51.96	51.96	0.0029	1.75981	0.9446	105.696	0.48458
5	211	54.12	54.848	-0.7262	1.6946	0.2362	442.608	0.11559
O100								
No.	Index	Pos. [2θ]	Ref. (2θ)	Shift	d-spacing [Å]	β [°2Th.]	Crystallite Size only [Å]	Strain
1	100	24.9697	25.224	-0.2543	3.56616	0.1181	924.6465	0.13335
2	103	36.6271	36.903	-0.2759	2.45352	0.2362	414.6774	0.17841
3	4	37.5976	37.814	-0.2164	2.39239	0.3542	271.4241	0.26013
4	112	39.2144	38.459	0.7554	2.2974	0.4723	203.1017	0.33146
5	202	52.4229	51.96	0.4629	1.74544	0.3542	286.5126	0.17987
6	211	54.2202	54.848	-0.6278	1.69176	0.3542	288.8119	0.17297

Moreover, the lattice parameters a and c are estimated from the lattice geometry and the d-spacing of the planes as shown in equation 6-3

$$\frac{1}{{d_{hkl}}^2} = \frac{h^2+k^2}{a^2} + \frac{l^2}{c^2} \qquad 6\text{-}3$$

The calculations for both Air0 and O100 samples resulted in a lattice parameter of a= b= 3.58 and 3.56 Å, c= 10.15 and 10.14 Å, respectively. It should be noted that these values differ from that of the standard anatase (JCPDS No. 01-075-2545, a=3.799 Å and c=9.509 Å). This shift corresponds to the effect of incorporation of larger diameter six-fold coordinated Nb^{5+} (0.064 nm) and Zr^{4+} (0.072 nm), compared to that of the host Ti^{4+} (0.061 nm)[1,10]. In addition, a dissimilar strain is noticed between the 2 axes of the lattice a and c, which suggests the presence of an induced anisotropic tensile stress in the lattice.

On the other hand, annealing in a reducing atmosphere (H100) leads to the formation of different phases. As shown in Figure 6-3, new diffraction peaks can be observed for H100 samples which cannot be indexed solely against anatase, but also orthorhombic $ZrTiO_4$ (JCPDS: 00-034-0415). Significant peak broadening can be observed relative to Air0 and O100, this increase in the FWHM can be ascribed to the particle size as well as the strain effects as mentioned earlier as the crystallite size in H100 was equal 236.12 Å, almost ¼ that of the Air0 or O100[11]. In addition, the increased FWHM for the (100) anatase combined with the decrease in its intensity indicates decreased crystallinity resulting from the structural disorder after the interaction of the H_2 atoms with the oxide. However, a strong peak at 30.5°, which is attributed to the $ZrTiO_4$, would suggest that annealing in a reducing atmosphere would favour the Zr ions to form an orthorhombic $ZrTiO_4$ crystal rather than being incorporated in the tetragonal anatase. Hence, retarding the anatase phase[12].

Raman spectra were collected to further characterize the structure since Raman spectroscopy is much more sensitive to short-range distortions as the Raman modes are determined by the symmetry and bonding of the molecular species[13]. Figure 6-4 a shows the different peaks obtained for the alloy over the range 100-1000 cm^{-1}. For the Air0 and O100, peaks observed at 628, 508, 362, a weak shoulder at 202, and a major peak at 132 cm^{-1} are consistent with the E_g, B_{1g}, A_{1g}/B_{1g}, and E_g vibrational modes of the tetragonal crystal structure of the anatase, respectively. Moreover, a weak broad band can be observed from 700-900 cm^{-1} centred near 800 cm^{-1} can be assigned to the B_{1g} mode (397 cm^{-1}) first overtone[14]. No peaks were observed for rutile, Nb_2O_5, or ZrO_2; which supports what have been previously discussed that the formed oxide is a single mixed oxide. It is worth noting that there are no significant variations seen between the

peaks of the Air0 and O_2 annealed samples. However, significant shift as well as slight broadening in the characteristic E_g peak (132 cm^{-1}) can clearly be seen compared to the nominal anatase, Figure 6-4 b. The broadening or shift of E_g mode in TiO_2 has been previously attributed in literature to defects, nonstoichiometry, non-homogeneity of size distribution, strain, and phonon confinement[15–21].

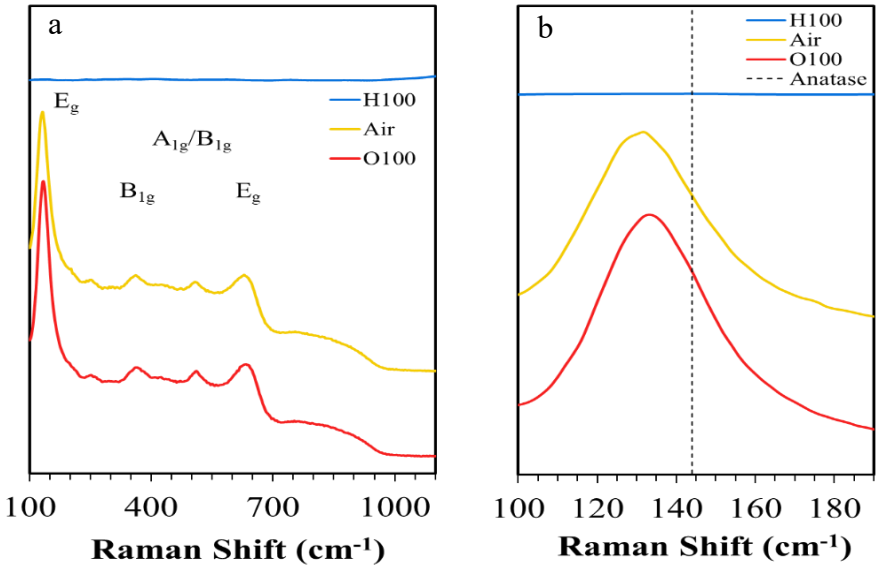

Figure 6-4 Raman Spectra of the samples (b) Raman Band at 134 cm^{-1} magnified and the vertical dashed line represents the nominal position of the Eg peak of Anatase.

The dependence of the phonon position on particle size is expressed in equation 6-4 [22]:

$$\Delta x \Delta p \geq \frac{h^2}{4} \qquad 6\text{-}4$$

where Δx is the particle size, Δp is the phonon momentum distribution and h is the reduced Planck's constant. Increased phonon confinement occurs as the particle size being smaller, this leads to increased phonon momentum distribution, i.e. broadened peak for the scattered phonon momentum, and shift in the Raman band wave number. Hence, an observable red shift occurred in the E_g and B_{1g} mode. On the other hand, no remarkable shift in the A_{1g} and the other E_g mode. This dissimilar shift in the Raman frequencies (wave numbers) can be attributed to the anisotropic tensile stress in the lattice discussed earlier, besides the increased bond length resulting from Nb and Zr doping. The entry of Nb and Zr in the lattice -whether in interstitial or substitutional sites - would affect the lattice symmetry resulting in a distorted TiO_6^{8-} octahedron as a

result of the ionic radius mismatch leading to a change in the phonon vibrations. The bond length can be calculated from the bond length/Raman frequency/covalency relationship assuming distinct Ti-O bond with no vibrational interaction between the neighbouring Ti-O bonds in the lattice [23]:

$$\nu_{Ti-O} = 722e^{-1.54946(R-1.809)} \qquad 6\text{-}5$$

where R is the Ti – O bond length (Å) and υ represents the Raman shift (cm^{-1}). These calculations resulted in bond lengths for Ti-O bond of 2×1.89, 3×2.03, and 2.25 Å based on the 628, 508, 362 cm^{-1} Raman bands, which is longer than the standard anatase bond lengths (apical Ti-O bond length: 2×1.9797, equatorial Ti-O bond length: 4×1.9338). While the calculated Ti-Ti bond length based on the sharp peak at 132 cm^{-1} resulted in 2.91 Å, compared to 2.876 Å for the pure anatase[24]. These results are consistent with the assumptions of the distorted octahedral and strained lattice discussed earlier in the XRD analysis. This confirmed distortion, along with the fact that no separate phases are present, indicates that the Nb and Zr entered the lattice in either an interstitial or a substitutional site. Previous geometrical calculations based on the hard sphere model showed that the max. radius for an ion to fit in between the native ions in the larger interstitial site (I2) equals to 0.57 Å for a stable geometrical configuration, i.e. smaller than the radius of both the Nb and Zr [25]. This said, it is clear that neither the Nb nor the Zr can fit in the interstitial site to form an interstitial solid solution. On the other hand, for a substitutional solid solution to form, Hume-Rothery rules must be satisfied, which is the case between the Nb, Zr, and the Ti ions.

Raman spectra of the H100 the anatase peaks diminished and no other peaks were observed. This can result from either the formation of new Raman-inactive species or the presence of a significantly low crystalline domains. However, after trying different positions and exposing the samples to the Raman laser beam for prolonged time, significant increase in the 136 cm^{-1} peak was observed as well as the growth of new peaks, Figure 6-5. These observations along with the XRD pattern confirms the presence of partially-amorphous as well as crystalline domains with good crystal quality in the H100. Moreover, these features suggest that significant structural changes have occurred after annealing in hydrogen, resulting in increased structural disorder at the surface. This structural disorder can be the reason for the appearance of new signals

after annealing, indicating that the original symmetry of the anatase crystal structure was destroyed [26,27]. Therefore, owing to the phonon confinement effects and the breaking down of the Raman selection rule, new Raman-forbidden modes can be activated and are held responsible for the new Raman signals [28,29].

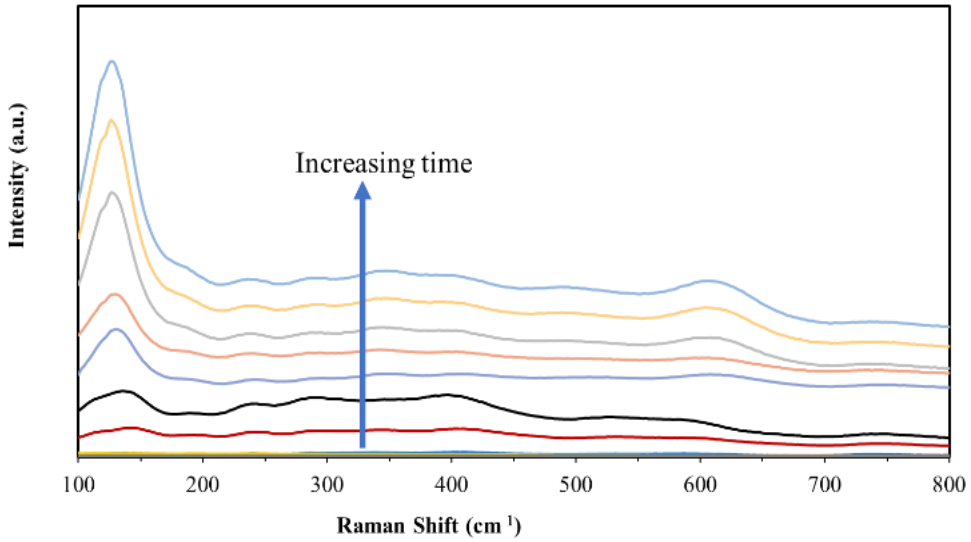

Figure 6-5 Raman spectra of H100 at different times

XPS analysis was carried out to investigate the present surface species, i.e. Ti^{4+}, O^{2-}, OH^{-}, Ti^{3+}, and oxygen vacancies (V_o). For the Air0 and O100, Ti 2p spectra exhibited two significant broad peaks at 458.17 ± 0.07 (Ti $2p_{3/2}$) and 463.9 ± 0.08 eV (Ti $2p_{1/2}$) with a spin-orbit splitting of 5.75 eV (Figure 6-6 a,b) confirming that the 2 peaks represents fully oxidized Ti ion in a sole chemical state Ti^{4+}. Careful investigation for the shape of the peak eliminates the possibility of the presence of neither Ti^{2+}, which should be separated by ~ 3-4 eV from the Ti^{4+} maxima, nor Ti^{3+} [30,31]. While Figure 6-6 d-f shows the Nb 3d photoemission spectra, broad doublets and symmetric peaks at 206.73 ± 0.05 and 209.58 ± 0.05 eV can be observed, characteristic of Nb^{5+} [32,33]. In addition, a peak for the Zr at ~ 184.35 ± 0.1 eV with a spin-orbit splitting of 2.4 eV in Figure 6-6 g-i suggests the existence of zirconium in the form of Zr^{4+} [1,33,34]. No significant relative changes in the binding energies or the FWHM between both Air0 and O100, confirming that both conditions lead to the same oxidation states[30].

O1s spectra showed a wide asymmetric peak with a tail towards higher binding energies in the Air0 samples, while for the O100, a multiple splitting exists, Figure 6-6

j-k. The presence of the asymmetric peak in the Air0 samples suggests the existence of different chemical states for the O1s.[35] Hence, peaks were carefully deconvoluted and fitted to 3 main components corresponding to 3 different chemical states located at 529.55 ± 0.03, 530.5 ± 0.3 and 532.1 ± 0.5 eV. Generally speaking, the binding energies present near 530 eV are assigned to the oxide ions of the lattice, and those of higher binding energies are assigned to the non-lattice/adsorbed oxygens[30,36,37]. The photoemission spectra at 529.55 eV was assigned to the intrinsic oxygen (Ti-O bond) in the anatase TiO_2 crystal lattice. Next, the peaks at 530.5 and 532.1 eV were attributed to loosely bound oxygen on the surface in the form of OH and H_2O[38]. The deconvoluted single peak at 529.55 eV confirms the presence of the lattice oxygen in a single oxidation state, supporting the claim that a single mixed oxide is formed rather than multiple oxides[39,40]. On the other hand, the observed splitting in the O100 is ascribed to the increased peak of the adsorbed oxygen on the surface due to the presence of an oxygen rich atmosphere during annealing which facilitates its adsorption to the surface.

Table 6-2 summarizes the peak positions, as well as the shifts compared to pure anatase for the 3 conditions. Although the presented data is in a good agreement with the literature, the binding energies of pure oxides of Ti, Nb, and Zr, all peaks showed a remarkable shift towards lower binding energies. This shift in positions indicates the influence of the Zr and Nb addition on the oxidation states of O and Ti. O1s peak showed a shift of ~ 0.4 eV towards lower BE compared to pure anatase (530.87 eV).[41] This shift originates from the influence of the new neighbouring atoms surrounding the oxygen in the lattice. The shift in the binding energies in the studied alloy is attributed to: (1) the difference in electronegativities between the dopant and the host atoms (χ_{Ti}=1.5, χ_{Nb}=1.6, χ_{Zr}=1.3). The binding energy is directly proportional to the neighbouring atoms' electronegativity. Hence, the addition of Zr (less electronegative atom) with higher percentage compared to Niobium in a substitutional site tends to lower the binding energies of Ti^{4+} and O^{2-}, owing to the increased electron cloud density around the Ti as well as the increased electron shielding effect[42]. (2) the presence of oxygen vacancies around the Ti^{4+}, Nb^{5+}, and Zr^{4+} ions[43]. These shifts correspond to the shifts in the Raman frequencies as well as in the diffraction angles of the anatase discussed before, confirming that the Nb and Zr as incorporated in the anatase lattice in a substitutional mode [12,44,45].

Meanwhile, annealing in a reducing atmosphere resulted in a different behaviour and subsequent change in the stoichiometry. The reduction of Titania leads to a defective structure either by formation of oxygen vacancies TiO_{2-x} or Ti interstitials $Ti_{1+x}O_2$, and in both cases O is deficient with respect to Ti, and is accompanied by the presence of Ti^{3+} species[46,47]. Nevertheless, in our case the presence of Ti interstitials were ruled out as it probably forms under more harsh conditions like high-temperature vacuum annealing [46–49], besides, annealing in an oxygen-deficient environment would energetically favour the oxygen vacancies formation rather than Ti interstitials [50,51]. XPS spectra in Figure 6-6 c reveals a shoulder in the Ti $2p_{½}$ at binding energy 456.7 eV, in addition to Ti $2p_{3/2}$ at 463.12 eV, which can be ascribed to Ti^{3+} [52–54]. It is fairly well known in literature that annealing in reducing atmosphere results in the formation of point defects in the anatase crystal lattice. As the hot H_2 molecules interacts with the surface of the TiO_2, it favours the disruption of the Ti-O bonds as it overcomes the activation energy of the lattice rearrangement, creating oxygen vacancies [52].

Table 6-2 XPS peak positions and shifts relative to the Anatase peaks

			O100		Air0		H100	
Element	Orbital	Reference BE (eV)	BE (eV)	Shift (eV)	BE (eV)	Shift (eV)	BE (eV)	Shift (eV)
Ti	2p 3/2	458.76	458.24	0.52	458.1	0.66	458.3	0.46
	2p 1/2	464.46	463.98	0.48	463.82	0.64	464.09	0.37
	split	5.7	5.74	-0.04	5.72	-0.02	5.79	-0.09
Nb	3d 5/2	207.4	206.78	0.62	206.68	0.72	206.7	0.7
	3d 3/2	210.1	209.53	0.57	209.43	0.67	209.45	0.65
	split	2.7	2.75	-0.05	2.75	-0.05	2.75	-0.05
Zr	3d 5/2	182.8	182.09	0.71	181.83	0.97	181.83	0.94
	3d 3/2	185.2	184.48	0.72	184.23	0.97	184.23	0.94
	split	2.4	2.39	0.01	2.4	0	2.4	0
O (TiO2)	Lattice	530	529.57	0.43	529.52	0.48	529.63	0.37
	Non-lattice		530.8		530.34		530.96	
			532.53		531.6			

The O1s spectrum of the H100 exhibited a tail towards higher binding energies. However, it cannot be attributed to the adsorbed OH as in the O100 samples since hydrogen is a reducing atmosphere which would prohibit the bridging of OH on the surface due to the oxygen-poor environment. Thus, the O1s asymmetric peak was fitted into 2 peaks centred at 529.63 and 530.96 eV. Those 2 peaks match well with the peak

splitting observed in the O1s in $ZrTiO_4$. Moreover, this is confirmed by the small shift in the Zr 3d peak as previously reported[55,56]. It was reported that the peak at 529.63 eV relates to the oxide ion of the Ti-O-Zr coordination, while the one at 530.96 eV belongs to the less negatively charged oxide ions Ti-O-Ti[56]. Also, the peak at 530.96 eV will closely match both the O1s in anatase and $ZrTiO_4$. This difference in binding energies originates from the difference in coordination of different oxide ions (Zr-O-Ti, and Ti-O-Ti)[56], besides shifting to lower binding energies resulting from the phase transformation during annealing[52]. These results are analogues to that of the XRD confirming the presence of $ZrTiO_4$ after hydrogen annealing.

This said, the picture that emerges is that the oxygen and Air0 annealing led to the formation of a single mixed oxide as the Nb and Zr ions substituted that of the Ti in the anatase lattice, while annealing in a reduced atmosphere led to the formation of 2 oxides, $ZrTiO_4$ and anatase.

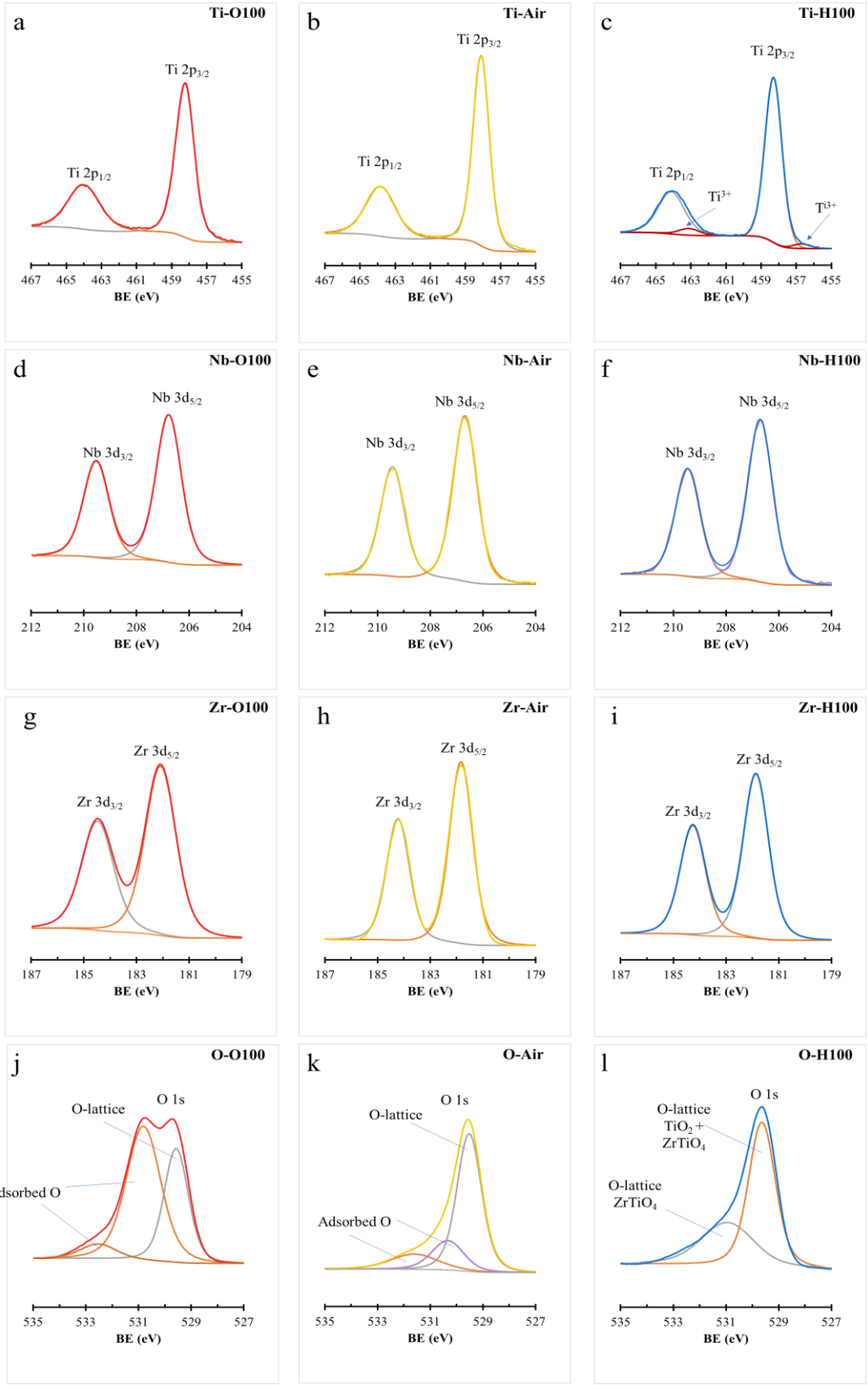

Figure 6-6 XPS core spectra of samples annealed in Air0, O100 and H100, (a-c) Ti, (d-f) Nb, (g-i) Zr, (j-l) O.

6.3 Optical Analysis

Diffuse Reflectance (DR) of the annealed MPNTs is shown in Figure 6-7 a. It can be seen that light scattering is the lowest in H100 which might be an argument suggesting decreased absorption probability. However, seeing that the surface reflectance is least in the wavelengths range 300-700 nm in H100 refutes that claim. It is also reasonable to find higher scattering in Air0 and Oxygen annealed samples (Air0 & O100) owing to their relatively larger diameters according to Mie scattering theory[57]. To understand how Hydrogen annealing affected the optical properties, a simple approach was used to calculate the refractive indices of the three samples similar to that followed in our previous work[58] and by Rambabu et al.[57]. Uniform morphology throughout the entire sample was assumed and following the effective medium theory as shown in equations 6-6 & 6-7. The needed volumetric calculations were performed by analyzing the SEM images to determine the filling factors of the samples. Table 6-3 shows the calculated refractive indices, external diameters and consequent Reflectance where it is evident that H100 has the lowest surface Reflectance in the range 300-700 nm.

$$n_M = [\, f_M * (n_O^q) + f_{air} * (n_{air}^q)]^{1/q} \qquad 6\text{-}6$$

$$R = (\frac{n_O - n_{air}}{n_O + n_{air}})^2 \qquad 6\text{-}7$$

where R, f_M and f_{air} are the reflectance; filling factors of the MPNTs, and Air0, respectively. The refractive index of Air0 (n_{Air0}) is set to 1 and the exponent is set to 2/3.

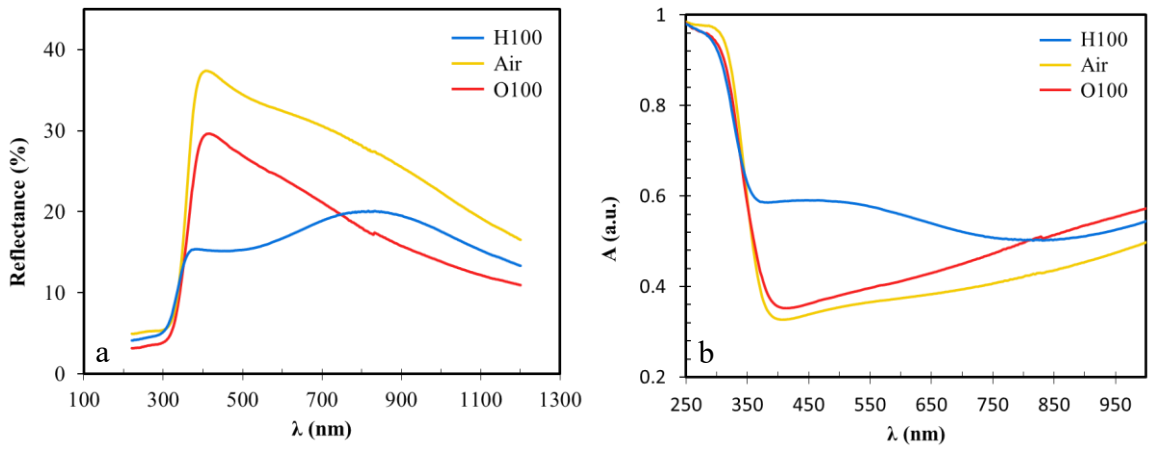

Figure 6-7 (a) DR and (b) Absorption Spectra of H100, Air0 & O100

Moreover, a clear hump up to ~ 800nm is shown in DR absorbance spectra of H100, Figure 6-7 b. This hump suggests the presence of states in the forbidden gap contributing to the absorption. It has been shown previously that holes generated through photon absorption may become trapped at OH^- groups adsorbed on the surface forming $OH^{\cdot}$ centers with absorption maximum at 350 nm up to 480 nm[59] i.e. deeply trapped.[60] Holes may also be trapped at bridging lattice O^{2-} forming O^- radicals absorbing in the NIR/Vis range[60,61]. It is worth mentioning that the incremental increase of absorption observed in the three samples beyond 850 nm may be attributed to the delocalized electron intra-band transition[61]. Accordingly, it is inevitable to say that both deep and shallow defects are present in the H100 where electronic transitions are possible, either from the VB to the defect states or from the defect states to the CB depending on the coupling between them[62]. This extended absorption range is in line with the samples' black colour, indicating defective states between CB and VB after reduction[63,64].

Table 6-3 Outer diameter, Refractive index, Reflectance and estimated band gap of the three conditions O100, Air0, and H100

Annealing Condition	**O100**	**Air0**	**H100**
Outer Diameter (nm)	418.31	411.33	371.45
Refractive Index	1.28	1.34	1.27
Reflectance (%)	1.54	2.13	1.41
Band Gap (eV)	3.25	3.27	3.1 tailed to 2.5

To further understand the nature of the states, VB XPS spectra were analyzed, Figure 6-8 b-e. A thorough analysis for the H100 shows a tail towards lower binding energies present, where the main absorption onset is located at 2.7 eV and maximum energy was blue shifted to 2.1 eV. Moreover, XPS fitting shows the presence of Ti^{3+} accompanied by the presence of Oxygen vacancies which in turn are formed due to the reductive atmosphere where oxygen leaves the surface in the form of H_2O after being

reduced by Hydrogen atoms at temperatures above 300°C [68]. In addition, the valence band spectra of H100 shows strong emission in the antibonding orbitals relative to Air0 and O100, this may be explained by the reduction of Ti^{4+} to Ti^{3+}, which causes an increase in the occupancy number of the antibonding orbitals [69]. These defective sites are present at 0.7 - 1 eV below the CBM in TiO_2 and Ti doped with Niobium [69,70]. Figure 6-9 shows the previously described defect positions present in the samples contributing to absorption making use of the band gap values calculated from Tauc plots (Figure 6-8 a) using indirect band-gap substitution.

A reduction in the bandgap of the H100s can clearly be observed, owing to the synergistic effect of the structural distortions, defects and the VB tail states discussed earlier, causing a lowering in the CBM with respect to the Fermi level. In addition, although the addition of Zr is expected to uplift the CBM and increase the band gap compared to TiO_2 owing to its higher d orbitals[71], the presence of $ZrTiO_4$ in H100 decreases the bandgap [12]. Finally, from the XRD results, the induced tensile strain is larger in H100 compared to O100 or Air0, leading to a reduction of the band gap [72]. This reduced band gap and defect states present in the H100 is expected to reflect in the density of charge carriers and lead to high photoactivity.

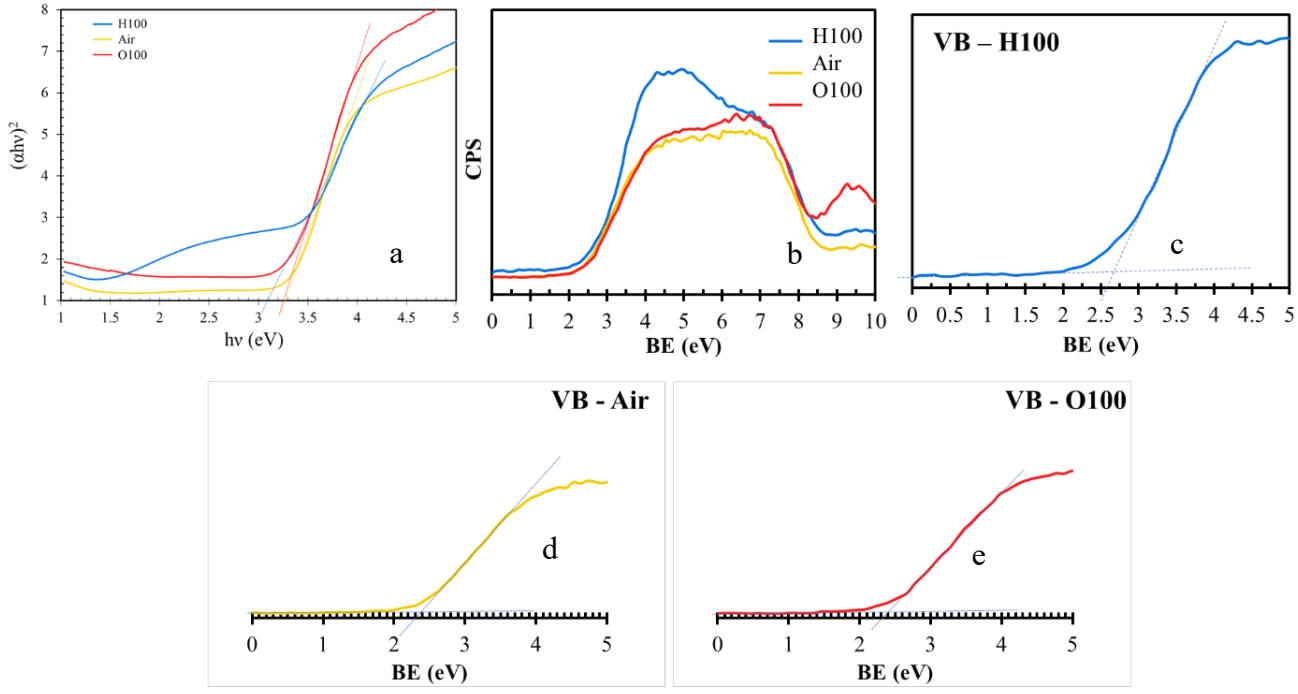

Figure 6-8 (a) Tauc Plots and (b-e) Valence band Spectra

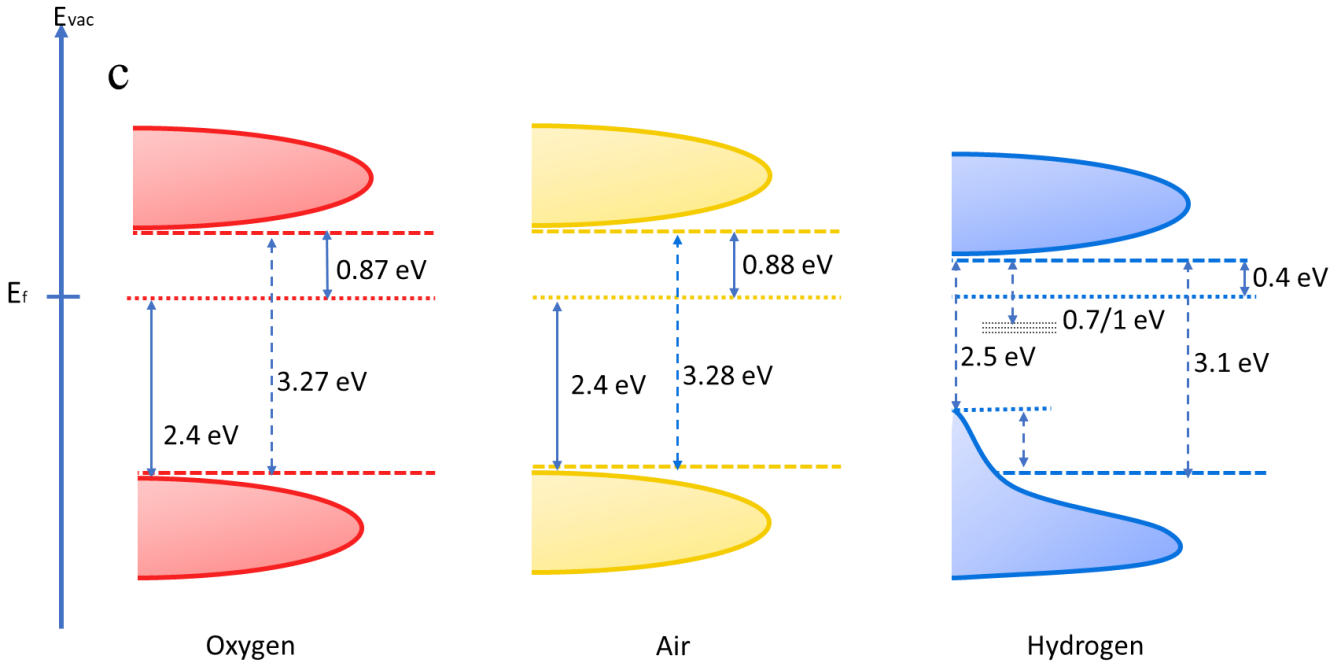

Figure 6-9 Schematic Illustration of the density of states, possible excitation mechanisms are indicated by dashed arrows

6.4 Photoelectrochemical Analysis

Photoelectrochemical water splitting performance was investigated for all the samples. Figure 6-10 shows the I-V plots, H100 showed much higher photocurrent compared to O100 and Air0 which is attributed to the reduced bandgap and the presence of valence band tail states discussed earlier. A positive/anodic shift in OCP is observed in H100 indicating the presence of high surface state density [73].

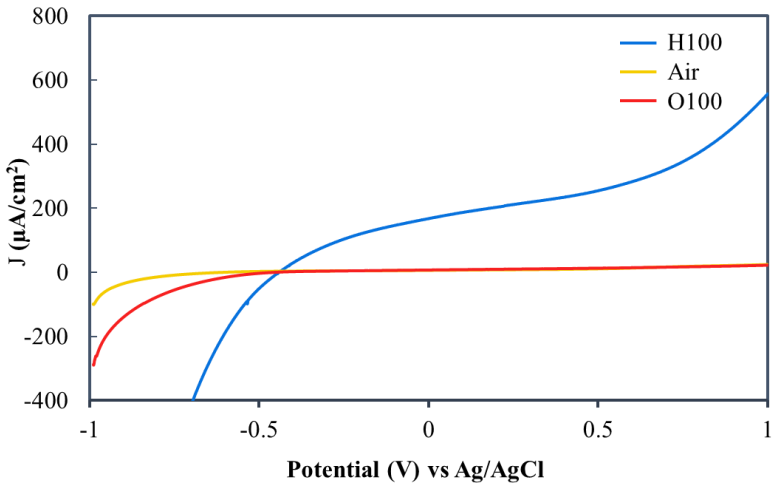

Figure 6-10 Linear sweep voltammetry of H100, Air0, & O100

In order to thoroughly explain this photocurrent enhancement, Mott-Schottky (MS) analysis was needed to extract the band-edge positions and have an insight on the charge carriers' density and flat-band potentials of the MPNTs. Figure 6-11 shows the MS plots obtained at 1 KHz of the annealed samples, which were used to calculate the charge density and the flat-band potential as described in equations 6-8 & 6-9

$$\frac{1}{C^2} = \frac{2}{N_D \varepsilon \varepsilon_0 e}\left[(V - V_{FB}) - \frac{kT}{e}\right] \qquad 6\text{-}8$$

$$N_D = -\left[\frac{2}{\varepsilon \varepsilon_0 e}\right]\left[\frac{d\left(1/_{C^2}\right)}{d(V)}\right]^{-1} \qquad 6\text{-}9$$

where N_D is the donor density, e is the electron charge, ε_0 is the permittivity of free space, ε is the dielectric constant calculated from the measured refracted index where $\varepsilon = n^2 = 20.07$, V is the electrode applied voltage, V_{FB} is the flat-band potential, k is Boltzmann's constant and T is the room temperature 25°C. It can be observed that the plot of C^{-2} versus V in H100 is not very linear, this behaviour could be related to the non-uniform nature of the multipodal morphology combined with the reducing annealing atmosphere, resulting in defective and distorted structure. This defective structure would affect the geometric distribution of the lattice defects [74]. Furthermore, the non-linear MS behaviour can be attributed to the abundance of lattice defects, deep trap states and grain boundary electron traps formed by reduced crystallinity; where these states progressively ionize with increasing the applied potential [75].

Table 6-4 lists the V_{FB} and N_D of Air0, O100 and H100, where H100 shows the most negative/cathodic V_{FB} compared to O100 and Air0. Although this may indicate the need for higher overpotential to overcome the increased band bending formed by the larger depletion region width (W_{sc}) according to equation 6-10, good charge separation is achieved due to the sufficiency of the depletion region width obtained.

$$W_{sc} = \sqrt{\frac{2\varepsilon\varepsilon_0}{eN_D}}(V - V_{FB}) \qquad 6\text{-}10$$

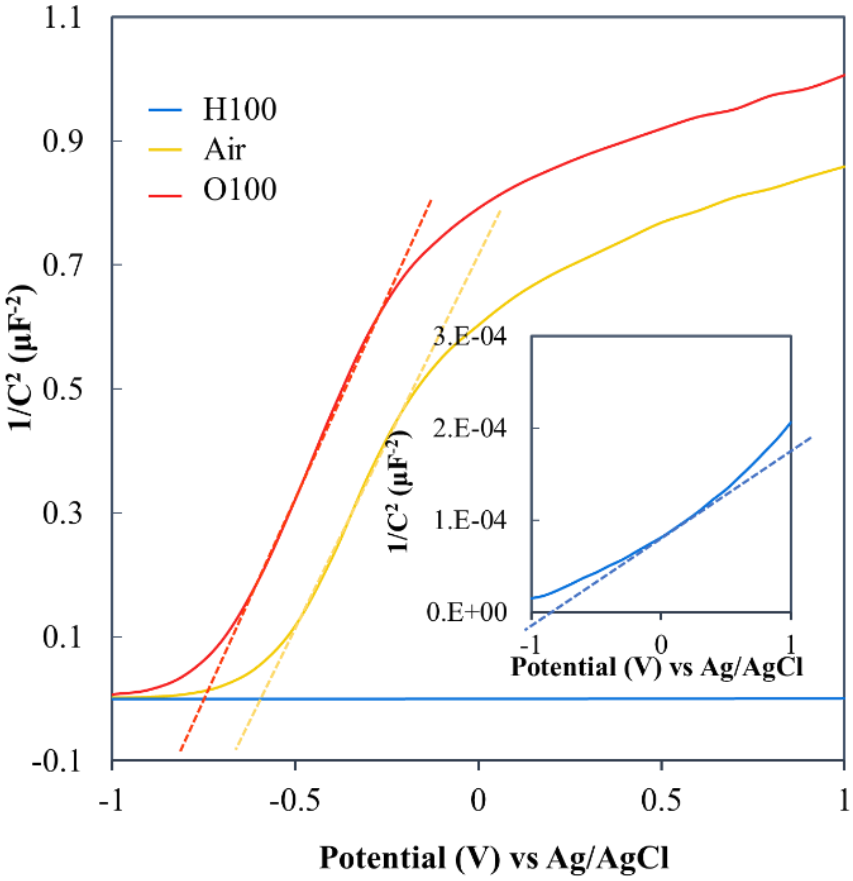

Figure 6-11 MS plots of H100, Air0 & O100

Table 6-4 OCP, V_{FB} vs. Ag/AgCl at pH=14, N_D, E_{CB} (vs. NHE at pH=0), E_{VB} (vs. NHE at pH=0) of the three conditions O100, Air0, and H100

Annealing Condition	**O100**	**Air0**	**H100**
OCP (V)	-0.46	-0.6	-0.45
V_{FB} (vs. Ag/AgCl at pH=14)	-0.774	-0.633	-1.048
Donor Density (cm^{-3})	2.17E+19	2.57E+19	3.19E+23
E_{CB} (vs. NHE at pH=0)	0.23	0.37	-0.29
E_{VB} (vs. NHE at pH=0)	3.50	3.65	2.26

It can be also seen that the donor density in H100 has increased by four orders of magnitude. From valence band XPS spectra, it is observed that the Fermi level is closer to the CBM in the H100, this occurs when there is an increase in the donor density. This

can be attributed to two reasons: the addition of Niobium which acts as a donor impurity owing to its high electron cloud density[76], and the presence of donor-like surface states made of Oxygen vacancies/Ti^{3+} which increase the charge carriers density as can be seen from the defect Equations 6-11 to 6-14 [60]. Although Titanium (Ti^{4+}) substitution by Niobium(Nb^{5+}) favours the presence of excess Oxygen owing to its higher oxidation state, the presence of a reducing atmosphere forming oxygen vacancies will synergistically contribute to the excess in charge carriers, which is the case in H100. This is reflected in the donor density obtained from MS analysis. The addition of Zr will not contribute to the carrier density other than the bandgap reduction discussed earlier, as $ZrTiO_4$ is not photoactive [12]. However, $ZrTiO_4$ may create deep defects that act as recombination centres, hindering the photocurrent. This said, it is clear that the aforementioned valence band tail states, the band gap reduction, the formation of Ti^{3+}, the reduced refractive index, along with the reduced surface reflectance in H100 are believed to be adding to the charge carriers' generation probability.

Formation of Ti^{3+}

$$Ti_{Ti}^{x} + 3O_{O}^{x} + 3H_2 \rightarrow Ti_{i}^{\cdot\cdot} + 3e^{-} + 3H_2O \qquad 6\text{-}11$$

Formation of Oxygen vacancies

$$O_{O}^{x} \rightarrow \frac{1}{2}O_2 + V_{O}^{\cdot\cdot} + 2e^{-} \qquad 6\text{-}12$$

Titanium substitution by Niobium in a non-reducing atmosphere

$$Nb_2O_5 \rightarrow 2Nb_{Ti}^{\cdot} + 4O_{O}^{x} + 2e^{-} + \frac{1}{2}O_2 \qquad 6\text{-}13$$

Titanium substitution by Niobium in a reducing atmosphere

$$Nb_2O_5 \rightarrow 2Nb_{Ti}^{\cdot} + V_{O}^{\cdot\cdot} + 4e^{-} + \frac{5}{2}O_2 \qquad 6\text{-}14$$

To get a deeper insight on the defects present in the samples, a careful[-3] examination of the J-t transient current response curves measured at constant external bias of 0.5 $V_{Ag/AgCl}$ in Figure 6-12 is needed. As expected, the O100 and Air0 show almost zero dark currents. This is in alignment with the structural analysis defying the presence of mid-gap states, as those states act as trap states and are the main source of the dark current. On the other hand, a high dark current is observed in the H100. It is noted that the nature of Ti^{3+} defects whether localized

or de-localized will affect their coupling with the delocalized conduction band states. Localized defects result in deteriorating the mobility of electrons and may eventually not contribute to the photocurrent. The much higher photocurrent of H100 relative to O100 and Air0 suggests the presence of bulk and abundant Ti^{3+} forming Oxygen vacancies which are uneasily oxidized and are considered as electron suppliers to the CB. However, the high dark current suggests the presence of easily oxidized localized surface Ti^{3+} close to the CB minimum which could pin the Fermi level, resulting in a high dark current [8,62,77]. This could also explain the anodic shift in the OCP and cathodic shift in V_{FB} [73]. Moreover, the inactive $ZrTiO_4$ formed by Zr ions segregation from Anatase phase, lead to decreased crystallinity, resulting in the formation of a smaller depletion region, which is supported by the increase in donor density according to Equation 6-10. This may have influenced the scattering of the charge carriers, making them become trapped at deep defects, and leading to a rise in the dark current [78].

The stability of the photoanodes can be assessed also from the J-t curves, where the samples have shown good stability over the test duration. In addition, It can be seen that a very sharp decay is present under light-off conditions in all the samples indicating the ease of carrier transport, equation 6-15 [79,80].

$$I = I_0 \, e^{-t/\tau_d} \qquad 6\text{-}15$$

where I is the photocurrent, I_0 is the initial photocurrent, t is time, and τ_d is the decay time.

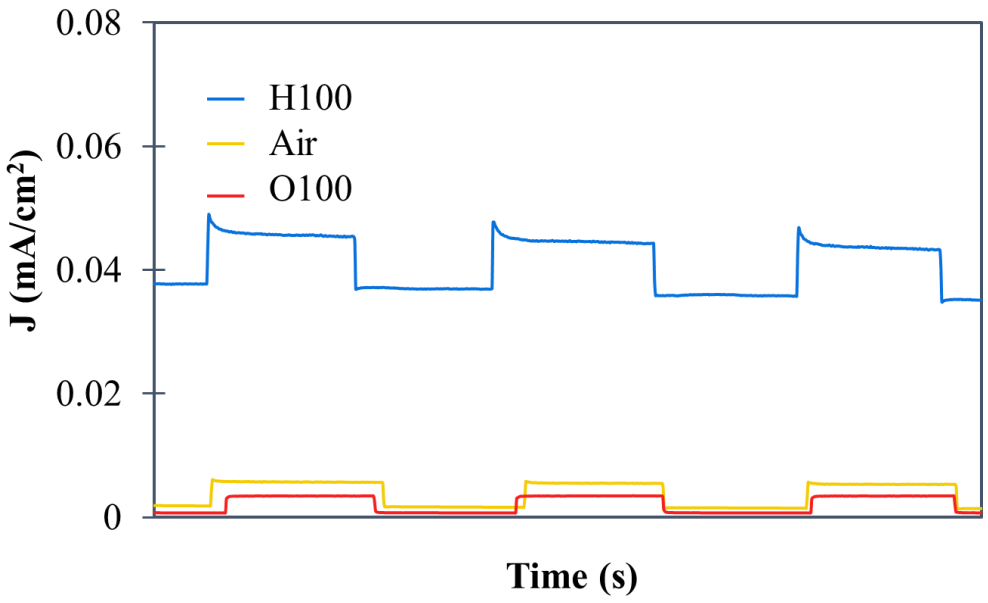

Figure 6-12 J-t plots of H100, Air0, and O100

Finally, the relative band alignment for the three conditions is plotted in Figure 6-13 for further clarification using equation 6-16.

$$E_{NHE} = E_{Ag/AgCl} + 0.197 + 0.059 * pH \qquad 6\text{-}16$$

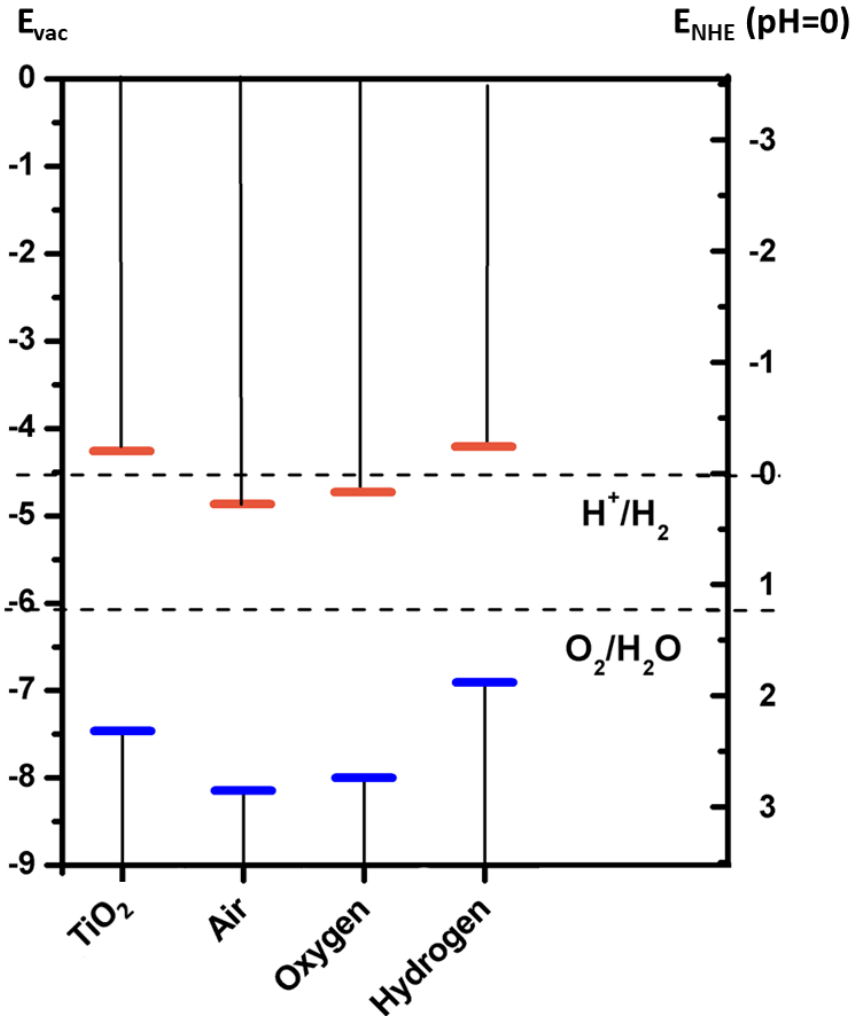

Figure 6-13 Band alignment vs. NHE and Vacuum of pure TiO2, H100, Air0, and O100 relative to the water redox potentials at pH=0

6.5 CZTS Deposition

CZTS nanoparticles were synthesized using non-stoichiometric concentrations of the precursors via a facile solvothermal methods; where the particle size as shown in Figure 6-14 b is in the range of ~200nm. It is worth noting that before the washing off the polyethylene glycol 400 used in the preparation, the nanoparticles look like flakes (Figure 6-14 a) which may be attributed to the surface passivation aided by the long chain solvent [81]. Electrophoresis was used to deposit the CZTS nanoparticles on H100 samples as shown in Figure 6-14 c, the particles are well distributed on the surface. Figure 6-15 shows the XRD of CZTS, where the three sharp peaks indicate enhanced crystallinity [82] and are assigned to (111), (220) and (311) which confirm the presence of tetragonal high quality Kesterite phase [83].

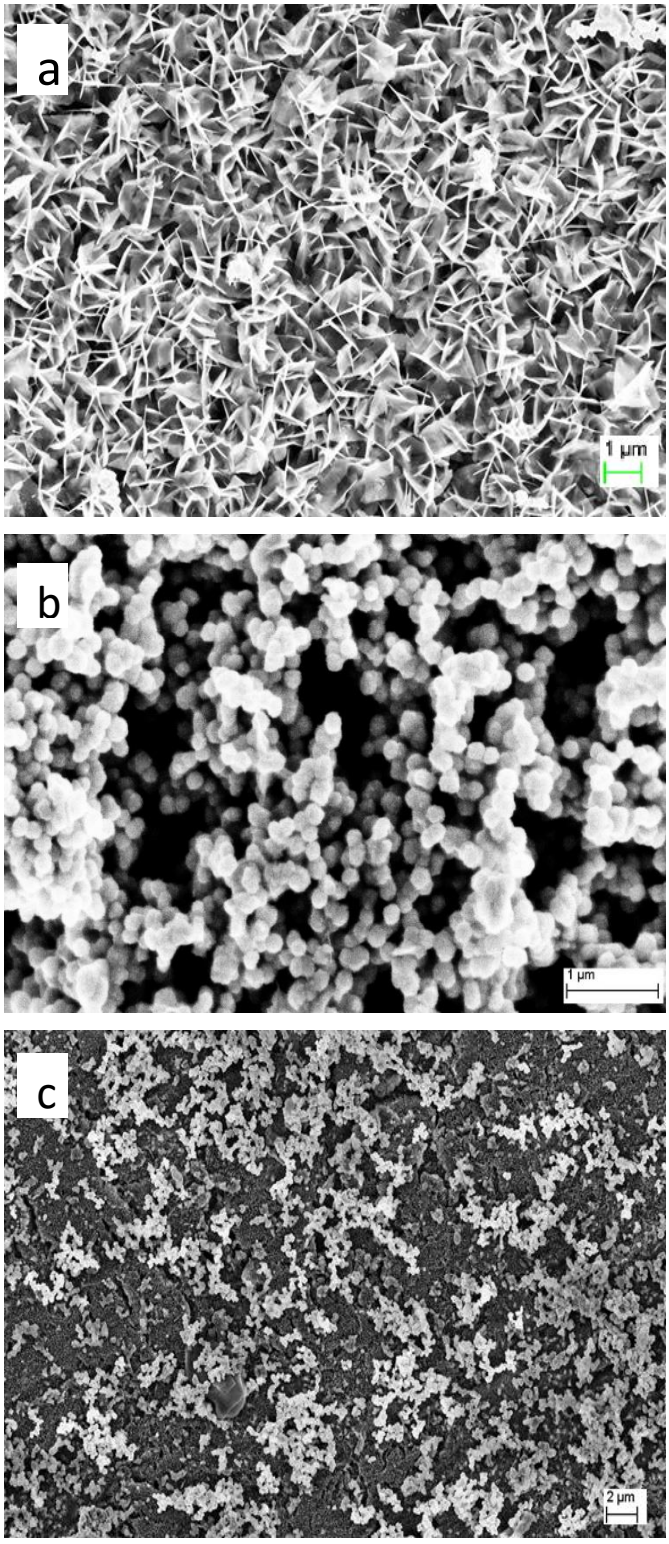

Figure 6-14 SEM images of CZTS (a) before washing (b) after washing (c) top view of CZTS deposited on Ti-Nb-Zr MPNTs

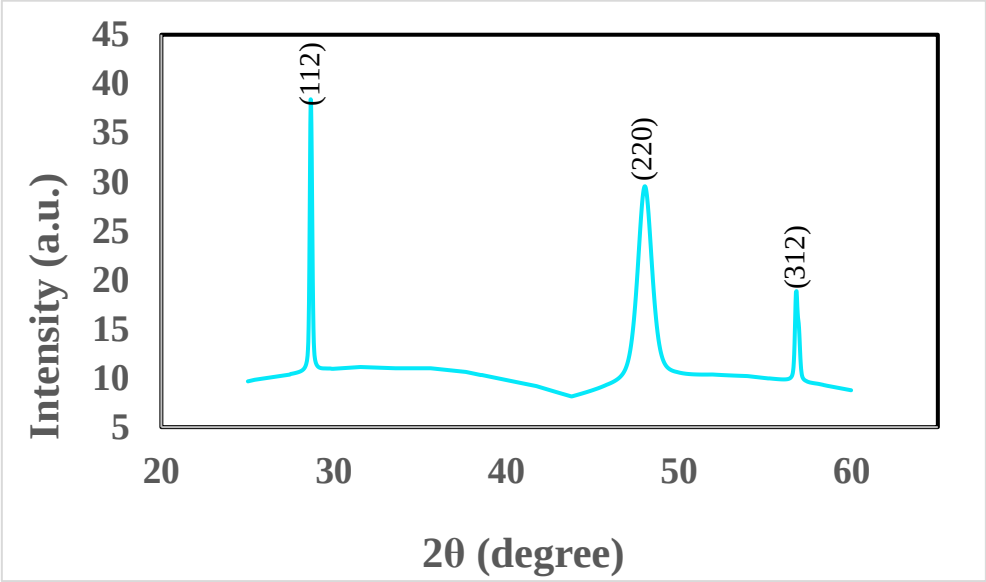

Figure 6-15 CZTS XRD

On attempting to study the photoelectrochemical performance of the H100 with CZTS deposited on them, it was found that a great enhancement in the photocurrent was achieved, about 6 times as shown in Figure 6-16. Upon examining the absorbance spectra of both, we see that only a slight shift is induced by the CZTS addition. Therefore, it cannot explain the large photocurrent. On testing several cycles it is noticed that the CZTS is not stable in the alkaline electrolyte; however, the large current could indicate the generation of a pn junction with desirable alignment that enhance charge separation and cause charge carrier injection [84].

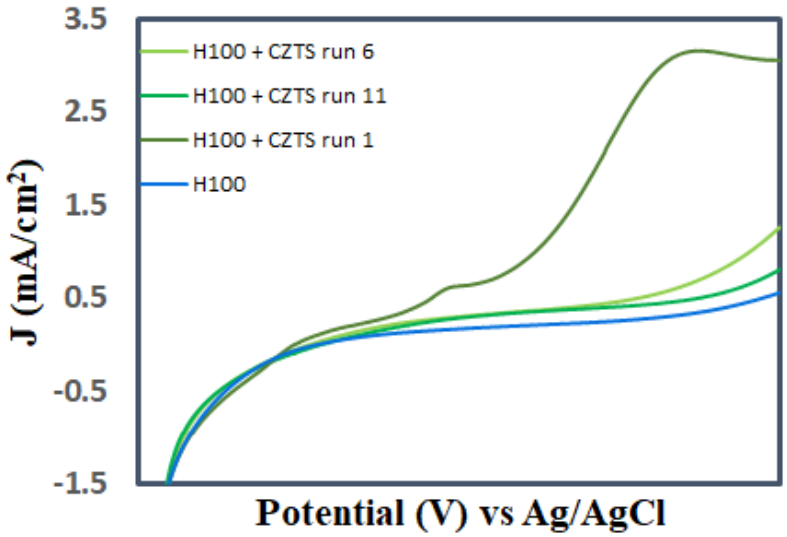

Figure 6-16 J-V plots of H100 vs H100+CZTS at different runs

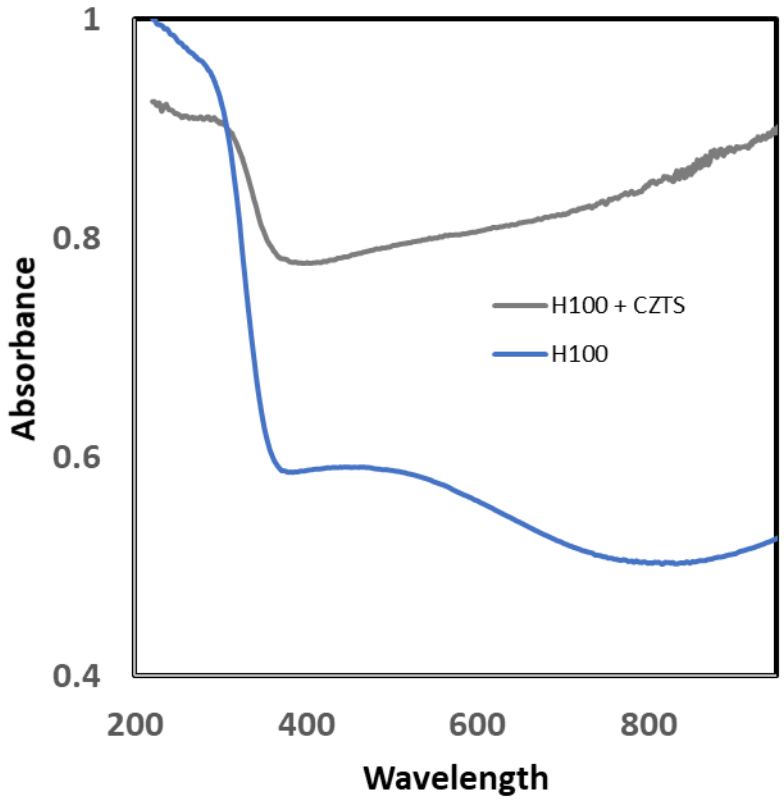

Figure 6-17 Absorbance Spectra of H100 & H100+CZTS

References

(1) Liu, Q.; Ding, D.; Ning, C.; Wang, X. ??-Fe2O3/Ti-Nb-Zr-O Composite Photoanode for Enhanced Photoelectrochemical Water Splitting. *Mater. Sci. Eng. B Solid-State Mater. Adv. Technol.* **2015**, *196*, 15–22.

(2) Huang, X.; Zhu, E.; Chen, Y.; Li, Y.; Chiu, C.-Y.; Xu, Y.; Lin, Z.; Duan, X.; Huang, Y. A Facile Strategy to Pt_3Ni Nanocrystals with Highly Porous Features as an Enhanced Oxygen Reduction Reaction Catalyst. *Adv. Mater.* **2013**, *25*, 2974–2979.

(3) Zhang, H.; Wang, H.; Eid, K.; Wang, L. Nanoparticle in Nanocage: Au@Porous Pt Yolk-Shell Nanoelectrocatalysts. *Part. Part. Syst. Charact.* **2015**, *32*, 863–868.

(4) Eid, K.; Wang, H.; He, P.; Wang, K.; Ahamad, T.; Alshehri, S. M.; Yamauchi, Y.; Wang, L. One-Step Synthesis of Porous Bimetallic PtCu Nanocrystals with High Electrocatalytic Activity for Methanol Oxidation Reaction. *Nanoscale* **2015**, *7*, 16860–16866.

(5) Lu, Q.; Wang, H.; Eid, K.; Alothman, Z. A.; Malgras, V.; Yamauchi, Y.; Wang, L. Synthesis of Hollow Platinum-Palladium Nanospheres with a Dendritic Shell as Efficient Electrocatalysts for Methanol Oxidation. *Chem. - An Asian J.* **2016**, *11*, 1939–1944.

(6) Eid, K.; Wang, H.; Malgras, V.; Alothman, Z. A.; Yamauchi, Y.; Wang, L. Facile Synthesis of Porous Dendritic Bimetallic Platinum-Nickel Nanocrystals as Efficient Catalysts for the Oxygen Reduction Reaction. *Chem. - An Asian J.* **2016**, *11*, 1388–1393.

(7) Eid, K.; Ahmad, Y. H.; AlQaradawi, S. Y.; Allam, N. K. Rational Design of Porous Binary Pt-Based Nanodendrites as Efficient Catalysts for Direct Glucose Fuel Cells over a Wide pH Range. *Catal. Sci. Technol.* **2017**, *7*.

(8) Mohamed, A. M.; Amer, A. W.; AlQaradawi, S. Y.; Allam, N. K. On the Nature of Defect States in Tungstate Nanoflake Arrays as Promising Photoanodes in Solar Fuel Cells. *Phys. Chem. Chem. Phys.* **2016**, *18*, 22217–22223.

(9) Suryanarayana, C.; Norton, M. G. *X-Ray Diffraction : A Practical Approach*; 1st ed.; Springer US, 1998.

(10) Shannon, R. D. Revised Effective Ionic Radii and Systematic Studies of Interatomic Distances in Halides and Chalcogenides. *Acta Crystallogr. Sect. A* **1976**, *32*, 751–767.

(11) Kumar, A.; Kumar, J. On the Synthesis and Optical Absorption Studies of Nano-Size Magnesium Oxide Powder. *J. Phys. Chem. Solids* **2008**, *69*, 2764–2772.

(12) Gao, B.; Lim, T. M.; Subagio, D. P.; Lim, T. T. Zr-Doped TiO_2 for Enhanced Photocatalytic Degradation of Bisphenol A. *Appl. Catal. A Gen.* **2010**, *375*, 107–115.

(13) Zhao, W.; Zhao, W.; Zhu, G.; Lin, T.; Xu, F.; Huang, F. Black Nb_2O_5 Nanorods with Improved Solar Absorption and Enhanced Photocatalytic Activity. *Dalt. Trans.* **2016**, *45*, 3888–3894.

(14) Balachandran, U.; Eror, N. G. Raman Spectra of Titanium Dioxide. *J. Solid State Chem.* **1982**, *42*, 276–282.

(15) Dohcevic-Mitrovic, Z. D.; Šćepanović, M. J.; Grujić-Brojčin, M. U.; Popović, Z. V.; Bošković, S. B.; Matović, B. M.; Zinkevich, M. V.; Aldinger, F. The Size and Strain Effects on the Raman Spectra of $Ce_{1-x}Nd_xO_{2-\delta}$ ($0 \leq x \leq 0.25$) Nanopowders. *Solid State Commun.* **2006**, *137*, 387–390.

(16) Venkatasubbu, G. D.; Ramakrishnan, V.; Sasirekha, V.; Ramasamy, S.; Kumar, J. Influence of Particle Size on the Phonon Confinement of TiO_2 Nanoparticles. *J. Exp. Nanosci.* **2014**, *9*, 661–668.

(17) Georgescu, D.; Baia, L.; Ersen, O.; Baia, M.; Simon, S. Experimental Assessment of the Phonon Confinement in TiO_2 Anatase Nanocrystallites by Raman Spectroscopy. *J. Raman Spectrosc.* **2012**, *43*, 876–883.

(18) Balaji, S.; Djaoued, Y.; Robichaud, J. Phonon Confinement Studies in Nanocrystalline Anatase-TiO_2 Thin Films by Micro Raman Spectroscopy. *J. Raman Spectrosc.* **2006**, *37*, 1416–1422.

(19) Eder, D.; Windle, A. H. Carbon–Inorganic Hybrid Materials: The Carbon-Nanotube/TiO_2 Interface. *Adv. Mater.* **2008**, *20*, 1787–1793.

(20) Clemens, P.; Wei, X.; Wilson, B. L.; Thomas, R. L. Anatase Titanium Dioxide Coated Single Wall Carbon Nanotubes Manufactured by Sonochemical-Hydrothermal

Technique. *Open J. Compos. Mater.* **2013**, *3*, 21–32.

(21) Auffan, M.; Rose, J.; Bottero, J.-Y.; Lowry, G. V.; Jolivet, J.-P.; Wiesner, M. R. Towards a Definition of Inorganic Nanoparticles from an Environmental, Health and Safety Perspective. *Nat. Nanotechnol.* **2009**, *4*, 634–641.

(22) Zhang, Y.; Wu, W.; Zhang, K.; Liu, C.; Yu, A.; Peng, M.; Zhai, J. Raman Study of 2D Anatase TiO_2 Nanosheets. *Phys. Chem. Chem. Phys.* **2016**, *18*, 32178–32184.

(23) Hardcastle, F. D.; Wachs, I. E. Determination of Molybdenum–oxygen Bond Distances and Bond Orders by Raman Spectroscopy. *J. Raman Spectrosc.* **1990**, *21*, 683–691.

(24) Sahoo, M.; Yadav, A. K.; Jha, S. N.; Bhattacharyya, D.; Mathews, T.; Sahoo, N. K.; Dash, S.; Tyagi, A. K. Nitrogen Location and Ti–O Bond Distances in Pristine and N-Doped TiO_2 Anatase Thin Films by X-Ray Absorption Studies. *J. Phys. Chem. C* **2015**, *119*, 17640–17647.

(25) Hamedani, H. A.; Allam, N. K.; El-Sayed, M. A.; Khaleel, M. A.; Garmestani, H.; Alamgir, F. M. An Experimental Insight into the Structural and Electronic Characteristics of Strontium-Doped Titanium Dioxide Nanotube Arrays. *Adv. Funct. Mater.* **2014**, *24*, 6783–6796.

(26) Naldoni, A.; Allieta, M.; Santangelo, S.; Marelli, M.; Fabbri, F.; Cappelli, S.; Bianchi, C. L.; Psaro, R.; Dal Santo, V. Effect of Nature and Location of Defects on Bandgap Narrowing in Black TiO_2 Nanoparticles. *J. Am. Chem. Soc.* **2012**, *134*, 7600–7603.

(27) Zheng, Z.; Huang, B.; Lu, J.; Wang, Z.; Qin, X.; Zhang, X.; Dai, Y.; Whangbo, M.-H. Hydrogenated Titania: Synergy of Surface Modification and Morphology Improvement for Enhanced Photocatalytic Activity. *Chem. Commun.* **2012**, *48*, 5733.

(28) Yu, P. Y.; Cardona, M. *Fundamentals of Semiconductors : Physics and Materials Properties*; Springer, 2010.

(29) Chen, X.; Liu, L.; Yu, P. Y.; Mao, S. S. Increasing Solar Absorption for Photocatalysis with Black Hydrogenated Titanium Dioxide Nanocrystals. *Science* **2011**, *331*, 746–750.

(30) Atashbar, M. Z.; Sun, H. T.; Gong, B.; Wlodarski, W.; Lamb, R. XPS Study of Nb-Doped Oxygen Sensing TiO_2 Thin Films Prepared by Sol-Gel Method. *Thin Solid Films*

1998, *326*, 238–244.

(31) Feng, N.; Liu, F.; Huang, M.; Zheng, A.; Wang, Q.; Chen, T.; Cao, G.; Xu, J.; Fan, J.; Deng, F. Unravelling the Efficient Photocatalytic Activity of Boron-Induced Ti^{3+} Species in the Surface Layer of TiO_2. *Sci. Rep.* **2016**, *6*, 34765.

(32) Briggs, D. (David); Grant, J. T. *Surface Analysis by Auger and X-Ray Photoelectron Spectroscopy*; IM Publications, 2003.

(33) Briggs, D. (David). *Handbook of X-Ray and Ultraviolet Photoelectron Spectroscopy*; Heyden, 1977.

(34) Li, L.; Wang, L.; Hu, T.; Zhang, W.; Zhang, X.; Chen, X. Preparation of Highly Photocatalytic Active CdS/TiO_2 Nanocomposites by Combining Chemical Bath Deposition and Microwave-Assisted Hydrothermal Synthesis. *J. Solid State Chem.* **2014**, *218*, 81–89.

(35) Jing, L.; Xin, B.; Yuan, F.; Xue, L.; Wang, B.; Fu, H. Effects of Surface Oxygen Vacancies on Photophysical and Photochemical Processes of Zn-Doped TiO_b Nanoparticles and Their Relationships. *J. Phys. Chem. B* **2006**, *110*, 17860–17865.

(36) Hsieh, P.-T.; Chen, Y.-C.; Kao, K.-S.; Wang, C.-M. Luminescence Mechanism of ZnO Thin Film Investigated by XPS Measurement. *Appl. Phys. A* **2007**, *90*, 317–321.

(37) Xu, N.; Liu, L.; Sun, X.; Liu, X.; Han, D.; Wang, Y.; Han, R.; Kang, J.; Yu, B. Characteristics and Mechanism of Conduction/set Process in TiN⁄ZnO⁄Pt Resistance Switching Random-Access Memories. *Appl. Phys. Lett.* **2008**, *92*, 232112.

(38) Li, X.; Wang, Y.; Liu, W.; Jiang, G.; Zhu, C. Study of Oxygen Vacancies′ Influence on the Lattice Parameter in ZnO Thin Film. *Mater. Lett.* **2012**, *85*, 25–28.

(39) Jing, L.; Xin, B.; Yuan, F.; Xue, L.; Wang, B.; Fu, H. Effects of Surface Oxygen Vacancies on Photophysical and Photochemical Processes of Zn-Doped TiO_2 Nanoparticles and Their Relationships. *J. Phys. Chem. B* **2006**, *110*, 17860–17865.

(40) Allam, N.; El-Sayed, M. Photoelectrochemical Water Oxidation Characteristics of Anodically Fabricated TiO_2 Nanotube Arrays: Structural and Optical Properties. *J. Phys. Chem. C* **2010**, 12024–12029.

(41) Samir, M.; Salama, M.; Allam, N. K. Sub-100 Nm TiO_2 Tubular Architectures for Efficient Solar Energy Conversion. *J. Mater. Chem. A* **2016**, *4*, 9375–9380.

(42) Huang, H.; Wang, C.; Huang, J.; Wang, X.; Du, Y.; Yang, P. Structure Inherited Synthesis of N-Doped Highly Ordered Mesoporous Nb_2O_5 as Robust Catalysts for Improved Visible Light Photoactivity. *Nanoscale* **2014**, *6*, 7274–7280.

(43) Lukáč, J.; Klementová, M.; Bezdička, P.; Bakardjieva, S.; Šubrt, J.; Szatmáry, L.; Bastl, Z.; Jirkovský, J. Influence of Zr as TiO_2 Doping Ion on Photocatalytic Degradation of 4-Chlorophenol. *Appl. Catal. B Environ.* **2007**, *74*, 83–91.

(44) Yu, J. C.; Jun Lin, A.; Kwok, R. W. M. $Ti_{1-x}Zr_xO_2$ Solid Solutions for the Photocatalytic Degradation of Acetone in Air. *J. Phys. Chem. B* **1998**, *102*, 5094–5098.

(45) Cao, Y.; Yang, W.; Zhang, W.; Liu, G.; Yue, P. Improved Photocatalytic Activity of Sn4+ Doped TiO_2 Nanoparticulate Films Prepared by Plasma-Enhanced Chemical Vapor Deposition. *New J. Chem.* **2004**, *28*, 218.

(46) Finazzi, E.; Di Valentin, C.; Pacchioni, G. Nature of Ti Interstitials in Reduced Bulk Anatase and Rutile TiO_2. *J. Phys. Chem. C* **2009**, *113*, 3382–3385.

(47) Finazzi, E.; Di Valentin, C.; Pacchioni, G.; Selloni, A. Excess Electron States in Reduced Bulk Anatase TiO_2: Comparison of Standard GGA, GGA+U, and Hybrid DFT Calculations. *J. Chem. Phys.* **2008**, *129*, 154113.

(48) Wendt, S.; Sprunger, P. T.; Lira, E.; Madsen, G. K. H.; Li, Z.; Hansen, J. O.; Matthiesen, J.; Blekinge-Rasmussen, A.; Laegsgaard, E.; Hammer, B.; *et al.* The Role of Interstitial Sites in the Ti3d Defect State in the Band Gap of Titania. *Science.* **2008**, *320*, 1755–1759.

(49) Tao, J.; Luttrell, T.; Batzill, M. A Two-Dimensional Phase of TiO_2 with a Reduced Bandgap. *Nat. Chem.* **2011**, *3*, 296–300.

(50) Morgan, B. J.; Watson, G. W. Intrinsic N-Type Defect Formation in TiO_2 : A Comparison of Rutile and Anatase from GGA+ U Calculations. *J. Phys. Chem. C* **2010**, *114*, 2321–2328.

(51) Janotti, A.; Varley, J. B.; Rinke, P.; Umezawa, N.; Kresse, G.; Van de Walle, C. G.

Hybrid Functional Studies of the Oxygen Vacancy in TiO_2. *Phys. Rev. B* **2010**, *81*, 85212.

(52) Bertóti, I.; Mohai, M.; Sullivan, J. L.; Saied, S. O. Surface Characterisation of Plasma-Nitrided Titanium: An XPS Study. *Appl. Surf. Sci.* **1995**, *84*, 357–371.

(53) Werfel, F.; Brümmer, O. Corundum Structure Oxides Studied by XPS. *Phys. Scr.* **1983**, *28*, 92–96.

(54) McCafferty, E.; Wightman, J. P. Determination of the Concentration of Surface Hydroxyl Groups on Metal Oxide Films by a Quantitative XPS Method. *Surf. Interface Anal.* **1998**, *26*, 549–564.

(55) Yasuda, K.; Schmuki, P. Electrochemical Formation of Self-Organized Zirconium Titanate Nanotube Multilayers. *Electrochem. commun.* **2007**, *9*, 615–619.

(56) Ikawa, H.; Yamada, T.; Kojima, K.; Matsumoto, S. X-ray Photoelectron Spectroscopy Study of High- and Low-Temperature Forms of Zirconium Titanate. *J. Am. Ceram. Soc.* **1991**, *74*, 1459–1462.

(57) Rambabu, Y.; Jaiswal, M.; Roy, S. C. Enhanced Photoelectrochemical Performance of Multi-Leg TiO_2 Nanotubes through Efficient Light Harvesting. *J. Phys. D. Appl. Phys.* **2015**, *48*, 295302.

(58) Omar, M. M.; Fawzy, S. M.; El-Shabasy, A. B.; Allam, N. Large-Diameter Light-Scattering Complex Multipodal Nano-Tubes with Graded Refractive Index: Insights into Their Formation Mechanism and Photoelectrochemical Performance. *J. Mater. Chem. A* **2017**.

(59) Lawless, D.; Serpone, N.; Meisel, D. Role of OH Radlcals and Trapped Holes in Photocatalysis. A Pulse Radiolysis Study. *J. Phys. Chem.* **1991**, *95*, 5166–5170.

(60) Schneider, J.; Matsuoka, M.; Takeuchi, M.; Zhang, J.; Horiuchi, Y.; Anpo, M.; Bahnemann, D. W. Understanding TiO_2 Photocatalysis: Mechanisms and Materials. *Chem. Rev.* **2014**, *114*, 9919–9986.

(61) Yoshihara, T.; Katoh, R.; Furube, A.; Tamaki, Y.; Murai, M.; Hara, K.; Murata, S.; Arakawa, H.; Tachiya, M. Identification of Reactive Species in Photoexcited

Nanocrystalline TiO 2 Films by Wide-Wavelength-Range (400−2500 Nm) Transient Absorption Spectroscopy. *J. Phys. Chem. B* **2004**, *108*, 3817–3823.

(62) Fan Hai-Bo, Yang Shao-Yan, Zhan Pan-Feng, Wei Hong-Yuan, Liu Xian- Lin, Jiao Chun-Mei, Zhu Qin-Sheng, C. Y.-H. W. Z.-G. Investigation of Oxygen Vacavcy and Interstitial Oxygen Defects in ZnO Films by Photoluminescence Ad X-Ray Photoelectron Spectroscopy. *Chin. Phys. Lett* **2007**, *24*, 2018.

(63) Gordon, T. R.; Cargnello, M.; Paik, T.; Mangolini, F.; Weber, R. T.; Fornasiero, P.; Murray, C. B. Nonaqueous Synthesis of TiO_2 Nanocrystals Using TiF 4 to Engineer Morphology, Oxygen Vacancy Concentration, and Photocatalytic Activity. *J. Am. Chem. Soc.* **2012**, *134*, 6751–6761.

(64) Wang, G.; Wang, H.; Ling, Y.; Tang, Y.; Yang, X.; Fitzmorris, R. C.; Wang, C.; Zhang, J. Z.; Li, Y. Hydrogen-Treated TiO_2 Nanowire Arrays for Photoelectrochemical Water Splitting. *Nano Lett.* **2011**, *11*, 3026–3033.

(65) Chen, X.; Liu, L.; Yu, P. Y.; Mao, S. S. Increasing Solar Absorption for Photocatalysis with Black Hydrogenated Titanium Dioxide Nanocrystals. *Science.* **2011**, *331*, 746–750.

(66) Sinhamahapatra, A.; Jeon, J.-P.; Kang, J.; Han, B.; Yu, J.-S. Oxygen-Deficient Zirconia (ZrO_{2-x}): A New Material for Solar Light Absorption. *Sci. Rep.* **2016**, *6*, 27218.

(67) Zhi-yong, Z. Electronic Structure and Optical Properties of. *Phys. Lett. A* **2007**, *16*, 2791–2797.

(68) Xiong, L. Bin; Li, J. L.; Yang, B.; Yu, Y. Ti^{3+} in the Surface of Titanium Dioxide: Generation, Properties and Photocatalytic Application. *J. Nanomater.* **2012**, *2012*.

(69) Naldoni, A.; Allieta, M.; Santangelo, S.; Marelli, M.; Fabbri, F.; Cappelli, S.; Bianchi, C. L.; Psaro, R.; Dal Santo, V. Effect of Nature and Location of Defects on Bandgap Narrowing in Black TiO_2 Nanoparticles. *J. Am. Chem. Soc.* **2012**, *134*, 7600–7603.

(70) Nowotny, J.; Alim, M. A.; Bak, T.; Idris, M. A.; Ionescu, M.; Prince, K.; Sahdan, M. Z.; Sopian, K.; Mat Teridi, M. A.; Sigmund, W. Defect Chemistry and Defect Engineering of TiO_2 -Based Semiconductors for Solar Energy Conversion. *Chem. Soc. Rev.* **2015**, *44*, 8424–8442.

(71) Yin, W. J.; Tang, H.; Wei, S. H.; Al-Jassim, M. M.; Turner, J.; Yan, Y. Band Structure Engineering of Semiconductors for Enhanced Photoelectrochemical Water Splitting: The Case of TiO_2. *Phys. Rev. B - Condens. Matter Mater. Phys.* **2010**, *82*, 1–6.

(72) Sun, Y.; Thompson, S. E.; Nishida, T. Physics of Strain Effects in Semiconductors and Metal-Oxide-Semiconductor Field-Effect Transistors. *J. Appl. Phys.* **2007**, *101*.

(73) Amer, A. W.; El-Sayed, M. A.; Allam, N. K. Tuning the Photoactivity of Zirconia Nanotubes-Based Photoanodes via Ultrathin Layers of ZrN: An Effective Approach toward Visible-Light Water Splitting. *J. Phys. Chem. C* **2016**, *120*, 7025–7032.

(74) Siuzdak, K.; Szkoda, M.; Sawczak, M.; Lisowska-Oleksiak, A.; Karczewski, J.; Ryl, J. Enhanced Photoelectrochemical and Photocatalytic Performance of Iodine-Doped Titania Nanotube Arrays. *RSC Adv.* **2015**, *5*, 50379–50391.

(75) Lee, E. J.; Pyun, S. Il. Analysis of Nonlinear Mott-Schottky Plots Obtained from Anodically Passivating Amorphous and Polycrystalline TiO2 Films. *J. Appl. Electrochem.* **1992**, *22*, 156–160.

(76) Nikolay, T.; Larina, L.; Shevaleevskiy, O.; Ahn, B. T. Electronic Structure Study of Lightly Nb-Doped TiO_2 Electrode for Dye-Sensitized Solar Cells. *Energy Environ. Sci.* **2011**, *4*, 1480.

(77) Li, H.; Chen, J.; Xia, Z.; Xing, J. Microwave-Assisted Preparation of Self-Doped TiO_2 Nanotube Arrays for Enhanced Photoelectrochemical Water Splitting. *J. Mater. Chem. A* **2015**, *3*, 699–705.

(78) Wang, T.; Luo, Z.; Li, C.; Gong, J. Controllable Fabrication of Nanostructured Materials for Photoelectrochemical Water Splitting via Atomic Layer Deposition. *Chem. Soc. Rev.* **2014**, *43*, 7469–7484.

(79) Hassan, N. K.; Hashim, M. R.; Allam, N. K. ZnO Nano-Tetrapod Photoanodes for Enhanced Solar-Driven Water Splitting. *Chem. Phys. Lett.* **2012**, *549*, 62–66.

(80) Hsu, C. H.; Chen, D. H. Photoresponse and Stability Improvement of ZnO Nanorod Array Thin Film as a Single Layer of Photoelectrode for Photoelectrochemical Water Splitting. *Int. J. Hydrogen Energy* **2011**, *36*, 15538–15547.

(81) Zhou, H.; Hsu, W.-C.; Duan, H.-S.; Bob, B.; Yang, W.; Song, T.-B.; Hsu, C.-J.; Yang, Y. CZTS Nanocrystals: A Promising Approach for next Generation Thin Film Photovoltaics. *Energy Environ. Sci.* **2013**, *6*, 2822.

(82) Miyauchi, M.; Hanayama, T.; Atarashi, D.; Sakai, E. Photoenergy Conversion in P-Type Cu_2ZnSnS_4 Nanorods and N-Type Metal Oxide Composites. *J. Phys. Chem. C* **2012**, *116*, 23945–23950.

(83) Nishi, H.; Kuwabata, S.; Torimoto, T. Composition-Dependent Photoelectrochemical Properties of Non-Stoichiometric Cu_2ZnSnS_4 Nanoparticles. *J. Phys. Chem. C* **2013**, 130920105942003.

(84) Zhang, Z.; Zhu, J.; Li, S.; Liu, X.; Mao, Y. Enhanced Photoelectrochemical Properties of TiO_2 Nanotube Arrays Sensitized with Energy-Band Tunable $(Cu2Sn)_{x/3}Zn_{1-x}S$ Nanoparticles. *Int. J. Hydrogen Energy* **2014**, *39*, 4198–4205.

Chapter 7

Conclusion & Future Work [*,†]

From the discussion presented in the preceding chapters, we can say that the objectives of the Thesis were achieved. In chapter 6, we have seen that complex Ti-Nb-Zr-O MPNTs were synthesized in a narrow window of anodization conditions using a formamide-based electrolyte containing NH_4F. The formation mechanism was discussed. MPNTs proved to possess a refractive index gradient, being maximum at the bottom oxide layer and decreasing as we get closer to the air at the top of the tubes, this increases light scattering probability. In addition, this refractive index can be precisely tuned by manipulating the NTs dimensions through synthesis conditions. As a proof, Air annealed MPNTs exhibited ~ 900% enhancement in the photocurrent compared to compact NTs, owing to the more positive flat-band potential, easier charge transfer, and higher carrier density. H_2 annealed samples showed the same trend confirming that this improvement is related to the presence of the MPNTs and independent of the annealing condition. Further verification was obtained by removing the multipodal portion of the NTs via sonication, the sonicated samples showed significantly lower photocurrent. Mott-Schottky analysis showed a positive shift in the flat band potential for the MPNTs compared to the compact one, along with almost double the donor density. To conclude, MPNTs have a tremendous potential as a route for enhancing metal oxides photoelectrochemical performance.

In chapter 7, we have seen that one step facile fabrication of complex multipodal Ti-Nb-Zr-O in a Formamide-based electrolyte was confirmed. SEM images confirmed the previously discussed growth mechanism, providing generic guidelines for the synthesis of MPNTs. Next, the effect of annealing in different atmospheres (Air, Oxygen, Hydrogen) on the structural and photoelectrochemical properties was studied. Raman, XRD and XPS suggest the presence of single mixed oxide Ti-Nb-Zr-O in a

---

[*] Parts of this chapter was published in: Omar, M. M.; Fawzy, S. M.; El-Shabasy, A. B.; Allam, N. K.; Large-Diameter Light-Scattering Complex Multipodal Nano-tubes with Graded Refractive Index: Insights into their Formation Mechanism and Photoelectrochemical Performance. *J. Mater. Chem. A*. **2017**, *5*, 23600 - 23611

[†] Parts of this chapter are submitted as a paper

strained anatase lattice under Air and Oxygen environments, where the Nb and Zr ions substitute Ti ions in the lattice in agreement with the infamous Hume-Rothery rules. However, annealing in a reducing atmosphere results in a more strained lattice, and a defective structure containing Ti^{3+}/Oxygen vacancies, beside the formation of a new phase, $ZrTiO_4$. XPS valence band spectra showed the presence of valence band tail states formed by hydrogen annealing leading to band gap reduction and extended NIR/Vis absorption. Mott-Schottky analysis showed four orders of magnitude increase in the donor density owing to the downshift of the CBM towards the Fermi level. The more negative flatband potential observed in H100 indicates enhanced charge separation. Also, Titanium substitution by Niobium under Hydrogen gas flow has resulted in excess charge carriers. All the previous considerations explain the tremendous photocurrent enhancement (~25 fold). To conclude, reduced complex MPNTs have shown enhanced photoelectrochemical performance due to the presence of defect states which enhance the absorption and increase charge carriers. We also see that CZTS sensitization has shown enhanced photocurrent but suffered from stability issues.

It is believed that the work presented in this thesis opens the door for many possible future work including:

1- Extending the multipodal nanotube morphology to other metal oxide semiconductors and other alloys such as TiO_2, $BiVO_4$, and others; as well as studying the effect of their annealing in different atmospheres.
2- Use simulations to get deeper insights regarding the graded refractive index phenomenon, and how it can be utilized to the maximum.
3- Attempt to stabilize CZTS by trying different aqueous electrolytes

Publications

- Omar, M. M.; Fawzy, S. M.; El-Shabasy, A. B.; Allam, N. K.; Large-Diameter Light-Scattering Complex Multipodal Nano-tubes with Graded Refractive Index: Insights into their Formation Mechanism and Photoelectrochemical Performance. *J. Mater. Chem. A.* **2017**, *5*, 23600 - 23611
- Fawzy, S. M.; Omar, M. M.; Allam, N. K Reduced Complex Multipodal Nanotubes: Band-tuning Through Defects. Submitted.